# Predicting Permeability and Capillary Pressure in Low-Resolution Micro-CT Images of Heterogeneous Laminated Sandstones

By

Pieter W.S.K. Botha

February 2017

A thesis submitted for the degree of Doctor of Philosophy of The Australian National University

Supervisory Panel:

Adrian Sheppard
Rob Heath
Mark Knackstedt

# Declaration of Contributions

The research documented in this thesis was done as part of a larger scale project funded by The Australian National Low Emission Coal Technology R&D group. Funding for the project was distributed between ANU and FEI for the purposes of data collection, analysis, and interpretation.

Specifically, staff members from FEI (now Thermo Fisher Scientific) collected the raw data in the form of micro-CT images of the core samples, and performed the initial image processing steps to prepare the images for further analysis.

The processed images were passes on to myself for detailed analysis, property and characteristics computation, statistical modeling and interpretation. I developed all the post-image processing analysis code to perform image unitisation and statistical calibration and predictions documented in the thesis. All the data documented in this thesis was compiled and interpreted by myself using various tools from previous work.

I generated all the reference data such as permeability and network model capillary pressure data using software created by staff from UNSW and FEI (Trondheim). I generated morphology capillary pressure data using the Mango software package written by staff at the Department of Applied Mathematics at ANU. These software programs have, over the past decade, become the gold standard for generating such data in the Applied Mathematics department.

Pieter Botha
08/02/2017

## Acknowledgements

To everyone I relied on for support and guidance during the course of this work. My supervisor Adrian, for always suggesting I could do more, and Jill, for always teaching me how I can do more. My friends, for comic relief when “it shouldn’t have worked before”. My family in far-away places, for your continuing support in everything I do. Renée, for always being interested in my latest graphical creation and supporting me without exception.

Additionally I’d like to acknowledge the Australian Government for funding me during my research with an Australian Postgraduate Award (APA) scholarship.

## List of Figures

µm/voxel image against Katz-Thompson permeability computed from the 16 µm/voxel image shows how several computation volumes in the 16 µm/voxel image have zero critical length, and therefore, zero computed permeability (c).  Plotted with the 'Matplotlib' python library with axis types set as 'symlog' (http://matplotlib.org/api/pyplot_api.html#matplotlib.pyplot.xscale), which provides logarithmic scales that include a small linear scale around zero, allowing zero to be plotted.

Figure 5.2: Comparing the grain size characteristic computed from the HR image of the 8mm sub-plug with the IR and LR images (a and b), and the pore size characteristic from the HR image with the IR and LR images (c and d) of the overlap regions from the 25mm core plug. The black diagonal lines show the 1:1 relationship on each diagram.

Figure 5.3: Comparing the grain sorting characteristic computed from the HR image of the 8mm sub-plug with the IR and LR images (a and b), and the pore sorting characteristic from the HR image with the IR and LR images (c and d) of the overlap regions from the 25mm core plug. The black diagonal lines show the 1:1 relationship on each diagram.

Figure 5.4: Comparing the porosity characteristic computed from the HR image of the 8mm sub-plug with the IR and LR images (a and b), and the clay fraction characteristic from the HR image with the IR and LR images (c and d) of the overlap regions from the 25mm core plug. The black diagonal lines show the 1:1 relationship on each diagram.

Figure 5.5: Comparing the open pore fraction characteristic computed from the HR image of the 8mm sub-plug with the IR and LR images (a and b) of the overlap regions from the 25mm core plug. The black diagonal lines show the 1:1 relationship on each diagram.

Figure 5.6: Comparing the surface area (a and b), mean curvature (c and d), and Euler number (e and f) Minkowski functionals computed from the HR image of the 8mm sub-plug with the IR and LR images of the overlap regions from the 25mm core plug. The changes in the characteristics are too large to plot a practical 1:1 line.

Figure 6.1: A porosity-permeability plot for the HR 5 µm/voxel image of the overlap region of sample 1. The graph shows a roughly linear relationship and the nearly continuous spread of the data points.

Figure 6.2: The correlations between permeability and open pore fraction (a and b), open pore size (c and d), and formation factor (e and f) calculated from the 16 and 64 µm/voxel images.

Figure 6.3: a) Open pore fraction as a function of the gray scale threshold value; b) The correlation $R^2$ between permeability and open pore fraction as a function of the gray scale threshold. The shaded areas show the range of gray scale values over which permeability remains highly correlated to open pore fraction, indicating that the statistical model is relatively independent of the image segmentation parameters.

Figure 6.4: Calibration of statistical models over the small field of view of the highest resolution image. The simulated permeability from the 5 µm/voxel image plotted against the predicted permeability from the multiple model containing open pore fraction, open pore size, and formation factor from the 16 µm/voxel image (a) and open pore fraction and formation factor from the 64 µm/voxel image (c). Multiple linear model residuals plotted against the predicted permeability values have no apparent systematic bias (b and d).

Figure 6.5: The predicted permeability of the 25 mm core plug computed from multiple linear model 2 (open pore fraction, open pore size, and formation factor) for the 16 µm/voxel image, and multiple linear model 1 (open pore fraction and formation factor) for the 64 µm/voxel image. Green horizontal stippled lines indicate the boundaries between rock units and the black box indicates the approximate location of the 8mm sub-plug. The scatterplots compare the predicted permeabilities from the 16 and 64 µm/voxel images for the 8 mm sub-plug calibration volume (left) and the 25 mm core plug (right).

Figure 7.1: a) The 25 mm core plug of sample 2 imaged at 16 µm/voxel; b) the 5 µm/voxel image of the 8 mm region of interest; and the overlap regions from the 16 µm/voxel and 61 µm/voxel images (c and d respectively). The white square indicates the approximate location of the 8 mm region of interest.

Figure 7.2: Calibration of statistical models for sample 2. The simulated

Figure 8.6: The R-squared and adjusted R-squared of multiple linear models of threshold pressure computed from the 5 μm/voxel image using sequentially fewer predictor characteristics calculated from the 16 μm/voxel image. Model 1 contains all eleven characteristics, while model 11 contains only one predictor (a). The vertical green and magenta stippled lines indicate respectively the models with the highest adjusted r-squared and with all significant characteristics (table 8.2). The computed threshold pressure plotted against the predicted pressure calculated with model 10 containing pore size and mean curvature as predictor characteristics (b). The residuals for model 10 plotted against the predicted threshold pressure values have no apparent systematic bias apart from an overabundance of data points towards lower pressure values (c).

Figure 8.7: The R-squared and adjusted R-squared of multiple linear models of threshold pressure computed from the 5 μm/voxel image using sequentially fewer predictor characteristics calculated from the 64 μm/voxel data. Model 1 contains all eleven characteristics, while model 11 contains only one predictor (a). The vertical green and magenta stippled lines indicate respectively the models with the highest adjusted R-squared and with all significant characteristics (table 8.2). The computed threshold pressure plotted against the predicted pressure calculated with model 9 containing open pore fraction, formation factor, and clay fraction as predictor characteristics (b). The residuals for model 9 plotted against the predicted threshold pressure values have no apparent systematic bias apart from an overabundance of data points towards lower pressure values (c).

Figure 8.8: Comparing the predicted threshold pressure from the 16 and 64 μm/voxel calibration data for the 8 mm sub-plug.

Figure 8.9: The computed lambda ($\lambda$) from the HR 5 μm/voxel image plotted against the predicted $\lambda$ using predictors from the 16 (a) and 64 (b) μm/voxel data.

Figure 8.10: The residual non-wetting phase saturation ($S_{or}$) computed from the HR 5 μm/voxel image plotted against the predicted $S_{or}$ using predictors from the 16 (a) and 64 (b) μm/voxel data.

Figure 9.1: The R-squared and adjusted R-squared of multiple linear models of threshold pressure computed from the 5 μm/voxel image using sequentially fewer predictor characteristics calculated from the 16 μm/voxel data. Model 1 contains all

eleven characteristics, while model 11 contains only one predictor.

Figure 9.2: The computed threshold pressure plotted against the predicted threshold pressure calculated with model 9 containing porosity, pore sorting, and grain sorting as predictor characteristics from the IR 16 μm/voxel data.

Figure 9.3: Demonstrating the subtle effect of opening the pore throats and removing and decreasing the size of some isolated clusters of voxels by increasing the number of intermediate gray scale values to convert to the pore phase. The original image in which the first 26 gray scale values were converted to pore volume (a), and the new image with the first 40 intermediate gray scale values converted to pore phase (b).

Figure 9.4: The computed threshold pressure from the modified HR 5 μm/voxel image plotted against the predicted threshold pressure calculated using model 10 with grain size and formation factor as predictor characteristics.

Figure 10.1: A visual comparison of x-direction network model and pore morphology-based capillary pressure simulation results of one sub-volume from units 1 (a), 2 (b), and 3 (c) in the HR 5 μm/voxel image of sample 1; diagrams comparing the threshold pressures (d) and lambda ($\lambda$) (e) parameters computed from Brooks-Corey modelling (section 8.2) of the network model and morphology-based drainage curves; and, a diagram comparing the estimated residual non-wetting phase saturation at the end of network model and morphology-based imbibition flow simulations (f).

Figure 10.2: Threshold pressure computed from network model drainage curves simulated using the HR 5 μm/voxel image plotted against the predicted threshold pressure of multiple linear models using characteristics from the IR 16 μm/voxel data (a) and the LR 64 μm/voxel image (b). The 16 μm/voxel model contains pore size and formation factor, while the 64 μm/voxel model contains formation factor and clay fraction.

Figure 10.3: Lambda computed from network modelling drainage curves using the HR 5 μm/voxel image plotted against the predicted lambda of multiple linear models using characteristics from the IR 16 μm/voxel data (a) and the LR 64 μm/voxel image (b). The 16 μm/voxel model contains surface area and mean curvature, while the 64 μm/voxel model contains formation factor and clay fraction.

Figure 10.4: Residual non-wetting phase saturation computed from network modelling imbibition curves using the HR 5 µm/voxel image plotted against the predicted residual non-wetting phase saturation of multiple linear models using characteristics from the IR 16 µm/voxel data (a) and the LR 64 µm/voxel image (b). The 16 µm/voxel model contains open pore fraction and the Euler characteristic, while the 64 µm/voxel model contains Euler characteristic and mean curvature.

Figure 10.5: The residual non-wetting phase ($S_{or}$) plotted as a function of irreducible wetting phase saturation ($S_{wi}$) at the end of drainage flow and receding contact angle ($\theta$). The colours indicated in the legend are applicable to all marker shapes.

Figure 10.6: The coefficient of determination ($R^2$) of multiple linear models between $S_{or}$ values, produced as a function of changes to $S_{wi}$ and $\theta$, and the 16 and 64 µm/voxel characteristics. Owing to the relatively small dataset the $R^2$ values plotted here are for those models containing just two predictors. The colours in the legend reference all marker shapes.

# List of Tables

## Publications from this Thesis

Botha, P. W. S. K., Golab, A., Bhattad, Goodwin, C., & Sheppard, A. P. (2014). Multi-Scale Imaging and Cross-Property Correlations in Heterogenous Sandstone. *International Symposium of the Society of Core Analysts*.

Botha, P. W. S. K., & Sheppard, A. P. (2016). Mapping permeability in low-resolution micro-CT images: A multiscale statistical approach. *Water Resources Research*. https://doi.org/10.1002/2015WR018454

## Table of Contents

# Abstract

Subsurface oil and gas reservoirs and fresh water aquifer systems are defined by fundamental geological characteristics such as mineral assemblage, grain and pore texture (size and shape), and porosity, and a range of petrophysical properties such as permeability, tortuosity, and capillary pressure, all of which contribute to fluid flow behaviour during extraction, injection, and storage.

Computer-based models of reservoir and aquifer systems use these fundamental rock characteristics and petrophysical properties for large-scale fluid flow simulations. Designing and testing accurate static models is essential for reliable flow predictions. A wide range of analytical techniques has been developed over many years to expand the range and quality of formation modelling data. The most commonly used techniques include down-hole logging systems and laboratory-based core analysis. Down-hole logging tools measure the geophysical properties of formations, for example: gamma radiation and electrical resistivity, and typically collect data at the scale of tens of centimetres to metres, though image logs from micro-resistivity tools can collect millimetre to centimetre scale data. Commonly used laboratory-based analytical techniques involve the use of drill core, core plugs, and drill cuttings, for routine and special core/cuttings analysis to determine reservoir and seal rock properties.

Modern X-ray micro-Computed Tomography (μCT) core imaging, in combination with petrophysical simulation software, often referred to as Digital Rock Physics, is fast becoming a standard tool for augmenting formation characterisation and modelling. Due to the nature of high-resolution μCT imaging and the associated analytical equipment, sample size is limited and governs the attainable resolution. It follows that metre-scale whole core samples cannot be imaged at the same high resolution as centimetre- and millimetre-scale core plugs. High-resolution images are critical to achieve reliable results from simulations of transport properties such as permeability and threshold injection pressure, which relies on all significant pathways in the pore space being correctly represented in the image. With current technology a μCT image of a 25mm diameter x 100mm tall sample, imaged using a detector with 2000 pixels per row, will have a minimum voxel size of ~13 μm, which implies that rock bands with grain and pore textures smaller than ~50 μm (i.e. 4 voxels across) cannot be represented with enough detail to reliably simulate petrophysical properties.

The main research objective is to investigate the relationships between geological characteristics and petrophysical properties of heterogeneous laminated sandstone

with the aim of estimating fluid flow properties for low-resolution images of larger rock volumes where fluid flow cannot be computed directly because of insufficient image resolution.

This thesis presents an imaging and computation workflow for predicting absolute permeability, threshold pressure, lambda (a parameter in the Brooks-Corey equation describing the shape of drainage capillary pressure curves), and residual non-wetting phase saturation for sample volumes that are too large to allow direct computation of these properties or where traditional correlation methods fail. The workflow involves computing the above-mentioned petrophysical properties from high-resolution µCT images, along with a series of rock characteristics from spatially registered low-resolution images. Multiple linear regression models correlating the petrophysical properties to rock characteristics provide a means of predicting and mapping those property variations in larger scale low-resolution images.

Two core samples of 25 mm diameter 80 mm tall of heterogeneous sandstone, for which 5 µm/voxel resolution is required to compute permeability and capillary pressure directly, were investigated in this study. Results show good agreement between statistical predictions of petrophysical properties made from intermediate-resolution images at 16 µm/voxel and low-resolution images at 64 and 61 µm/voxel for samples 1 and 2 respectively. The statistical models to predict permeability from low-resolution images at 64 and 61 µm/voxel (similar to typical whole core image resolutions) include open pore fraction and formation factor as predictor characteristics. Although binarized images at this resolution do not completely capture the pore system, I infer that these characteristics implicitly contain information about the critical fluid flow pathways, which control permeability.

Capillary pressure simulations were performed using both pore-morphology and network model-based methods. A prediction model of threshold pressure containing open pore fraction, formation factor, and, in this case, clay fraction is similar to the model of permeability from the low-resolution image of sample 1. My conclusion, which is similar to that of the permeability model results, is that formation factor and clay fraction, because their computation takes into account the image gray scale values, inherently capture information about the pore system length scale that controls threshold pressure.

A surprising yet important result is that of sample 2, where the set of predictor characteristics are unable to accurately predict threshold pressure. I conclude that this is because of image processing difficulties arising from a low signal to noise ratio in the high-resolution image, which complicates the segmentation of pore space from grain volume. The result suggests that image quality is critically important, which potentially eliminates the use of data collected using imaging techniques like ‘region of interest’ scans.

Statistical models of lambda using characteristics from pore morphology-based simulations describe 62% of the parameter variance. The predictor characteristics included in the model using low-resolution characteristics are open pore fraction, surface area, and mean curvature. Correlations between lambda computed from network model-simulations and low-resolution predictors are more encouraging with formation factor and clay fraction describing 93% of the variance in lambda.

Predicting residual non-wetting phase saturation poses a significant challenge and was not successfully addressed in this project. Neither the morphology-based nor the network model simulations produced data that correlate well with predictor characteristics. In the case of the network model-derived data it is possible that a larger dataset may improve residual non-wetting phase predictions.

# 1 Thesis Organisation

The research objective is the prediction of petrophysical properties in digital 3D imaging data where their direct determination is not realistically possible because of limitations in image resolution. To provide the relevant background information to the project the introduction (section 2) starts with an overview of petrophysical properties and related physical phenomena, which is followed by a description of the target sandstone formation and its relevance to hydrocarbon production, aquifer management, and $CO_2$ storage in a global context. Section 2 continues with an introduction to micro x-ray computed tomography imaging (µCT), the computation of the petrophysical properties from such 3D data sets, and the numerical upscaling of high-resolution geologic models for dynamic fluid flow simulation at formation scale. The introductory context of the project is followed by a detailed description of the research objectives.

Chapter 3 (Numerical Modelling and Multi-scale Imaging) compiles a review of past works related to efforts to develop numerical models to predict petrophysical properties (particularly absolute permeability) and the use of multi-scale µCT imaging to improve the general understanding of complex formations. Chapter 3 also contains a description of the unique contribution of the research results and interpretations documented in this thesis. Chapter 4 (Methods) provides details of sample selection and the methods used for data collection and analysis. Chapter 5, the first of the results chapters, demonstrates the impact of image resolution on the computation of absolute permeability and continues with a discussion on the changes to predictor characteristics with changing image resolutions. Chapters 6 and 7 compile and discuss the results of absolute permeability statistical models and predictions, while chapters 8 and 9 document the results of statistical modelling and prediction of capillary pressure, which was computed from pore morphology-based simulations. Chapter 10 briefly demonstrates some exploratory results of network model-based drainage and imbibition flow simulations and highlights the differences between network modelling and morphology-based multi-phase flow simulations. Conclusions and references are documented in chapters 11 and 12 respectively.

# 2 Introduction

## 2.1 Petrophysical Properties and Related Physical Phenomena

### 2.1.1 Absolute and Relative Permeability

Absolute permeability ($k$), with unit $m^2$ or more commonly Darcy (D) (where 1 D = $10^{-12}$ $m^2$), was first described by Henry Darcy in 1856 following extensive experimentation with the flow of water through sand beds arranged in vertical tubes (Darcy, 1856; Simmons, 2008). Permeability describes the ability of a saturated porous medium to allow the flow of a single fluid phase through its pore system. It is a fluid-independent parameter of the porous medium, and, combined with fluid viscosity forms the proportionality constant in Darcy's law (eq. 2.1) relating fluid flow through a porous medium to the change in fluid pressure over a certain distance. Darcy's empirical law is based on laminar flow and fails when the flow rate is high enough to induce turbulence. $Q$ is flow rate (e.g. vol/time), $k$ is the permeability constant ($m^2$), A is the cross-sectional area (e.g. $m^2$), $\Delta P$ in Pascals is the difference in pressure between the fluid inlet and outlet, $\mu$ is fluid viscosity (Pa.s), and $L$ is the length over which the pressure drop occurs.

$$Q = k\frac{A\Delta P}{\mu \mathrm{L}} \tag{2.1}$$

Under operational conditions a reservoir system is rarely saturated with a single fluid, partly because the system naturally contains multiple fluids in the form of water, oil, and gas, and partly because additional fluids such as water and $CO_2$ may be introduced into the system during enhanced production stages or injection for long-term storage. In a porous medium saturated with two or more immiscible fluids the effective permeability ($k_{ei}$) of the $i^{th}$ fluid can be determined by extending Darcy's law and assuming that one fluid remains static, essentially occupying some fraction of the pore space, while only the other fluid flows under pressure (Muskat & Meres, 1936) (eq. 2.2).

$$Q_i = k_{ei}\frac{A\Delta \mathrm{P}}{\mu_i \mathrm{L}} \tag{2.2}$$

Relative permeability is often considered co-current, i.e. both fluids flow in the same direction. The relative permeability of the $i^{th}$ fluid ($k_{ri}$) describes the flow of one fluid as the ratio of its effective permeability ($k_{ei}$) to the absolute permeability ($k$) of the porous medium (Ahmed, 2001) (eq. 2.3). It is normally expressed as a function of the saturation of one fluid phase, where saturation is the fraction of the pore volume occupied by that fluid.

$$k_{ri} = \frac{k_{ei}}{k} \tag{2.3}$$

### 2.1.2 Wettability

Unlike absolute permeability, relative permeability is not only a function of the medium, but depends on numerous other factors such as saturation, wettability, flow rate, viscosity and saturation history (Bennion & Thomas, 1991).

Wettability describes the wetting preference of a rock formation: whether a fluid prefers to adhere to, or to spread across a solid surface in the presence of another immiscible fluid (Craig, 1975). It is the result of forces such as adhesion, cohesion, and surface tension, and is quantified in terms of a contact angle, which is the angle between the contact surface between two immiscible fluids and a solid surface (figure 2.1). The wettability phenomenon is also a function of capillary forces (see section 2.1.3), which determine that, because of adhesion and cohesion forces, a fluid arranges itself in the smallest area per unit volume. A wetting fluid dropped onto a solid surface will spread across the solid surface, increasing the contact angle and displacing the non-wetting fluid until equilibrium is reached. A non-wetting fluid, on the other hand, forms droplets with a high value for the equilibrium contact angle. A water-oil/gas system is said to be "water-wet" when the contact angle is smaller than 75°, "neutrally wet" when it is 75°-105°, and "oil/gas-wet" when it is 105°-180° (Anderson, 1986).

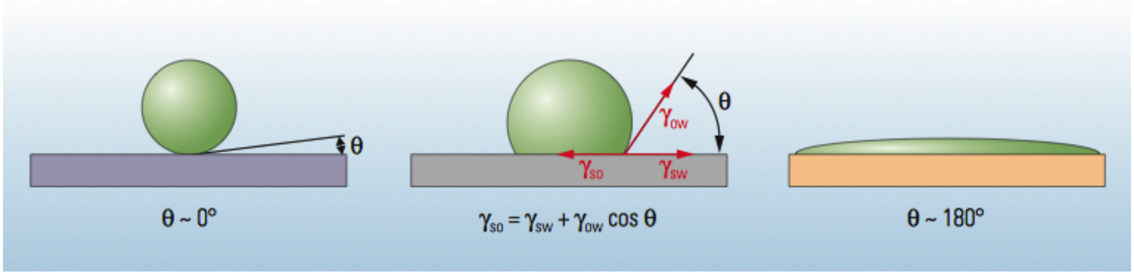

Figure 2.1: A non-wetting fluid forms droplets with a low contact angle on a solid surface, while a wetting fluid spreads across a solid surface with a high equilibrium contact angle (Abdallah et al., 2007).

Wettability affects relative permeability because capillary action fundamentally controls the distribution and flow of fluids in a porous substance. For example, figure 2.2 illustrates a strongly water-wet water-oil system at irreducible water saturation that undergoes imbibition (displacement of a non-wetting phase with a wetting phase). Water fills small pores, occupies pore crevices and covers rough grain surfaces, while oil fills the bulk of the pore volume. The relative permeability of the water phase, which exists as thin films at low to moderate saturations, can be very low. Under imbibition the non-wetting phase (oil) saturation and relative permeability decrease as a waterfront displaces the oil. Concurrently the wetting phase (water) saturation and relative permeability increase (figure 2.3). As imbibition continues, and water saturation increases, the connections between oil in adjacent pores are disconnected, leaving isolated oil droplets surrounded by water, resulting in decreased oil relative permeability. Even in this state the water relative permeability remains relatively low because the remaining oil droplets still occupy the larger pores and partially block the entrances to many of the pore throats [*Anderson*, 1987, part 5].

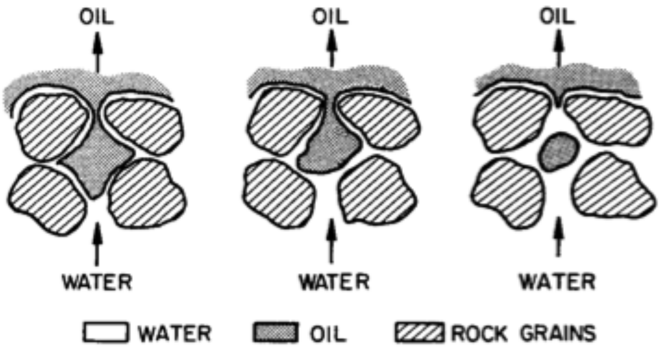

Figure 2.2: Waterflood displacement of oil from a pore [*Anderson*, 1987, part 5].

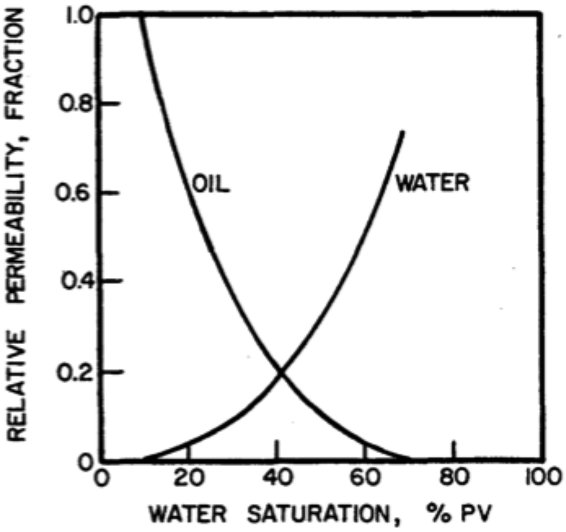

Figure 2.3: The changes in relative permeability of water and oil as a function of water saturation [*Anderson*, 1987, part 5].

The preferential displacement of fluids as a consequence of wettability is a critical factor in reservoir and aquifer management. Because of the effects of wettability laboratory measurements of relative permeability are susceptible to errors, especially when core samples are cleaned with solvents or contaminated with drilling fluid. This highlights the need for replicating reservoir temperature and pressure conditions and using the same fluids and well-preserved core samples with representative reservoir wettability for laboratory testing [*Caudle et al.*, 1951; *Anderson*, 1987, part 5; *Bennion and Thomas*, 1991].

### 2.1.3 Capillary Pressure

Two or more immiscible fluids in a saturated porous medium, in contact with one another, experience internal pressure as a result of forces like adhesion, cohesion, and surface tension, causing fluids to arrange themselves into the smallest area per unit volume to minimise free surface energy (Ahmed, 2001), and essentially controls the contact angle. The capillary pressure ($P_c$) is the pressure difference across the fluid interface and is proportional to the fluid-fluid interfacial tension and the mean curvature of the fluid-fluid interface, which is inversely proportional to the radius of curvature $r$ through the Young-Laplace equation, where $\lambda_{nw}$ is the surface tension between the non-wetting and wetting phases and $\theta$ is the contact angle (figure 2.4 and eq. 2.4). Note that the constant, 2 in equation 2.4, is only valid when considering circular capillaries. The interfacial curvature itself is controlled by the pore geometry (and particularly the pore radii), the fluid saturation and the contact angle (i.e. the wettability) [*Bear*, 1988, p 444-445].

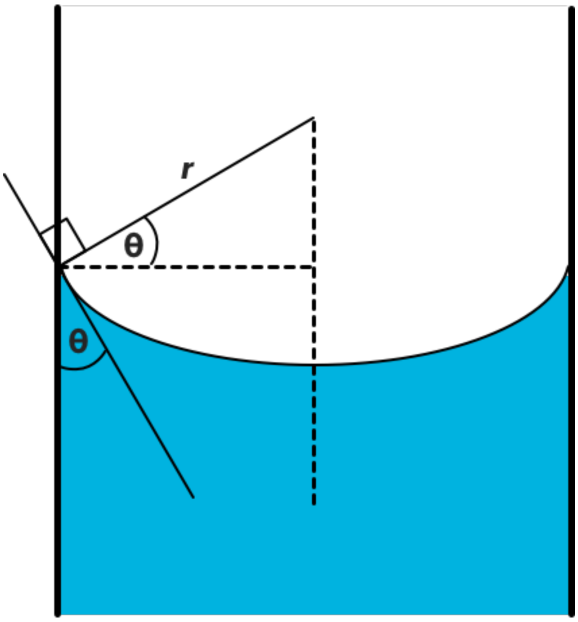

Figure 2.4: A schematic showing the curved fluid-fluid interface in a capillary as a result of a pressure difference between the two fluids. The pressure is higher in the non-wetting fluid than in that of the wetting fluid and the interfacial curvature is proportional to the pressure difference.

$$P_c = \frac{2\gamma_{nw} cos\theta}{r} \tag{2.4}$$

Capillary pressure either aids or hinders fluid flow defining the local pressure required to move a fluid through the pore network. At slow enough flow rates or for small enough samples, where the Darcy pressure difference across the sample is smaller than the capillary pressure, the flow is considered to be capillary-dominated.

Hysteresis describes a history dependence or non-uniqueness in a measured physical parameter as a function of an independently controllable input parameter. Figure 2.5 illustrates the capillary pressure curve for a water-saturated system under drainage by oil or gas and imbibition by water. Under drainage (displacement of a wetting phase by a non-wetting phase) the capillary pressure increases with decreasing water saturation until the system reaches its irreducible water saturation (the fraction of water that remains when a very high capillary pressure has been applied). Imbibition (displacement of a non-wetting phase by a wetting phase) increases the wetting phase saturation and decreases the capillary pressure along a pressure path that is lower than the capillary pressure for a given water saturation during drainage. Capillary hysteresis describes the difference in the capillary pressure curves under drainage and imbibition. The mechanisms for hysteresis are still a subject for debate. One mechanism suggests that the contact angle cannot be considered a single value for a given fluid pair, and that it is lower during drainage (advancing contact angle) than it is under imbibition (receding contact angle) [*Anderson*, 1987a, part 4; *Bear*, 1988, p 446-447 ].

In the context of $CO_2$ injection and storage it is thought that capillary trapping as a function of wettability and capillary forces should contribute significantly to subsurface trapping mechanisms (Al-Menhali & Krevor, 2016; Andrew et al., 2013; Krevor et al., 2015; Ren et al., 2014). Consider a water-wet $CO_2$-brine system with a water saturation of one. Under drainage (displacement of a wetting phase with a non-wetting phase) an injected $CO_2$ plume displaces the brine, reducing the water saturation and increasing $CO_2$ relative permeability. It is thought that $CO_2$ trapping will occur under water imbibition at the trailing edge of the injected plume, which will cause connected $CO_2$ clusters in adjacent pores to disconnect (snap-off) thereby trapping $CO_2$ at the pore scale by a combination of wetting and capillary forces.

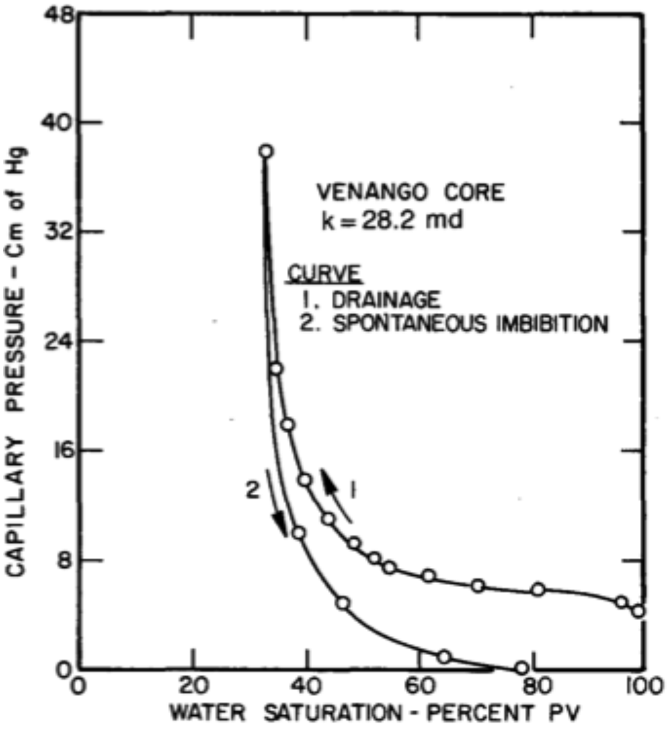

Figure 2.5: The capillary pressure curve for a water-wet water-oil system under drainage and imbibition [*Anderson*, 1987a, part 4].

### 2.1.4 Electrical Conductivity

*Archie* [1942] determined that the resistivity (resistance to the flow of electrical current) of a relatively clean water-saturated sandstone ($R_o$) is directly proportional to the water (usually brine) resistivity ($R_w$) and a formation resistivity factor ($F$). He demonstrated empirically that $F$ is directly proportional to the formation porosity ($\phi$) raised to the power of $-m$, described as the cementation exponent and determined as the line of best fit on a plot of the logarithm of formation factor against the logarithm of porosity (eq. 2.5 and 2.6).

$$R_o = FR_w \tag{2.5}$$

$$F = \phi^{-m} \tag{2.6}$$

Archie reports experimental results showing the cementation exponent typically varies from 1.3 for unconsolidated sediments to 2 for consolidated sediments. In more complex rocks with a variety of clay and other minerals, which also result in different wettability conditions because of more complex grain surface conditions, cementation exponent values of up to 5 have been reported (Focke & Munn, 1987).

Archie's law is only valid when there are no conductive minerals in the rock matrix and holds well for relatively clean sandstones; however, *Patnode and Wyllie* [1950] conclude that electric current could be carried, not only by the saturating fluid, but through conductive clay minerals in "shaly sands", and propose an expanded form of Archie's law to account for conductive phases in the rock matrix (eq. 2.7), where $C_o$ is the formation conductivity, and $C_s$ and $C_w$ represent the conductivity of solids and brine respectively.

$$C_o = C_s + \frac{C_w}{F} \tag{2.7}$$

*Winsauer and McCardell* [1953] suggest the excess conductivity in shaly reservoir rocks is due to an increased ionic concentration in the fluid layer adjacent to charged clay surfaces. This is still considered to be a significant factor controlling the conductivity of such rocks and presents yet another variation of Archie's law (eq. 2.8) where $C_z$ is the conductivity of charged clay surfaces.

$$C_o = \frac{1}{F}(C_s + C_z) \tag{2.8}$$

## 2.2 The Precipice Sandstone

The target formation for the primary study is the Precipice sandstone, the early Jurassic age basal formation of the Surat Basin, in southeast Queensland, Australia. The sedimentology of the Precipice sandstone was studied in detail by *Martin* [1977], and by previous investigators in early descriptions of the Surat Basin geology and stratigraphy (Jensen, 1921, 1926; Reeves, 1947; Whitehouse, 1953). Martin describes the Precipice sandstone as a fluviatile depositional facies, deposited by low-sinuosity braided stream systems, predominantly flowing from west to east. Source rocks include mainly granitic basement, evidenced by the presence of feldspar and biotite, with some contribution from metamorphic and sedimentary sequences, as interpreted from the occurrence of rock fragments, towards the western edge of the basin.

Along with *Allen and Houston* [1964] Martin report the Precipice to be a fine- to coarse-grained laminated sandstone, with laminations ranging in thickness from just a few millimetres to several centimetres. It contains low quantities of clay minerals (generally less than 10%) and minor amounts of accessory minerals including feldspar and mica. Diagenetic alterations include silica redistribution and the chemical alteration of feldspar and biotite to kaolinite. Silica redistribution can be caused by overburden pressure or may be chemically induced. *Martin* [1977] describes that quartz dissolution is closely related to the occurrence of biotite, which is almost always partially altered to kaolinite. This suggests a chemical mechanism for silica redistribution, rather than by overburden pressure dissolution, in which case silica dissolution would be more distributed more evenly instead of being correlated with biotite. Results also indicate that finer grained sediments contain higher proportions of mica, which, due to its flaky habit, is commonly deposited along with finer sediment sizes, providing a possible explanation for the extraordinarily low porosity and permeabilities in the fine-grained intervals of the Precipice, which cannot be explained by grain size alone.

Figure 2.6 shows a two-dimensional slice from a tomogram and demonstrates the range of grain and pore sizes present in a single core plug. It clearly shows fine-grained lamellae near the top and much coarser grained zones near the middle of the image.

The Precipice is an ideal target formation for injection and storage because of its relatively high permeability, but also its large degree of heterogeneity. Even though the data from this project will be applied to $CO_2$ storage, the results are more widely applicable to fields such as oil and gas exploration and production and aquifer management and remediation. In particular the methods developed in this study are aimed at improving the range of data available for large scale formation modelling and simulation.

A typical feature of fluvial sedimentary rocks is sedimentary stratification, or layering, which is the accumulation of distinct beds as a function of changes to the depositional conditions in which they formed. Changes to the depositional environment may include the volume of water or the energy available to transport sediment, or the volume or type of detritus in the source region. Layering is evident because of differences in characteristics such as particle size, shape, and distribution, and the mineral and fossil content in each layer (Boggs, 2003). Layered sandstone formations such as the Precipice are fairly common around the world and the influence of heterogeneity on fluid flow properties is a topic of significant importance. *Kjonsvik et al.* [1994] investigate shallow marine reservoirs with layers of rock characterised by different texture and petrophysical properties. They point out that in order to assess waterflood performance it is important to understand the degree of pressure communication across the boundaries separating layers with different permeabilities. They also mention that the spatial arrangement of layers with contrasting permeability and their pore scale attributes such as wettability can either result in improved oil recovery or oil trapping during water flooding. The Burgan oil field in Kuwait, the largest sandstone reservoir in the world, was deposited in a fluvial deltaic system (Kaufman et al., 2002), encompassing braided river channels for the South Burgan field and estuarine and tidal channels for the North Burgan field (Filak et al., 2013), which produce fine laminated structures similar to those in the Precipice Sandstone.

Fine laminations complicate the interpretation of petrophysical logs, especially when sand layers are interbedded with layers rich in clay content, because the laminations are often finer than the vertical measurement resolution of down-hole tools. Small-scale structures such as those in the Precipice cannot be taken into account with anything but the highest resolution tools such as those used to produce micro-resistivity logs, which may not report the information required. Fine laminations also result in less than ideal data from conventional laboratory measurements because the samples themselves may not be representative of the formation, and the sample may be heterogeneous and produce variable results as a function of measurement direction). µCT image-based fluid flow simulations are not immune to fine scale heterogeneities. Section 2.3 and 2.4 describes the relationship between sample size, image resolution, and the impact on the ability to simulate flow properties. With insufficient image resolution to accurately capture the pore system, flow properties cannot be computed numerically; therefore, heterogeneities often cannot be taken into account with a single sample. The research objective is to develop a method to estimate fluid flow properties in low-resolution µCT images of samples where they cannot be computed directly.

I approach this study with the conclusion that the Precipice Sandstone serves as a good approximation of typical sandstone reservoir and aquifer systems. It is relatively clean and free of clay minerals, but contains significant heterogeneity in the form of fine laminations defined by differences in grain and pore texture attributes.

The remaining sections of the introduction continue with an overview of µCT imaging, the impact of image resolution on fluid flow simulations, which is followed by a detailed description of the research objective (section 2.6) in the context of these introductory concepts.

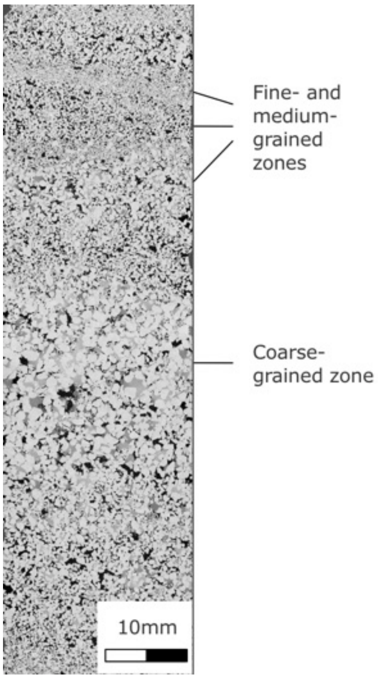

Figure 2.6. Demonstrating the range of grain and pore textures in a single 25 mm diameter x 80 mm tall core-plug sample.

## 2.3 Micro X-ray Computed Tomography Imaging (µCT)

µCT scanning systems produce tomograms, which are three-dimensional representations of the internal structure of a sample placed in between a point source of X-rays and an X-ray detector array (camera) (figure 2.7). *Van Geet et al.* [2001], *Cnudde and Boone* [2013], and *Wildenschild and Sheppard* [2013] provide detailed descriptions of the history and fundamentals of µCT equipment, imaging principles, and potential applications of the technique in various fields of study. Focussed X-rays are generated within an X-ray source by bombarding a tungsten target with an electron beam. The X-rays are directed to travel through the sample and are captured by a camera, which converts the x-ray signal to a 16 bit grey-scale image, also known as a projection. The grey level of each pixel in the projection is related to the degree to which the incident X-rays were absorbed (attenuated) by the minerals and fluids in the sample as a function of electron density and average atomic number. Following linearization of the projection data with respect to flat-field images, each pixel represents the integrated attenuation of each mineral lying on the X-ray line between the source point and the detector pixel. Incrementally rotating the sample, and collecting a new projection after each rotation, generates a series of projections. A reconstruction algorithm is used to produce the 3D tomographic image from the series of two-dimensional projections.

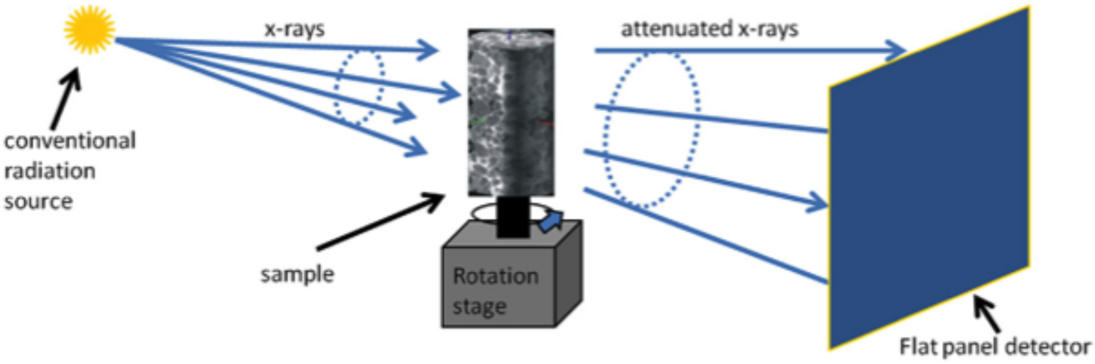

Figure 2.7: A typical µCT configuration with the sample located between an X-ray point source and an X-ray detector array (Wildenschild & Sheppard, 2013).

*Varslot et al.* [2010] demonstrates the use of a more advanced helical scanning system to achieve high-resolution imaging in a practical time frame. In addition to being rotated the sample is also moved vertically, where the pitch describes the vertical distance moved for each complete rotation of the sample. Varslot et al. also describes some of the challenges involved in producing high-quality µCT images, such as misalignment artefacts, image drift due to fluctuations in ambient temperature, and the close relationship between X-ray source spot size, image resolution, and imaging data signal to noise ratio.

In computed tomography imaging, field of view and image resolution are directly related through the number of voxels in each dimension in the reconstructed tomogram (Sakellariou et al., 2004). Lower resolution images, such as those of whole core samples, provide greater sample coverage and capture more sample heterogeneity, but do not adequately represent the pore structure and cannot be used for direct permeability computation. On the other hand, images with higher resolution permitting direct computation of fluid flow properties, have correspondingly smaller fields of view. These small images, though high in resolution, only cover a representative volume for the most homogenous rocks and are very different in scale from core plugs used in conventional experiments. High-resolution µCT imaging can generally be achieved for sample sizes ranging from 5 to 25 mm in diameter; however, sample size limits are very much a function of the imaging system in question. For samples greater than 25 mm diameter one would start considering the use of whole core or medical CT scanners, keeping in mind that medical CT images of whole core often provide little information about petrophysical properties.  Classifying an image as high- or low-resolution depends on how the image resolution compares to the scales of sample textures. Two core plug samples of 10 mm diameter, one with fine and one with coarse textures, could be imaged at the same absolute resolution (say 8 µm/voxel side length), and the image of the fine texture sample considered to be low-resolution and that of the course texture sample to be high-resolution, based on the extent to which the rock texture is captured within each image.

## 2.4 Image Resolution and Petrophysical Properties

The equations to compute electrical conductivity and permeability are those of Laplace and Navier-Stokes respectively. Laplace’s equation (eq. 2.9) (Øren et al., 2007), also known as the continuity equation for potential flow, presents solutions in the form of potential functions that describe the idealised behaviour of potential fields.

$$\nabla \cdot \sigma_w \Delta p = 0 \qquad (2.9)$$

$\sigma_w$ is the electrical conductivity of the fluid in the rock and $p$ is the electrical potential. In the case of electric fields the Laplace equations describes the electrostatic potential in an area that has no charge.

The Navier-Stokes equations are a set of formulations that describe fluid flow. It comprises the momentum equation, which arises by combining Newton's second law of motion with a fluid component, and the continuity equation defining the conservation of mass. Permeability simulations in this study are based on the Lattice-Boltzmann method, which approximates the solutions of the Navier-Stokes flow equations. The fluid is represented as generalized particles (Christoph H. Arns et al., 2004) and placed under a pressure gradient by a body force throughout the volume (Ferréol & Rothman, 1995), or by constant-pressure boundary conditions, i.e. no-flow at the boundary. Additionally, the Lattice-Boltzmann method uses the Bhatnagar-Gross-Krook (BGK) relaxation term as an approximation of particle collision behaviour (Bhatnagar et al., 1954).

Imaging techniques such as µCT described in section 2.4 make it possible to generate realistic digital 3D representations of rocks and their pore systems, which are ideal for the numerical computation of petrophysical properties. *Spanne et al.* [1994] and *(Martys et al., 1999)* investigate Fontainebleau sandstone and were among the first to identify the need for high-quality images with sufficient resolution. They emphasise the need for 3D images that accurately capture those pore geometries that control fluid flow to produce reliable computational results of petrophysical properties. Generally permeability simulations only return useful results if the image resolution is sufficiently high to represent flow pathways in the pore system with at least four open voxels, i.e., the voxel size needs to be 4 times smaller than the diameter of the smallest pore throats that lie on percolating flow paths. The no-slip conditions mean a Poiseuille velocity profile, which needs at least four voxels to be represented with any accuracy.

Figure 2.8 is a qualitative diagram showing the theoretical effect of image resolution on phase proportions and the ability to compute numerically petrophysical properties, in this example, absolute permeability. Consider a two-component system comprising one solid phase (grains) and one air phase (pores). With modern 3D scanning systems achieving micrometre- and tens or hundreds of nanometre-scale imaging resolution (Cnudde & Boone, 2013; Metz et al., 2009; Varslot et al., 2010) the two components are well differentiated and a histogram of gray scale intensities shows only two peaks, one gray scale value for each component. As image resolution decreases (e.g. for imaging larger fields of view), an increasing fraction of the voxels lie on the surfaces between grain and pores and thus appear as intermediate gray scale values, because the volume sampled by those voxels includes both grain and pore (the 'partial volume effect'). With a further decrease in image resolution the proportion of intermediate gray scale voxels increases and the proportions of voxels representing the original two components decrease. At some pore size dependent resolution the interconnections within the pore space (i.e. pore throats) start to be represented entirely by intermediate gray scale values and direct transport modelling becomes impossible. Extracting information from images in this regime, where transport pathways cease to be fully resolved, is the focus of this work.

At even lower resolution, the spatial averaging associated with each voxel covers such a large volume that all geometric information is lost. It is normally considered that medical CT scanning, with a typical resolution of around 500 μm/voxel, falls into this last category. With a complete absence of geometric information, CT scans of whole core are not used to estimate permeability, and it seems unlikely that worthwhile information for predicting transport properties could be extracted.

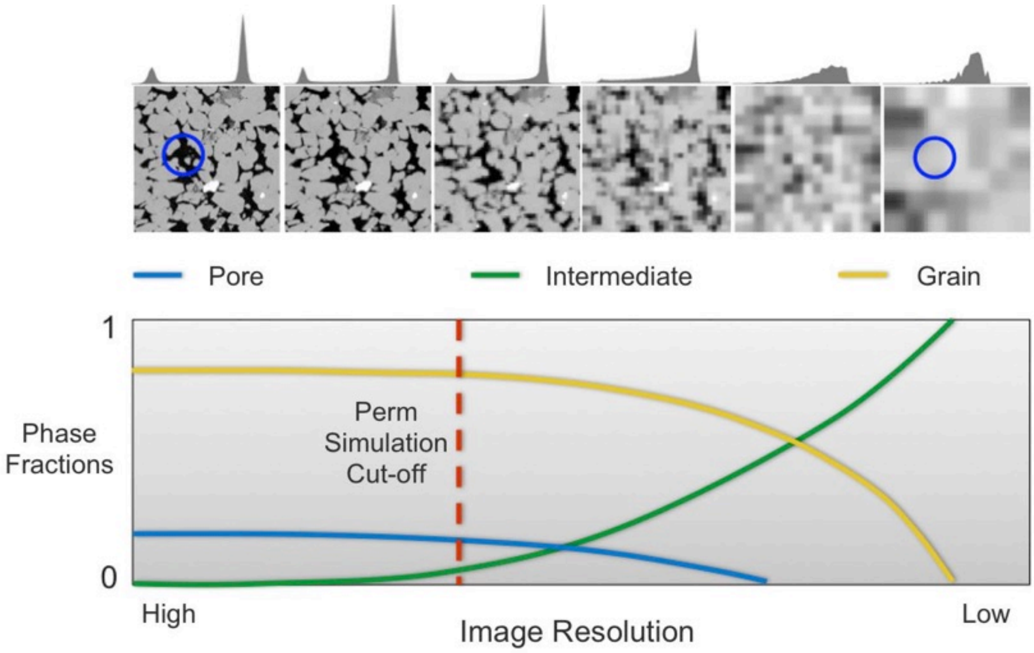

Figure 2.8: The effect of image resolution on phase identification. High-resolution images resolve pore space geometry with high fidelity while at low-resolution pores are represented partially or completely by intermediate gray scale values.

*Berg* [2012] and *Zhang and Knackstedt* [1995] evaluate electrical conductivity and highlight the importance of pore geometry and flow path tortuosity. *Arns et al.* [2001] investigate the effects of image resolution and associated segmentation errors, such as poor representation of pore geometry, on the numerical computation of electrical conductivity. For a single sample represented by a range of image resolutions, they observed systematic overestimation of formation factor with decreasing image resolution.

In lower-resolution images, the pore throats are depicted by intermediate gray scale voxels (rather than open pore voxels) and consequently do not allow flow during simulation: the simulated permeability will therefore be zero regardless of the actual permeability. *Apourvari and Arns* [2014] assess the effect of sub-resolution porosity on permeability and use a Lattice Boltzmann method modified with the Brinkman approach (Brinkman, 1949) that includes regions of sub-resolution porosity in the permeability computation by applying Darcy's law to such regions. This approach suffers the shortcoming that one must estimate the permeability of the sub-resolution porosity, often without knowledge of the pore space geometry. Since permeability is highly dependent on channel diameter this approach may have very large uncertainties.

In studying the effect of image resolution on permeability simulation, *Peng et al.* [2014] found that two µCT images of Berea Sandstone with resolutions of 1.85 and 5.92 µm/voxel return nearly identical permeability, indicating that the latter is high enough resolution to capture the main flow paths for that rock, and that the smaller pores need not always be resolved. *Zhang et al.* [2000] investigate the scale dependency of the so-called representative element volume (REV), a range of physical sample volumes for which a measured quantity such as permeability does not change. Their results show that the REV for a Brent Triassic sandstone sample is considerably larger than that of a sample of crushed glass beads, because of the increased degree of heterogeneity of the sandstone. In the context of image resolution and field of view, and depending on the sample heterogeneity, it is clear that for any given sample, volumes that fall in the range of an REV may not always have sufficient resolution to allow permeability simulation.

## 2.5 Numerical Upscaling

Subsurface oil and gas reservoirs and fresh water aquifer systems are heterogeneous systems characterised by geological measures such as mineral assemblage, grain and pore texture (size and shape), and porosity. These measures, or fundamental characteristics, combine together to produce a range of petrophysical properties such as absolute and relative permeability, tortuosity, and capillary pressure, which contribute to fluid flow behaviour during extraction, injection, and storage (Ahmed, 2005).

Computer-based static models, or descriptions, of reservoir and aquifer systems are based on these fundamental geologic characteristics and petrophysical properties and form the basis for dynamic fluid flow simulations. Designing and testing accurate static models are essential for reliable flow predictions (M.J. King & Mansfield, 1999) and a wide range of analytical techniques has been developed over many years to expand the range and quality of reservoir modelling data. Notably, these techniques collect data at various scales and need to be incorporated in a single geological model. The most commonly used techniques include down-hole logging systems and laboratory-based core analysis. Down-hole logging tools measure the geophysical properties of formations, for example: gamma radiation (useful for identifying geological formation tops and serves as a measure of clay mineral content) and electrical resistivity (indicates formation fluid type) (Darling, 2005). Down-hole logs typically collect data at the metre scale, though image logs from micro-resistivity tools can collect millimetre-scale data. Laboratory-based analytical techniques most often involve the use of drill core, core plugs, and, in recent years, drill cuttings, for routine and special core/cuttings analysis, and 3D X-ray Computed Tomography imaging to determine reservoir and seal rock properties (Bell, 1996; Ubani et al., 2012). In addition to these laboratory and down-hole techniques, outcrop and field performance data are often included in static models (Michael J. King, 2007), which are typically constructed with small grid cells because it is generally accepted that fine scale features can significantly impact reservoir and aquifer flow behaviour (Jones et al., 1995).

Several papers reviewing upscaling techniques and procedures have been written in recent time (Durlofsky, 2005; Farmer, 2002; Renard & de Marsily, 1997). Numerical upscaling, sometimes referred to as upgridding, describes the process of constructing lower-resolution models (models with fewer grid cells for the same volume) from high-resolution static geologic models of the formation in question. A high-resolution geologic model typically describes a formation with a large number of grid cells (~$10^7$ – $10^8$ cells), where each grid cell, still potentially at the metre scale, is small enough to capture variations in the distribution of formation properties. In his review *Durlofsky* [2005] emphasises the need for uncertainty analysis in reservoir performance, which means understanding the range of flow behaviour to be expected from a given formation. For this reason it is often necessary to perform many iterations of flow simulations, each one under slightly different conditions; therefore, the demands on computational resources are considerable and high-resolution models cannot be used to produce large-scale flow simulation data in an efficient and cost-effective manner. The upscaling process populates the grid cells of a lower resolution model (~$10^5$ – $10^6$ cells) with effective, or representative, values of those properties relevant to dynamic flow modelling. Each grid-cell of the lower-resolution model, which could be several meters in length per side, is represented by several grid-cells in the higher-resolution equivalent, which contains more detail on small-scale variations in the flow properties of the formation. Figure 2.9 demonstrates how a region with many grid cells in a static description is upscaled by computing a single representative value and assigning it to a single grid cell in a lower resolution model.

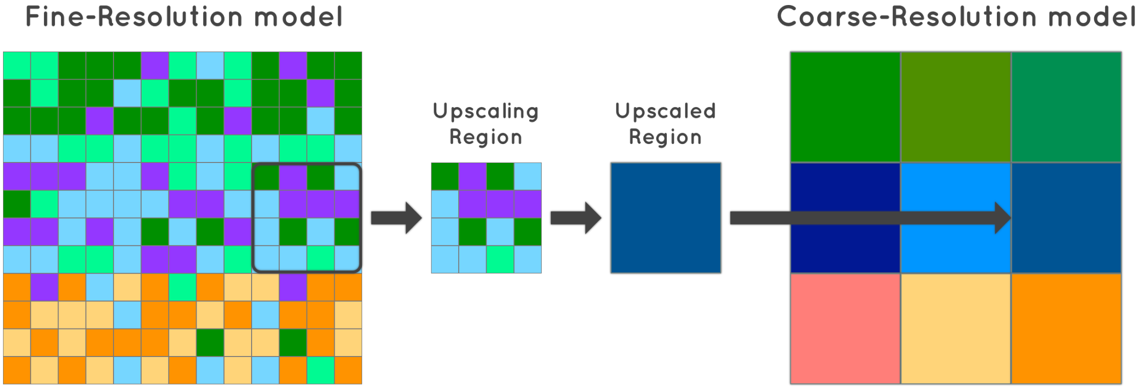

Figure 2.9: A conceptual example of how the grid cells of a low-resolution model are populated with effective values based on the input information from a many grid cells in a high-resolution model.

## 2.6 Research Objective

The combination of μCT image resolution and the heterogeneity of laminated sandstone, with highly variable grain and pore textures from one lamella to the next, result in flow simulation data from small-scale samples that are not representative of the larger scale. This thesis focuses on developing a method to predict and map petrophysical property variations over the large fields of view obtainable from lower resolution tomographic images, such as images of core plug and whole core samples. After initial exploration of the data yielded insufficient evidence to suggest a clear path for rock classification I concluded that a statistical approach would be more appropriate. The research is based on a multi-scale imaging workflow and subsequent statistical correlations between rock characteristics computed from large-scale low-resolution images and petrophysical properties numerically computed from small-scale high-resolution data. The focus of this research is not numerical upscaling as described in section 2.5 above, but rather the construction of three-dimensional flow property maps in relatively low-resolution core images, which can ultimately serve as input for numerical upscaling at the whole core scale and beyond. When it comes to estimating petrophysical properties in larger scale low-resolution data, many authors refer to this process as 'upscaling' of pore-scale data. This can be a confusing use of terminology; therefore, I refer to the process as 'property mapping' in low-resolution images, rather than 'upscaling' to avoid confusion with its conventional meaning described in section 2.6.

The petrophysical properties of interest are absolute permeability, and a small set of parameters defining capillary pressure curves, including, threshold pressure and residual non-wetting phase saturation, or trapping number in the context of $CO_2$ injection and storage.

The range of rock characteristics I investigate in this thesis as potential predictor variables in statistical correlations with the aforementioned petrophysical properties are open pore fraction, porosity, which includes the sub-resolution pore fraction), clay fraction, formation factor, grain and pore size and sorting, and the Minkowski functionals (pore fraction, surface area, mean curvature and the Euler characteristic). Chapter 3 (Methods) provides more detail on how the petrophysical properties and rock characteristics were computed from the high- and low-resolution images respectively.

The accurate representation of pore throats is critical for reliable fluid flow simulation since they are the primary controllers of both permeability and capillary entry threshold pressure. I approach the objective of this work with the following two hypotheses:

1) The classic approach to such problems applies classification methods to group repeating rock units; however, I suggest that a statistical approach may be more appropriate, and
2) Where pore throats are represented as intermediate gray scale voxels in lower resolution images, those measures that somehow make use of the image gray scale values have the potential to correlate with fluid flow properties

In section 3.2 I mention that a classification-based workflow seems like a reasonable approach for heterogeneous laminated systems like the Precipice sandstone, however, evidence presented in chapter 4 suggest that a statistics-based method to flow unit characterisation may be more appropriate.

Considering which rock characteristics will provide the most value to a statistical method I hypothesise that where pore throats are represented as intermediate gray scale voxels in lower resolution images, those measures that somehow make use of the image gray scale values have the potential to correlate well with fluid flow properties. For this reason the formation factor characteristic is of particular interest. Even though it is a petrophysical property defined through electrical conductivity, the formation factor computation used in this study can be tuned to take into account gray scale values of low-resolution images, which makes it a potentially useful predictor of fluid flow properties. Chapter 4 (Results and Discussion) highlights the usefulness of formation factor as a predictor and contains extensive information related to how the range of predictors behave when they are combined in multiple linear statistical models to predict petrophysical properties.

The funding for this project was provided by Australian National Low Emissions Coal Research and Development (ANLEC R&D), a federally funded agency that guides research and development aimed at low emissions coal technology. This project forms part of a larger umbrella project aimed at better understanding the technical challenges and feasibility of $CO_2$ injection and storage in the Precipice Sandstone near Wandoan, Queensland, Australia.

# 3 Numerical Models and Multi-scale µCT Imaging

## 3.1 Numerical Models of Petrophysical Properties

The relationships between petrophysical properties and fundamental rock characteristics have long been a topic of interest and stems from the need for petrophysical data in reservoir and aquifer modelling. However, petrophysical data is often difficult and costly to obtain; therefore, a large number of researchers have investigated and proposed various methods of predicting petrophysical properties, in particular absolute permeability, from more readily measurable rock characteristics. Nelson (1994) provides a thorough review of permeability, its controlling factors such as porosity, grain size and sorting, clay mineral content, and relationships with other petrophysical properties like electrical conductivity and capillary pressure. All equations presented in this chapter provides permeability with darcy units.

Some of the early attempts to predict petrophysical properties focussed on the rock fabric and grain characteristics. In clastic sedimentary rocks the grain texture (grain size and sorting) has indirect control on permeability. At a basic level porosity is grain size independent for rocks with equal sorting and grain packing. *(Krumbein & Monk, 1943)* conducted permeability experiments in sand packs at 40% porosity with known grain size and sorting values. Their work resulted in equation 3.1 correlating permeability with the geometric mean grain diameter ($D_g$) and an exponential dependence on grain sorting ($\sigma$) (see section 4.6.1). Interestingly their equation does not include a porosity component, however, amongst other sedimentary processes grain sorting controls porosity in unconsolidated sands, therefore it could be argued that porosity is indirectly included in the grain sorting component.

$$k = 760\ D_g^2 \mathrm{e}^{-1.31\sigma} \tag{3.1}$$

*Berg* [1970] developed a similar empirical model for unconsolidated sands and relatively clean consolidated sandstones also based on geometric mean grain size and grain sorting as the difference between the 90th and 10th percentiles of the grain size distribution; however, it also includes porosity ($\phi$). Berg's assumption is that permeability is primarily controlled by the smaller grain sizes, which serve to block pores and pore throats (eq. 3.2).

$$k = 5.1 * 10^{-6} \phi^{5.1}\ D_g^2 \mathrm{e}^{-1.385\sigma} \tag{3.2}$$

Grain size and sorting serve as interesting and valuable parameters to predict permeability, however, more directly it is the pore size and the size of pore connections that control permeability (Nelson, 1994).

One of the most well known empirical equations to predict permeability is that of Kozeny and Carman. The Kozeny-Carman equation (Carman, 1956; Kozeny, 1927; Paterson, 1983; Walsh & Brace, 1984) simplifies fluid flow through complex pore systems by expressing it in terms of laminar flow through a bundle of tubes of varying radii. The equation relates permeability to the hydraulic radius of the tubes, determined as the reciprocal of the ratio of pore surface area to rock volume, or, specific surface area ($\sum_p$ ), porosity ($\phi$), and tortuosity ($\tau$), the ratio between a path length longer than the sample ($L_\alpha$) and the sample length ($L$) (eq. 3.3).

$$k = \frac{\phi}{\int \tau \sum_p^2} \tag{3.3}$$

Ever since the initial days of digital image processing researchers have investigated the relationships between pore space geometries and flow properties such as absolute and relative permeability in an attempt to find measures by which they can predict fluid flow in porous samples. In his paper *Doyen* [1988] compiles a brief list of early works in this field. *Rink and Schopper* [1978] studied two-dimensional images of sandstone, which represent the pore system as isolated clusters of pore bodies connected with narrow tubes, which we might call the pore throats. They make use of image processing techniques including erosion and dilation to remove the pore throats from the image and represent the pore system as isolated pore bodies with roughly convex shapes. A pore size distribution histogram constructed by measuring the diameters of the pore bodies can then be used to calculate the sample permeability. *Berryman and Blair* [1986] collected high-resolution scanning electron microscope images of three samples: a reference sample of glass beads, Ironton-Galesville sandstone, and Berea sandstone. They estimated the porosity and pore specific surface area from measured two-point spatial correlation functions, which they combine with known values of electrical formation factors to predict permeability using a form of the Kozeny-Carman equation. The authors report that for the glass beads their estimated permeability data range within 10-20% of the measured values. For the Ironton-Galesville and Berea sandstone the predictions are within 20%, and 10-30% respectively. The authors also specify that image resolution and detail are critical, especially for the specific surface area, which required magnifications of ~500x. Porosity measurements are less sensitive and could be collected at lower resolution settings of ~100x. *Doyen* [1988] continues the discussion around digital image resolution and mentions that the specific surface area is directly proportional to the slope of the two-point correlation function evaluated at the origin. Critically, digital images are represented by pixels of predetermined size, and the slope of the correlation function at the origin increases with decreasing pixel size, or increasing microscope magnification. It follows that the permeability predictions made using the Kozeny-Carman equation is strongly dependant on the imaging magnification used for computing the specific surface area. *Doyen* [1988] investigates seven epoxy-impregnated thin-sections of Fontainebleau sandstone, compiling pore and throat size distribution data using an image-analyser and image erosion techniques similar to that of *Rink and Schopper* [1978]. He computes characteristic throat sizes for the flow of fluids and electrical current, which was used to predict permeability and electrical conductivity with Bruggeman's effective medium approximation.  His predicted permeability and conductivity to within a factor of three of the laboratory measured values. The data indicate that in the Fontainebleau sandstone there is a large decrease in permeability and conductivity associated with decreases in porosity. Highlighting that sample porosity is controlled by pore bodies that maintain relatively large dimensions, even at low porosities, and that flow coefficients are related to pore throats, he suggests that during diagenesis the pore throats shrink until they are completely closed at porosities below 10%, thereby explaining the reduction in flow coefficients with decreasing porosity. He also mentions that such pore-scale heterogeneity cannot be explained by the Kozeny-Carman method, which relies on a homogenous pore system.

*Paterson* [1983] and *Walsh and Brace* [1984] modified the Kozeny-Carman approach after highlighting the relationship between tortuosity and formation factor ($F = \left(\frac{L_\alpha}{L}\right)^2 / \phi = \tau / \phi$) thereby removing the tortuosity component and resulting in equation 3.4:

$$k = \frac{1}{\int F \sum_p^2} \tag{3.4}$$

*Fredrich et al.* [1993] computed pore geometric parameters (surface area to volume ratio and mean pore intercept length) using laser scanning confocal microscopy, and estimated the permeability of Fontainebleau samples using *Walsh and Brace*'s [1984] equivalent channel model. Their results indicated that for samples with relatively high pore fractions the predicted permeabilities compared well with laboratory measurements. However, the estimated permeability of one low-porosity sample deviated by more than one order of magnitude from its bench-top data. The authors argue that the equivalent channel model is appealing because of its simplicity and its direct relationship with physically meaningful and measurable microstructural parameters with. In a conclusion similar to that of *Doyen* [1988] they suggest that permeability prediction errors for low-porosity samples may be due to the mechanism by which pore geometry changes during diagenesis and porosity reduction, resulting in pore geometries that are not accounted for by the equivalent channel model.

Capillary pressure experiments determine the pressure required to force a non-wetting or wetting fluid through a pore system. The Lucas-Washburn equation (Washburn, 1921) correlates the fluid injection pressure with the pore throat radius. *Purcell* [1949], motivated to develop a technique to determine permeability from drill cuttings, proposes an equation to calculate permeability using mercury injection capillary pressure data. In developing the equation Purcell utilises Poiseuille's equation (eq. 3.5), which defines the rate of flow, $\frac{Q}{t}$, for a fluid with viscosity, $\mu$, through a tube with internal radius, $R$, and length, $L$, with a drop in pressure across the tube, $P$.

$$\frac{Q}{t} = \frac{\pi R^4 P}{8\mu L} \tag{3.5}$$

Purcell continues by incorporating the volume of the tube and the Young-Laplace displacement pressure equations into equation 3.5. By setting the resultant formulation equal to that of Darcy's Law for flow rate he arrives at an equation that computes permeability of a bundle of parallel tubes with equal length, but a range of radii, as a function of porosity and the capillary pressure and volume of the component tubes. He recognises that the arrangement of tubes is an unrealistic simplification of natural pore systems, in that the flow paths of porous rocks are typically interconnected and do not follow straight lines, but are tortuous. Tortuosity describes the interconnectedness of the pore system and is often defined as the ratio between the actual flow path length and the net displacement distance. The reciprocal of formation factor has been described as the retardation factor, or the electrical tortuosity ($\tau$) where $\tau = {}^{1}/_{F}$ (Clennell, 1997). Purcells therefore modifies his formulation by incorporating the formation factor, $F$, to produce equation 3.6, where $\rho$ denotes the percentage pore space occupied by the liquid, and the capillary pressure, $P_c$, is expressed in atmospheres.

$$k = 0.66F\phi \int_{\rho=0}^{\rho=100} \frac{d\rho}{(P_c)^2} \tag{3.6}$$

Purcell concludes that the mercury injection technique yielded similar results to that of the porous diaphragm technique, and the predicted permeability values for his test samples of Upper Wilcox and Paluxy sands are in good agreement with conventional laboratory measurements.

*Swanson* [1981], also interested in developing a method to determine permeability on small core samples and drill cuttings, points out that the gently rising values at low capillary pressure commonly seen in drill cuttings data (figure 3.1) tends to cause an over-estimation of permeability using the Purcell equation. Swanson also references *Thomeer* [1960] who develop a mathematical expression that describes log-log plots of capillary curves as hyperbola, which he then related with permeability. Swanson pointed out that capillary pressure data are not well represented as hyperbola resulting in questionable data from the Thomeer method. He considers drainage-type flow and the spatial distribution of the non-wetting phase. At low pressures when the non-wetting phase first enters the sample, its distribution is spotty, saturating only a small fraction of the connected pore system. Such low saturation values and the corresponding capillary pressures are not representative of the pore size that controls flow through the bulk system. Swanson suggests that connectivity between the majority of pores in the pore network is dominated by the effective porosity or saturation, which he defined as the point on a capillary pressure curve with the maximum mercury saturation to pressure ratio (the tangent point between the pressure curve and a 45$^{o}$ line $b - b'$. Swanson calculated the permeabilities of a range of clean sandstone and carbonate samples using equation 3.7, where $\alpha$ represents a formation constant and $S_b$ is the fluid saturation.

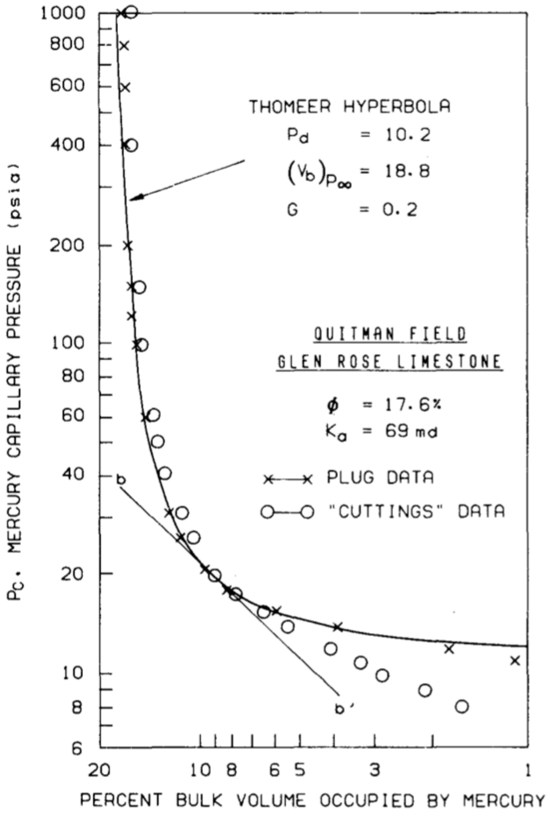

Figure 3.1: A capillary pressure curve showing a gentle rise in pressure during drainage and the 45° tangent line $b-b'$ [*Swanson*, 1981].

$$k = \alpha \left(\frac{S_b}{P_c}\right)_{max}^{c} \tag{3.7}$$

In a similar equation *Katz and Thompson* [1986] continues the use of the capillary pressure curves but instead use it to derive a pore system length scale they refer to as the characteristic length. The characteristic length can also be considered to be the effective pore throat diameter and is determined from the capillary pressure inflection point on the mercury intrusion curve, which they suggest corresponds with the establishment of a connected mercury cluster; only at this pressure does the non-wetting fluid spread in a connected manner from the inlet to the outlet of the sample. They propose an expression that relates permeability to a universal constant $(C)$, the characteristic length $(l_c)$ and the electrical conductivity $(\sigma/\sigma_o)$ (eq. 3.8). In the absence of grain surface conductivity the electrical conductivity is the inverse of the formation factor $(1/F)$, which captures the connectedness and of the pore system can be expressed in terms of tortuosity $(\tau)$ (Clennell, 1997). *Berg* [2014] provides an excellent summary of works related to permeability estimation in the context of characteristic length, tortuosity, and porosity.

$$k = Cl_c^2 \left(\frac{\sigma}{\sigma_0}\right) = Cl_c^2 \frac{1}{F} = Cl_c^2 \tau \tag{3.8}$$

In the context of detailed 3D imaging, the characteristic length can be given a precise geometric definition as the diameter of the largest sphere that can pass through the pore system. *Arns et al.* [2005] use parameters computed from µCT images to predict permeability using empirical methods, including Kozeny-Carman and Katz-Thompson, and correlate the results with Lattice Boltzmann simulated permeability. They conclude that for resolutions where it is possible to compute, the characteristic length provides the best measure of length scale to predict permeability.

## 3.2 Multi-scale µCT Imaging

As is described in section 1.3 the nature of µCT imaging equipment places unavoidable limits on the sample sizes for which images that accurately capture the pore system can be collected. The resulting challenge is that only a small portion of a sample can be imaged at any one time. This small volume is often not representative of the larger sample, especially in heterogeneous material, and it is often not economic or practical to collect more than 1 or 2 sub-samples for high-resolution imaging. A solution that partially solves this problem is to collect a low-resolution image of the whole sample that captures some portion of the sample heterogeneity and a high-resolution image of a small-scale sample that provides information on pore-scale fluid flow properties. *Latham et al.* [2008a, 2008b] describe a technique for the registration, or geometric alignment, of two or more digital images. In particular the technique makes it possible to register large-scale 3D images with one another, which, at the time of the publication, was a breakthrough capability. This was an exciting development as it is now possible to perform experiments, for example core flooding, on the same sample at different times and align the images that capture the results of those experiments to visualise and quantify any changes. Moreover, it is possible to physically collect a small-scale sample from a larger-scale volume, image it at high-resolution, and register the high-resolution image into a lower-resolution image of the larger scale sample. This approach forms the basis for much of the research reported in this thesis.

Many multi-scale imaging and analysis workflows currently in use rely on the visual assessment and classification of regions in a low-resolution image. In most cases it is assumed that there is no property variation within each class and the petrophysical properties computed from high-resolution images are assigned to their respective classes. This is an attractive concept for heterogeneous laminated sandstones such as the Precipice sandstone studied here. Visual assessment seems to indicate the presence of several repeating rock bands, which should, by all reasonable assumptions, have similar if not the same flow characteristics. However, chapter 4 presents evidence to suggest that a classification-based approach may not be ideal and to support the use of a statistical approach.

*Sok et al.* [2009] present a multi-scale imaging workflow for carbonate samples. They highlight the fact that carbonate rocks are naturally complex with pore structures ranging from nanometre to centimetre scale. To fully characterise and understand their fluid flow behaviour it is important to integrate information from a wide range of scales. They demonstrate the collection and registration of high-resolution 100 nanometre scale focussed ion beam scanning electron microscope (FIBSEM) images with 2 and 20 micrometre scale μCT images, thereby capturing and integrating information across a wide range of scales. Computed permeability from the FIBSEM data showed good agreement with core-plug scale permeability measured in the laboratory. The results clearly demonstrate that there is merit in collecting images at multiple scales with multiple voxel sizes to capture the range of fluid flow properties. It is also apparent that assigning flow property values to regions in lower resolution images rely on assuming that those regions are equivalent or similar based on some observable criteria, implying that region classification may improve the reliability of those assigned values. In a similar project *Grader et al.* [2010] make use of what they call a descending scale of μCT imaging whereby they collect a low-resolution image of the whole core and higher resolution data for successively smaller samples that capture the pore-scale details of a heterogeneous carbonate sample.

*Golab et al.* [2010] study tight sands and use a multi-scale multi-analysis approach by combining not only gray scale μCT images, but also high-resolution SEM and compositional mineral maps of thin-sections taken from the same rock volume. Instead of collecting and aligning low- and high-resolution CT images they collect two 3D images of the same sample volume: one in a dry state and another after the sample was flooded with an x-ray attenuating fluid. The approach assumes that the attenuating fluid occupies the pore spaces and is displayed with high gray scale values in a tomogram. Subtracting the aligned dry and wet images from one another produces a 3D map of the sub-resolution micro-porous spaces previously not visible in the dry image. In addition to dry and wet 3D imaging the authors register high-resolution 2D SEM images and mineral maps generated using and automated SEM-EDS method into the 3D volume. The combination of these data sets identifies and maps the specific minerals associated with the micro-porous component of the pore system, in this case illite, muscovite, and chlorite. This mapping is not limited to the 2D plane of the SEM images, but can be extended to the 3D image using the tomogram gray scale values associated with these minerals. They argue that their data suggest the conventional assumption that pores in tight sands are connected by "slot-like" pore throats is not always accurate. In this instance the "slot-like" pore throats contribute relatively little to the overall porosity and are generally smaller than 200 nm in thickness, which lead them to conclude that the micro-porous regions represent significant pathways for fluid flow.

A classification-based approach was used by (Bai et al., 2013) who also investigate the microscopic pore structures of tight sandstone from the Yanchang formation. They collect a μCT image of a 2.54 cm diameter core plug, in which they identify three units based on the characteristics of the pore system. One unit has very low porosity with very few pores. Unit two comprises a well-developed pore network with relatively large pores and connecting throats, while unit three shows a network of micro-fractures. They make use of nano-CT images to characterise sub-samples from each of the units and assign property values to the larger-scale core plug. In their study *Yan et al.* [2013] describe the core and pore scale characterisation of the Liujiago sandstone, from the Ordos Basin in northwest China for potential $CO_2$ injection and storage. They collect low-resolution medical- and μCT images of the sample that show the presence of laminations. Petrographic thin-section descriptions confirm that the laminations are the result of increased proportions of fine-grained rock fragments, mica, and porosity. In this instance the authors do not attempt to perform any classification and instead collect three sub-samples for high-resolution μCT imaging to better understand the distribution of rock and flow characteristics.

*Khalili et al.* [2013] focus on carbonates and investigate the use of porosity-permeability relationships derived from μCT images and the resulting calibrated porosity maps to constrain permeability estimates in larger-scale lower resolution μCT images. This method is significantly different to using a classification-based approach to assign property values at the larger scale. In addition to predicting permeability they also perform data upscaling to compute the effective permeability. Their results indicate that the experimental and predicted permeability agrees at larger scale; however, at smaller scales the numerical results tend to underestimate permeability relative to the experimental values. They argue that upscaling techniques that rely on averaging cannot accurately account for high permeability contrasts and therefore do not provide accurate vertical flow information at the small scale. Capturing variability is a constant challenge in upscaling and is beyond the scope of this thesis.

Studying gas transport in a shale reservoirs *(C. Chen, 2016)* uses multi-scale imaging to characterise the pore-scale geometry of porosity found in kerogen and the inorganic matrix of Middle Eastern and Eagle Ford shales. His results support the use of a dual-porosity in which the gas flow within the kerogen component is dominated by non-linear desorption and adsorption and molecular diffusion, while in the matrix component viscous flow is mainly driven by a pressure gradient. History matching of the model suggests that it accurately captures the dramatically different flow rates introduced by the kerogen and matrix components in a shale reservoir.

### 3.3 Contributions of this Work

This thesis explores the fundamentals of predicting the spatial variations in absolute permeability and parameters of capillary pressure of heterogeneous sandstone from high field of view tomographic images whose resolution is not sufficient to allow their direct computation. Surprisingly there is very little existing literature on this topic of cross-scale correlations, and I suggest it is because cross-scale alignment of high-resolution 3D tomograms is fundamentally difficult. The unique contribution of this work is the development of a workflow that combines existing analytical techniques to predict and map the spatial distribution of fluid flow properties in large field of view CT images, such as images of whole core, where they cannot be computed directly by numerical methods. The petrophysical properties of interest are absolute permeability and parameters derived from capillary pressure curves, including threshold pressure and residual non-wetting phase saturation. This workflow predicts the fluid flow properties of many small homogeneous regions within low-resolution images, thereby providing information that is unavailable from bulk laboratory techniques. Unlike classification-based or neural network approaches this method is based on statistical correlations between petrophysical parameters computed from regions in high-resolution images with rock characteristics determined from the same regions in low-resolution images. Direct linear regression methods are well-constrained thereby producing results that are simpler to interpret in terms of the physical meanings of the predictor rock characteristics.

Segmentation of lower resolution images (binarizing the image) typically eliminates much of the gray scale information related to pore geometry. In addition to macro-scale quantities such as porosity and pore size, this work explores the use of a segmentation technique that preserves gray scale information and allows the computation of characteristics that incorporate image gray scales. Such characteristics should have the potential to correlate well with geometry-dependent properties like permeability.

Fluid flow properties are computed directly on high-resolution images by numerical solution, while characteristics such as open pore fraction, pore size and formation factor are calculated from low-resolution images and used as predictor variables of those properties.

The essential steps in the workflow used in this study are:

1. Acquire a low-resolution (LR) 3D image of a core sample that spans a relatively large volume of the rock (in this work: 25mm diam. x 80mm long).
2. Acquire an intermediate-resolution (IR) 3D image of the same core sample that spans a relatively large volume of the rock (in this work: 25mm diam. x 80mm long).
3. Acquire a high-resolution (HR) 3D image of one or more sub-samples of the core, and compute directly the permeability on homogeneous regions within each image. In total, the sub-samples should span the bulk of the rock texture variability.
4. Digitally align the low- and high-resolution images to locate the overlap region.
5. Calibration: determine statistical correlations between petrophysical properties (from HR image) and rock characteristics (from the aligned overlap region of the IR and LR image). Develop statistical correlations using response and predictor data from exactly the same physical rock volumes represented by different resolution images.

6. Prediction: Calculate rock characteristics for the LR image of the core plug and/or whole core from step 1 and predict fluid flow parameters using the statistical correlations from step 4.

Optionally, the workflow may include more than three levels of imaging to span a larger range of length scales. In the context of reservoir-scale modelling and simulation the predicted petrophysical properties obtained from this workflow can ultimately be used to compute effective permeability at the core scale by means of Darcy simulation techniques (Kløv et al., 2003).

# 4 Methods

## 4.1 Sampling and Multi-Scale Imaging

This thesis reports on two core plug samples (sample 1 and sample 2) from the Precipice Sandstone in the Surat Basin, Australia, which can be considered a good example of relatively clean siliciclastic aquifer rock. The samples are 25mm in diameter and 80mm tall and form the basis for developing the previously described flow property prediction workflow. Samples 1 and 2 were collected at 1195.39 m and 1217.32 m respectively. Chapter 5 (Permeability Results and Discussion: Sample 1) discusses the development of the workflow in the context of the results from sample 1, followed by chapter 6 (Permeability Results and Discussion: Sample 2), which reports on the main results from sample 2. Chapter 7 discusses the results for the modelling and prediction of parameters derived from capillary pressure curves. The core plugs were imaged in 3D using a helical scanning µCT system at The Australian National University (ANU), Canberra, Australia, by FEI staff members who assisted with data collection. Image analysis was conducted using the Mango image analysis software and custom data processing scripts created in Python during the course of the project.

The 25 mm core plugs were first imaged rapidly as part of a bundle with other cores to produce image 1) a low-resolution image (LR) at ~64 and 61 µm/voxel for samples 1 and 2 respectively, after which image 2) an intermediate resolution image (IR) at ~16 µm/voxel was acquired through a high-fidelity scan of the core plugs in isolation. Finally, image 3) a high-resolution image (HR) at ~5 µm/voxel was acquired through physical coring and imaging of a 8mm diameter 15 mm long sub-plug from the original core plug of sample 1. The high-resolution image for sample 2 was collected using a 'region of interest scan' (see chapter 7). The three images for each of the core plugs are aligned to one another using a distributedmemory parallel cross-scale 3D image registration algorithm described in section 4.2 (Latham, Varslot, & Sheppard, 2008; Latham, Varslot, Sheppard, et al., 2008). In addition to the high-fidelity imaging of significant sample heterogeneity across multiple scales, this imaging program enables the study of cross-scale correlations because of precise voxel to voxel registration of the images to each other. The overlap regions between the images provide information at all three resolutions; therefore, the statistical calibration step is restricted to the domain of the high-resolution image. After registration one is left with the following image pairs:

a. 5 μm/voxel HR image overlapped with the 16 μm/voxel IR image,
b. 5 μm/voxel HR image overlapped with the 64/61 μm/voxel LR images,
c. 16 μm/voxel IR image overlapped with the 64/61 μm/voxel LR images

Figure 4.1 shows the difference in resolution between the images and the approximate location of the sub-plug for sample 1. The location for collecting the sub-plug was selected for both practical and analytical considerations. Based on visual assessment, the sub-plug location was selected to provide the best sampling across the range of relatively fine, medium, and coarse textures. The coarsest lamination in the sub-plug is poorly cemented and necessitates an 8 mm diameter sub-plug to avoid sample damage that may occur during coring to a smaller diameter. Furthermore, the 8 mm diameter makes it possible to collect reliable data on a larger volume of the coarsest lamination. Given the configuration of the μCT imaging equipment the 8 mm diameter sub-plug can be imaged with a maximum resolution of ~5 μm/voxel, which is sufficient to accurately represent the pore system in all three rock textures. As I discuss in section 4.1.4 it is worth noting that the analytical results may be affected if the sub-plug is chosen in such a way that it does not represent the range of rock textures present in the larger scale sample, or if it is too large for accurate imaging of the finest textures in the heterogeneous pore system. Since the images were not constructed through a digital down-sampling procedure, they all contain real imaging artefacts such as noise and blur.

The original schedule included working on a set of 16 samples; however, as the research progressed several obstacles prevented this from occurring. Significant amounts of time were spent on the initial development and testing of analytical methods, procedures, and results visualisation. The results from the analysis of the first sample created several fundamental questions along the way, which required extra time to investigate and document. At the time of analysing the second sample I discovered that the choice of imaging method for the remaining samples (region of interest scans) introduced deficiencies in the data that prevented property predictions to be made. At this stage there was no longer time to conduct new experiments on these samples.

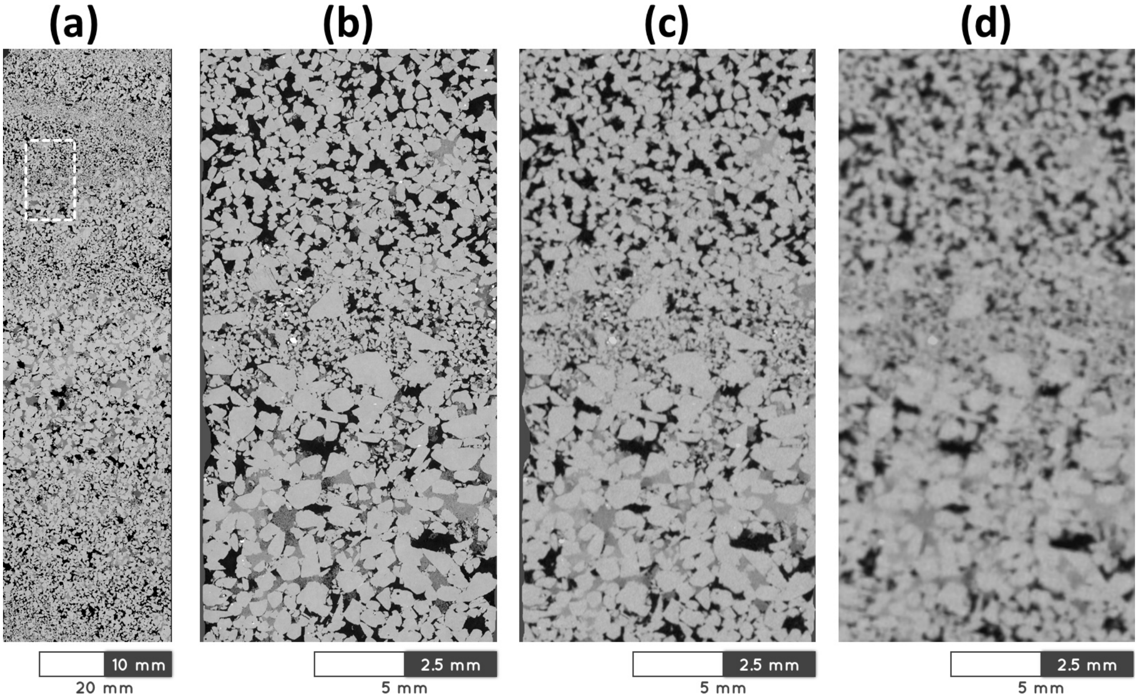

Figure 4.1: a) The 25 mm core plug of sample 1 imaged at 16 μm/voxel; b) the 5 μm/voxel image of the 8 mm sub-plug; and the overlap regions from the 16 μm/voxel and 64 μm/voxel images (c and d respectively). The white square indicates the approximate location of the 8 mm sub-plug.

Figure 4.2 shows 2D slices, gray scale histograms and intensity profiles of select regions of the registered low-, intermediate-, and high-resolution images. The reduction in image resolution causes significant smoothing of the intensity profile and the inability to capture smaller features is evident. Furthermore, the intensity histogram of the 64 μm/voxel image shows an overall increase of intermediate gray scale values due to spatial averaging (blurring), which results in many regions of the pore space, most notably the pore throats, being completely occupied by intermediate gray scale values.

The resolution of images 1 (LR) and 3 (HR) differ by a factor of 13, corresponding to a reduction in volumetric sampling density of over 2000, i.e. image 1 can cover a volume 2000 times larger that of image 3, given an image of the same number of voxels.

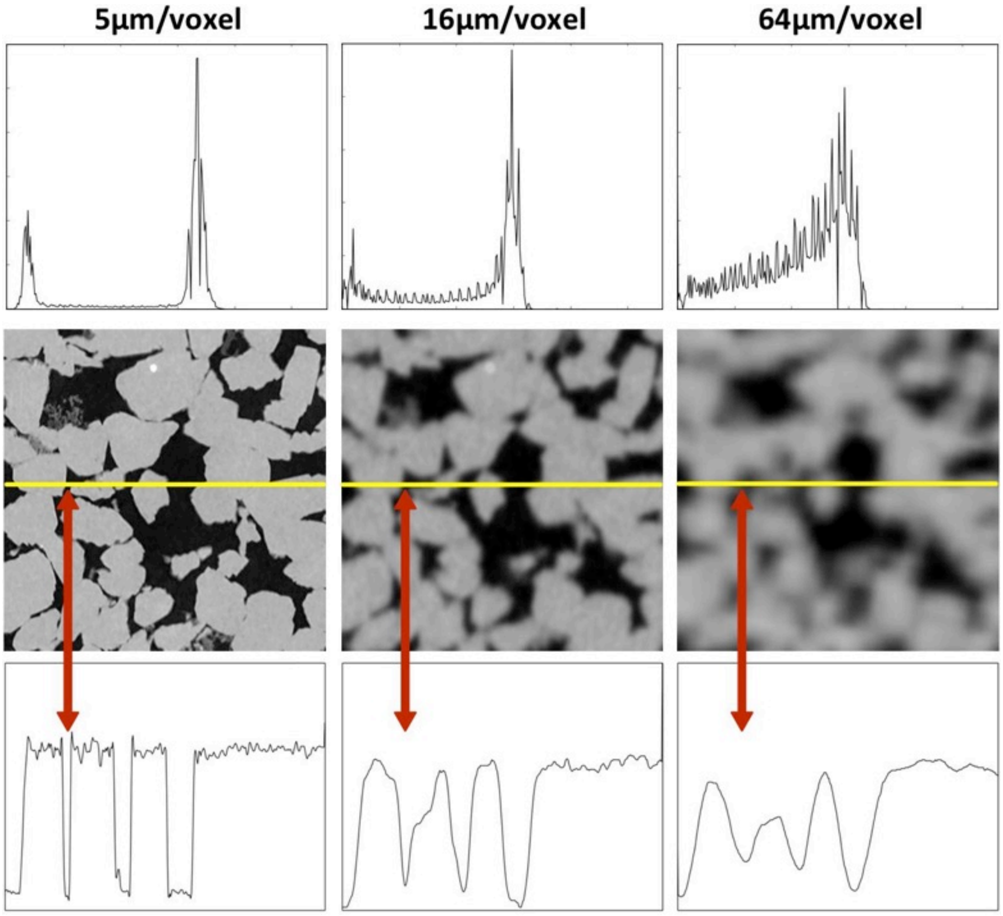

Figure 4.2: Close-up regions taken from the three different resolution images. Each image has an accompanying gray scale histogram above and intensity profile below (indicated by the yellow lines). Note how the change in resolution is reflected in the smoothing of the intensity profile. The red arrows indicate a narrow part of the pore space, which is resolved in the high-resolution image, but represented by intermediate gray scale values in the low-resolution image.

## 4.2 Image Segmentation

Conventionally the 65535 grey levels in the 16-bit gray scale images are arranged into a smaller number of phases, with each phase representing a different class of material. Typically the segmented phases are: pore, intermediate phase (clays), and solid phase (framework minerals). However, segmentation generally causes a loss of geometric information contained in the image gray scales. Figure 4.3a and b show how pore throats may be closed during segmentation and how corners and crevasses of pores are not always accurately represented by a segmented image, especially at low-resolution. Here we make use of a two-stage segmentation method. First, using the converging active contour method (Sheppard et al., 2004), where the gray scale values are divided into three main phases; and second, a ‘soft’ thresholding segmentation procedure (micro-porosity segmentation) allocates 100 gray levels to intermediate intensity voxels to build a porosity map, which includes sub-resolution pores within the intermediate phase (figure 4.3c). Each voxel in the intermediate phase is assigned a value based on a linear interpolation between a minimum and maximum attenuation value corresponding to 100% pore and 100% grain respectively (Sok et al., 2009). This process assumes that the intensity of each intermediate-phase voxel in the image is linearly related to the porous fraction of that voxel. This is a tolerable assumption for the very simple mineralogy of the Precipice Sandstone studied here; however, for more complex rock types it would be necessary to perform more reliable porosity mapping using a method such as the multi-image wet/dry imaging workflow described in *Sheppard et al.* [2014].

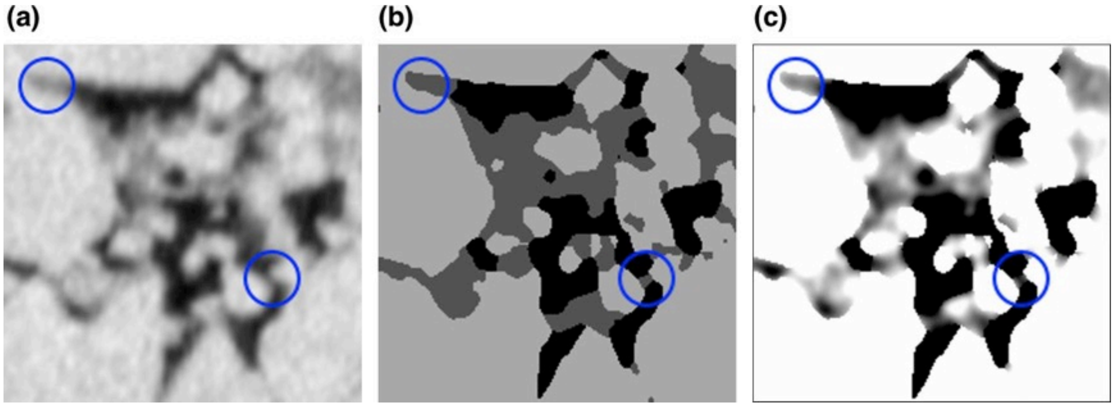

Figure 4.3: 2-dimensional slices from a 16 μm/voxel gray scale tomogram (a), the equivalent segmented (binarized) image (b), and the image produced by the micro-porosity segmentation method (c). The blue circles indicate regions where the intermediate gray scale values from the tomogram (a) are lost in the segmented image (b), while the micro-porosity segmentation is able to retain the gray scale information (c).

## 4.3 Image Unitisation

The samples used in this study contain significant heterogeneity with fine-, medium-, and coarse-grained bands (figure 2.6 and figure 4.1). To improve the probability of identifying correlations between rock properties and petrophysical properties a unitization procedure (step detection) was developed during the course of this project to identify internally homogeneous zones, or units, to be characterised individually. Log-type data, similar to time-series data, are ideally suited for analysis by step detection techniques. For example, in voice recognition software step detection is critical for the identification of the beginning and end of words within the audio signal (Li et al., 2002). Step detection analysis has also been applied to downhole well-logs by Gill [1970].

The method for µCT image unitisation presented here makes use of the gradient profile (rate of change) of the grain size and open pore fraction profiles to identify points of maximum rate of change along the length of the core sample. These points of maximum gradient are considered potential boundaries between units. I should emphasize that this procedure is not intended for rock classification. It serves to isolate internally homogenous zones within the image for individual characterisation with minimal overlap between adjacent yet distinct image volumes. Furthermore, it is worth noting that the procedure presented here operates on grid-aligned µCT data and is intended for use on core samples with approximately horizontal laminations. A different unitisation method would need to be considered for strongly inclined laminations.

### 4.3.1 Generating Unitisation Input Data

The phase volume profiles, which includes open pore fraction and all phases separated during the image segmentation step, are generated slice-wise from the 3D segmented data file by computing the phase fractions in each z-slice (orthogonal to the vertical axis) of the image, resulting in a representation of the phase fractions resembling a downhole geophysical log, albeit at a much smaller scale. The grain size log is generated by first using the segmented data file to define a Euclidean distance map, which, for each voxel, assigns a value equivalent to the shortest distance to a boundary voxel (Danielsson, 1980). The next step is to apply a covering radius transform (CRT) (Hazlett, 1995) to the grain phase, which is equivalent to the repeated application of morphological opening in which the structuring elements are the complete set of Euclidean balls up to the largest inscribed radius of the grain space. For practical purpose related to Mango software design and implementation, to allow the generation of log-type data from the CRT image one must use the segmented file to mask all components of the CRT image except the grain component (to which the CRT transformation was applied). It is now possible to convert the resulting image to a tomogram-type file and then compute the grain size log. A pore size log was also created using this procedure, however, because the grain phase is numerically dominant the pore size log was excluded for use in the unitisation procedure.

The small sampling interval of one z-slice (i.e. the height of one voxel) in combination with high but non-uniform levels of high-frequency fluctuations in the logs, necessitate a smoothing operation before the profile gradients are computed and the gradient analysis is performed. Conventional time series data such as audio, weather, or financial data can be smoothed using a rolling average with constant window sizes, however, given that the µCT log data are generated from rock volumes with spatially varying properties, a dynamic window size is calculated based on grain size. For each z-slice the averaging range ($r$) is given by the scaled ratio between the voxel size ($v$) and the mean grain size ($gs$) from the CRT analysis described above (eq. 4.1). The non-uniform smoothing implemented here is based on the hypothesis that to achieve a representative average for any given z-slice, the averaging window must be small enough so that the data do not contain sharp fluctuations resulting from individual grain CRT values. It could be argued that a separate smoothing range ought to be computed for the open pore fraction profile; however, here grain size is considered the dominant geological feature that controls the occurrence of visually distinct laminations, which are the features targeted for separation by the unitisation procedure. Therefore, the averaging range computed from the grain size profile is applied to both the grain size and open pore fraction logs.

$$r = \frac{1}{50} * \frac{v}{gs} \tag{4.1}$$

The main reason for smoothing the grain size and open pore fraction profiles before computing their gradients is to reduce the amount of high-frequency fluctuation in the gradient profiles, which would render them unusable for identifying points of maximum rate of change. Even with this smoothing operation (explained above) the resulting gradient profiles contain significant amounts of high-frequency variations, forcing another smoothing operation. Unlike the grain size and open pore fraction profiles, gradient is a consistent measure of instantaneous rate of change. Additionally, given that small scale fluctuations as a result of adjacent yet distinct µCT volumes have been accounted for during the dynamic smoothing of the grain and open pore fraction profiles, here the gradient logs are further smoothed using a constant averaging range of 100 z-slices. Figure 4.4 demonstrates the progression from raw data to smoothed profile and gradient logs for the grain size characteristic.

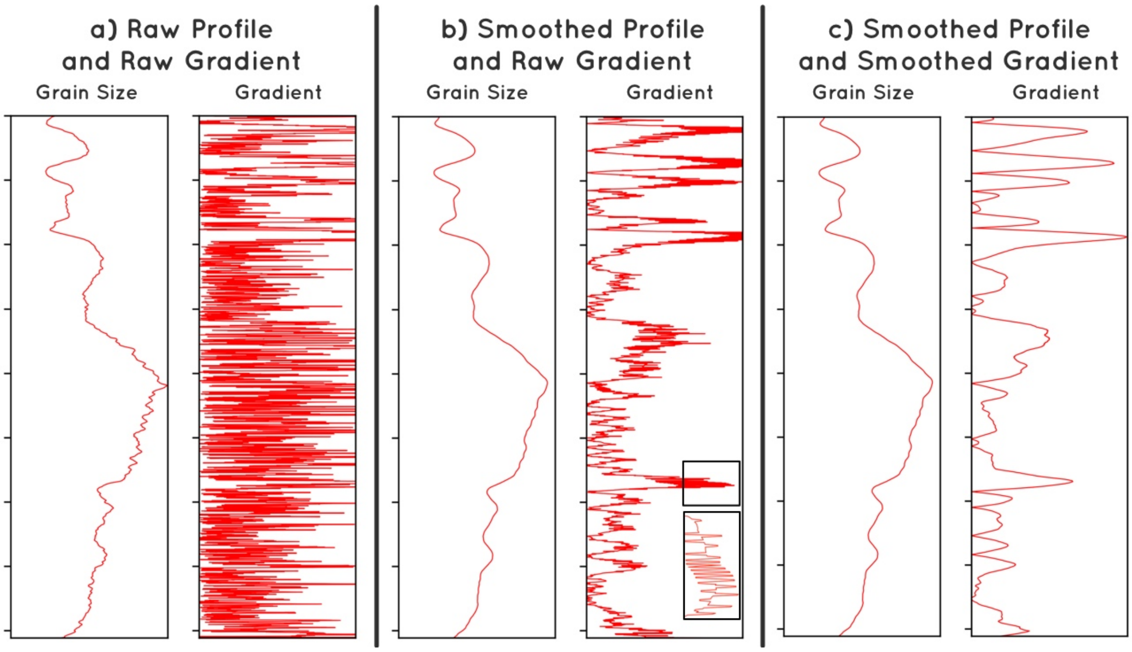

Figure 4.4: Showing the effect of the profile and gradient data smoothing operations. From left to right, the raw grain size profile and raw gradient (a), the smoothed grain size profile with the raw gradient of the smoothed profile (b), and the smoothed grain size profile and the smoothed gradient (c). The inset as a part of (b) indicates the nature of the high-frequency fluctuations that can affect analysis of the gradient profile without a smoothing operation.

### 4.3.2 Gradient Profile Analysis

The objective of the gradient analysis is to identify points of maximum rate of change along the grain size and open pore fraction gradient profiles. The gradient profiles contain positive and negative gradient values. For simplicity the absolute gradient is used as input for the analysis. The first step locates a set of local maxima as the initial candidates for points of separation (transitions or boundaries) between distinct yet adjacent units. For any given gradient profile the number of boundaries could be very large (up to several tens of boundaries), therefore, to produce a realistic number of transitions the second step of the analysis makes use of a user adjustable parameter to reduce the number of initial transitions. The parameter is a number ($x$) of standard deviations ($\sigma$). For each initial transition the analysis compares the mean values ($\mu$) of adjacent units, in this case the characteristic values are grain size and open pore fraction. If the mean values for one of the adjacent units are smaller than $x * \sigma$ of the other unit the transition is removed and the adjacent units are joined. The mean and standard deviation for the adjacent units are computed by using the individual z-slice values to define the variance. For example, unit a and unit b are separated by a transition boundary identified as a local gradient maximum. If $\mu_a < x * \sigma_b$ or $\mu_b < x * \sigma_a$ the transition is removed. This analysis is an iterative process and terminates when no more transitions are identified for removal. Selecting the $x$ parameter is the only user input required for the unitisation procedure; all other steps are automated and occur when running the algorithm. In image processing terms the procedure might be considered a one dimensional watershed analysis (Beucher & Meyer, 1992). As a final step the grain size and open pore fraction profiles are joined to produce a single unitisation result where adjacent units are considered unique in terms of both grain size and open pore fraction.

### 4.3.3 Applying Unitisation to Data

In summary, the unitisation procedure follows these main steps:

1) Generate the open pore fraction and grain size logs from the µCT image and apply smoothing operations.
2) Compute the gradients of the open pore fraction and grain size logs at each point along the length of the profiles and apply the smoothing operations.
3) Determine the local gradient maxima, which forms an initial division of the sample into a maximal number of units.
4) Iteratively compare adjacent units and their properties. If the mean grain size or open pore fraction values for two adjacent units are within a predefined number of standard deviations (the number of standard deviations are adjustable), the boundary separating the units is removed, and the routine returns to re-calculate the updated unit properties and re-compare adjacent units.
5) When the routine converges, i.e. no more boundaries are identified for removal, the unitisation result from the open pore fraction and grain size log analyses are combined, thus defining units in which both the grain size and open pore fraction are considered distinct from their neighbours.

The unitisation procedure is applied to the IR image at 16 µm/voxel (figure 4.5a) and the HR image at 5 µm/voxel (figure 4.5b). The unitisation results from the HR 5 µm/voxel images are used to define the unitisation of the IR 16 µm/voxel and LR 64 and 61 µm/voxel images in the regions where they overlap the HR images. The unitisation results from the 16 µm/voxel image are used to define the unitisation of the LR 64 and 61 µm/voxel images of the 25mm core plug.

The procedure is not intended for unsupervised operation. It is likely that after an initial attempt the user adjustable number of standard deviations, which controls the comparison step between adjacent units, would need adjustment to arrive at what the user deems a reasonable result. In some cases one of the logs may not show enough variation to warrant unitisation based on that parameter. The number of standard deviations can be used to effectively turn off the analysis of either log by being set to 0. Figure 4.5b shows such an example in the HR image of the sub-plug for sample 1, in which the open pore fraction log shows relatively little variation and was turned off for analysis.

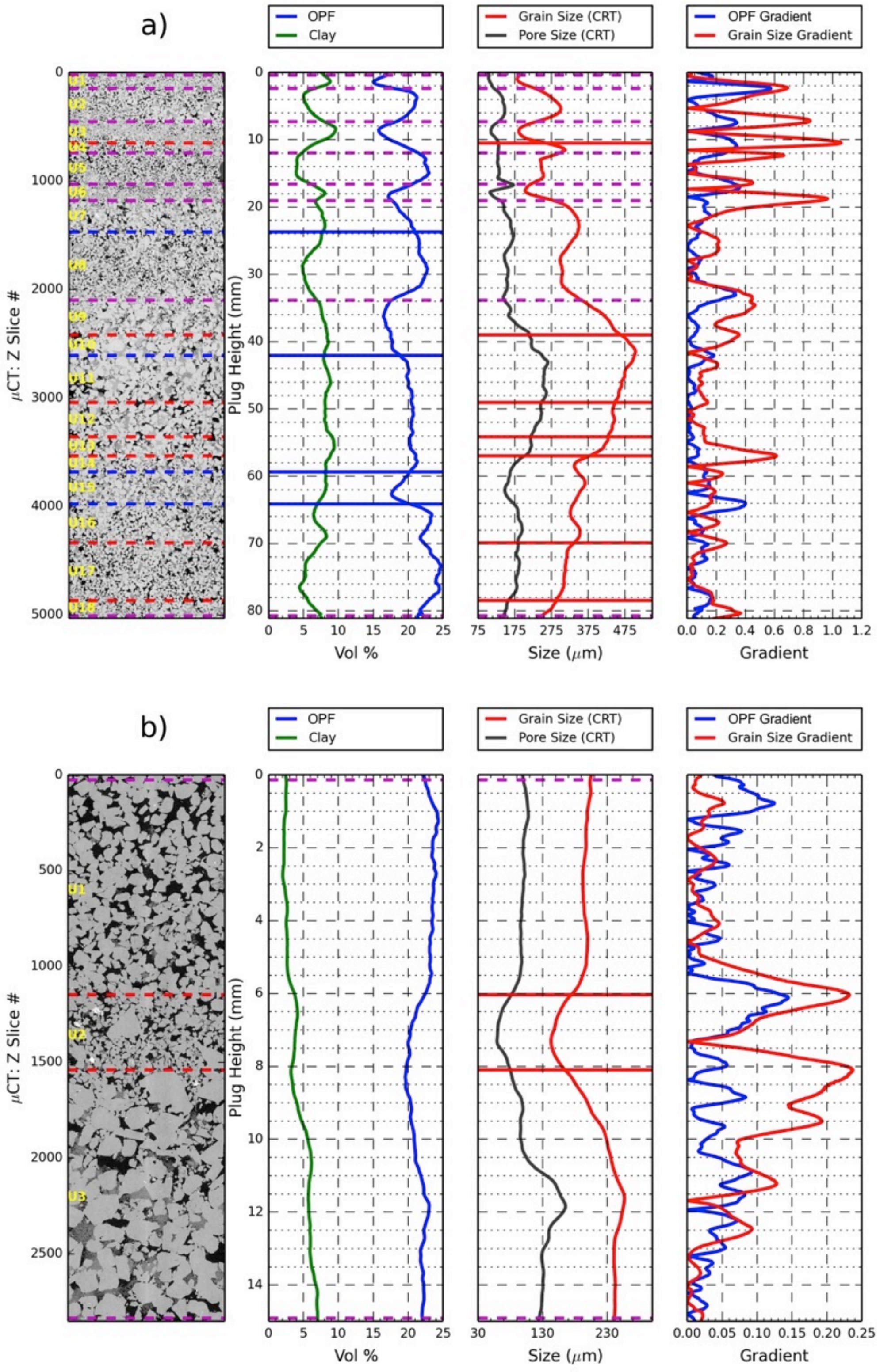

Figure 4.5: a) 25mm plug image unitisation, and b) 8mm sub-plug image unitisation. Horizontal red lines indicate boundaries from the grain size log. For this sample the open pore fraction profile (OPF) does not contain sufficient variation to warrant unitisation, which was therefore switched off.

## 4.4 Absolute Permeability

Simulations of absolute permeability (k) were performed using the Morphy software suite (Christoph H. Arns et al., 2001, 2004). Permeability is calculated using the D3Q19 (3 dimensional lattice with 19 possible momenta components) Lattice-Boltzmann method (Qian & Zhou, 1998). The fluid, which is represented by a series of particles during the simulation, is placed under a pressure gradient by a body force (Ferréol & Rothman, 1995; Martys & Chen, 1996). One of the key advantages of this method is that permeability computations can be performed on multiple small volumes of μCT data, thereby generating statistically large numbers of data points.

## 4.5 Capillary Pressure Curves

### 4.5.1 Pore Morphology

There are several ways to compute drainage and imbibition flow in digital images of porous rocks, which include methods that solve directly for the Navier-Stokes flow equations, methods that make use of pore morphology, and methods based on pore network models.

Pore-morphology-based methods make use of transformation procedures that express the pore system as covering radius transform (CRT) (Hazlett, 1995) maps. These morphology-based methods have the advantages of taking into account the full pore geometry, including corners and crevices near the connecting pore throats, being computationally efficient, and they can be used on the same small volumes used for permeability simulations. The disadvantage of morphology-based methods is the assumption of a zero contact angle between the wetting and non-wetting phases, i.e. it cannot incorporate wettability or hysteresis affects, which means they cannot compute irreducible wetting phase saturation under drainage flow or the irreducible non-wetting phase saturation under imbibition flow (Hilpert & Miller, 2001). Regardless of these disadvantages, the fact that simulations could be performed on the same volumes used for the IR and LR image characterisation and permeability simulations, and their computational efficiency, I made use of pore morphology-based methods to compute drainage and imbibition flow capillary pressure curves to be used for parameterisation and then regression analysis (see chapters 8 and 9 for a detailed discussion on the methods and results).

### 4.5.2 Network Models

An alternative method makes use of network models, which represent the pore system as a series of idealised shapes with larger pore bodies connected by smaller pore throats (Oren et al., 1998). In an excellent review paper on pore network models and multi-phase flow simulation *Blunt* [2001] emphasises that one of the major challenges in the use of pore-scale models is to determine the level of detail required in a description of the pore system to allow reliable predictions of fluid flow properties. He explains that traditional methods of representing the pore system as spheres and cylinders essentially allow only one phase to occupy the system. Given the more realistic scenario of multiple phases present in the pore network, higher accuracy models representing pores as shapes with irregular triangular cross-sections allow the simulation of different flow behaviour in the corners and centres of the pores, which are typically occupied by the wetting and non-wetting phases respectively. Such models were successfully used by *Oren et al.* [1998], *Lerdahl et al.* [2000], and Bultreys et al. (2016) to produce good predictions of relative permeability, while Bultreys et al. (2016) simulated secondary water-flooding in heterogeneous rocks with diverging wettability characteristics. With the ability to now account for wettability, capillary pressure flow simulations can more accurately compute parameters such as non-wetting phase saturations and demonstrate a more realistic hysteresis effect. The extensive use of network modelling to generate capillary pressure curves is not within the scope of this project. However, I generate a small dataset to recognise and demonstrate the benefits of network modelling for multi-phase flow simulations (see chapter 10 for a discussion on the methods and results).

## 4.6 Computing Predictor Rock Characteristics

To increase the number of data points for use in statistical correlations (see section 4.7) each unit identified in the unitisation procedure described in section 4.3 is subdivided into a series of approximately cubic sub-volumes. Petrophysical properties and predictor rock characteristics are computed for each sub-volume, and, therefore, each unit separately. It is now appropriate to introduce the concept of a representative element volume (REV), a volume, or a scale of observation, for which parameters such as porosity and grain size are constant (Al-Raoush & Papadopoulos, 2010). The top and bottom boundaries for the sub-volumes for each unit are chosen to match those from the unitization results, while the x and y dimensions are chosen so that the resultant sub-volume approximates a representative element volume (REV) of that unit. The concept of the REV further implies that measuring a parameter in a sub-volume would yield a comparable result relative to measuring that parameter in the whole unit. The approach of analysing several sub-volumes for each unit has the benefit of capturing both the inter- and intra-unit variability for the petrophysical properties and predictor characteristics. The x,y,z voxel dimensions of the sub-volumes for sample 1 are: unit 1 = (330, 330, 330), unit 2 = (330, 330, 392), and unit 3 = (425, 425, 425). Figure 4.6 demonstrates how the computation of rock characteristics (grain size, pore size, and porosity) is impacted by the choice of sub-volume size. Here I investigate changing the sub-volume size for unit 3 from sample 1 (see section 4.3.3 and figure 4.5). Unit 3 is the coarsest grained unit of the three units. Initially the computed values change dramatically as the volume of the subset increases, however, at some stage the computed values reach a point of relative stability. Unit 3 was ultimately chosen with x, y, and z dimensions of 425 voxels$^3$, which according to the data in figure 4.6 (see stippled line) is a point of relative stability for computed values of grain size, pore size, and porosity. Units 1 and 2 are both finer-grained, and I conclude that ~330 voxel$^3$ dimensions for units 1 and 2 represent REVs for those units.

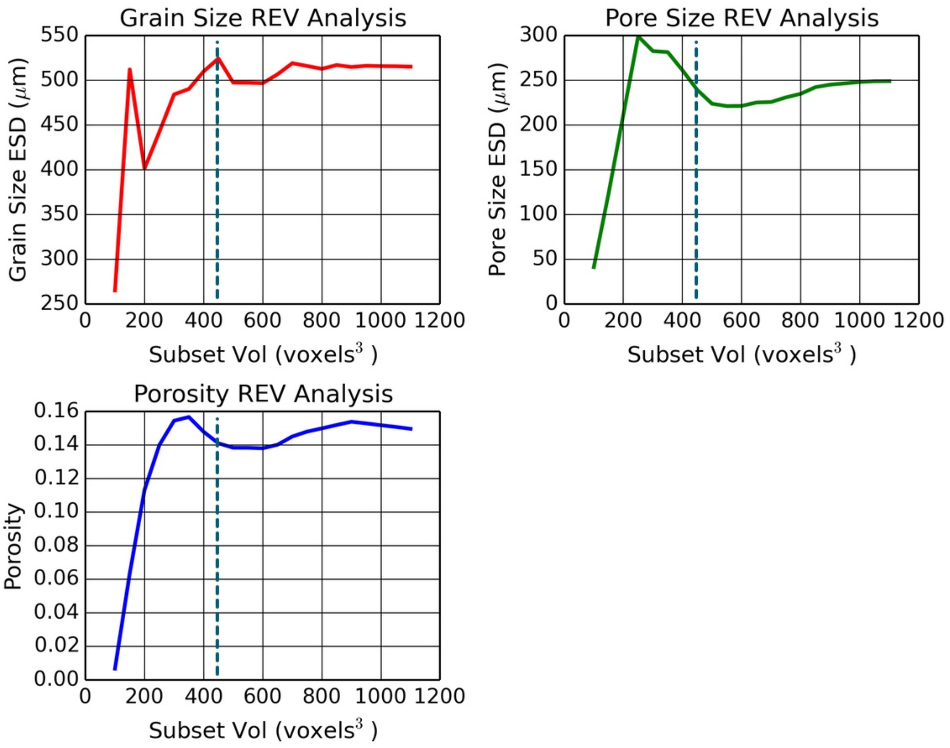

Figure 4.6: Demonstrating the changes in computed characteristics values with changes in sub-volume voxel dimensions. The stippled lines indicate the voxel dimensions for unit 3 at 425 voxels$^3$.

As described in section 4.7 (Statistical Methods), the statistical correlations are developed using response data (absolute permeability and capillary pressure) from the HR images and predictor characteristics from the IR and LR image sub-volumes. The sub-volumes from each image resolution represent exactly the same physical rock volume from different resolution images. The exact alignment of sub-volumes between images is achieved by conducting digital image registration explained in section 4.1.

### 4.6.1 Grain and Pore Size and Sorting (GS, Gsort, PS, and Psort)

To compute grain and pore size and sorting I use the segmented data to construct a Euclidean distance map, which, for each voxel, assigns a value equivalent to the shortest distance to a boundary voxel (Danielsson, 1980). The distance map is further processed by a watershed transform (Beucher & Meyer, 1992), followed by the merging of labelled watershed regions, which generates a partitioning of the grain or pore space into individual grains or pores (A. P. Sheppard et al., 2006; Thompson et al., 2005). An analysis of the volumes of regions bins the regions into size classes expressed in number of voxels, which is converted to equivalent sphere diameter (ESD) (Jennings & Parslow, 1988). Assuming a log-normal distribution, a cumulative logarithmic ESD size distribution curve is used to calculate the median grain and pore size in micrometres for each sub-volume (Krumbein, 1934). I express grain and pore sorting as a measure of spread using the 5th, 16th, 84th, and 95th percentiles from the size distribution curves (Folk & Ward, 1957).

### 4.6.2 Open Pore Fraction (OPF), Porosity (Po) and Clay Fraction (CF)

Here I make use of the segmented data files that represent the original gray scale tomograms in terms of three classes representing a) open pores as low brightness voxels, b) clay and sub-resolution porosity as intermediate gray scale voxels, and c) the grain phase as high brightness voxels (figure 4.3b). Summing the number of voxels in each class and normalizing to the total number of voxels in the image gives the fractional contribution of each class. Open pore fraction is the fraction of resolved void space clearly distinguished from the intermediate and grain phases. As mentioned in section 2.2 on image segmentation, I use a ‘soft’ thresholding segmentation method, which starts with a simple three-phase segmentation of the image into pores (low gray scale values), clay and sub-resolution pores (intermediate gray scale values), and grains (high gray scale values). The next step places low and high gray value thresholds (automatically chosen by the analysis software) on the intermediate gray scale intensity voxels and rescales the voxels within the thresholds to a range between 0 and 100 grey scale values (figure 4.3c). Based on a linear interpolation between a minimum and maximum grey scale value, I compute the fractions of clay phase and sub-resolution pores for the range of intermediate gray scale voxels. By adding the fraction of sub-resolution pores to the open pore fraction I determine the porosity value (Sok et al., 2009). The fraction of clay phase is computed as the difference between one and the sum of the fraction of solid phase (grains) and porosity (the sum of the open pore fraction and sub-resolution pore fraction). Both the clay fraction and porosity characteristics are therefore computed as a function of the intermediate gray scale voxels. It is important to note that the intermediate gray scale voxels represent sample volumes physically occupied by clay mineral phases and the boundaries between the grain and pore phases.

### 4.6.3 Formation Factor (F)

In this thesis I compute and report the Formation factor by numerically solving Laplace's equation using a finite difference formulation to solve for the potential in a unity strength electrical field (C. Arns et al., 2002; Christoph H. Arns et al., 2001). The formation factor $(F)$ of each gray scale voxel (including completely resolved pore voxels with 100% porosity) is given by Archie's law $F = \phi^{-m}$ (eq 2.6), where $m$ is the cementation exponent and $\phi$ the porosity. Using conventional experimental data the $m$ exponent can be computed as the slope of a plot of the logarithm of formation factor and the logarithm of porosity. The numerical computation of formation factors requires a predetermined value for $m$. *Archie* [1942] found that $m$ ranges between 1.8 and 2 for consolidated sandstone, and mentioned it can be as low as 1.3 for clean unconsolidated sands. I am specifically interested in testing if formation factor contributes significantly to a statistical model of permeability, because here the formation factor computation is tuned to take into account the scaled sub-resolution porosity data in the intermediate gray scale voxels. For this reason, especially in the case of low-resolution images, the result from the formation factor computation is not necessarily a reliable measure of electrical conductivity. Instead it is an arbitrary characteristic chosen for possible correlation with petrophysical properties, particularly absolute permeability, because it represents current flow through voxel space where resistance to flow at each voxel is determined by the fraction of pore space and intermediate clay phase in that voxel. To test the sensitivity of the correlation between formation factor and permeability to variations in the $m$ exponent I generate formation factor data for

$m = 2$, 2.5, and 4. I select 2 because it is the classically accepted value for consolidated sands, while 2.5 and 4 are considered because they may help to capture the fact that flow velocity is highly sensitive to obstructions.

### 4.6.4 Minkowski Functionals

The so-called Minkowski Functionals are a set of additive morphological measures representing, for three-dimensional objects, volume (Open Pore Fraction - OPF), surface area (SA), mean curvature (MC), and the Euler characteristic (EC) (C. H. Arns et al., 2001; Mecke, 1996; Schladitz et al., 2006). The volume measurement is equal to the open pore fraction explained in section 4.6.2. Here I generate data for the Minkowski Functionals using the morphological analysis algorithm implemented by *Arns et al.* [2001b], which includes the computation of the critical length (lc).

## 4.7 Statistical Modelling

### 4.7.1 Choosing a Statistical Approach

Section 3.2 (Multi-scale Imaging) explains that a common approach to dealing with heterogeneous core samples is to perform a classification of the range of heterogeneity and to physically collect high-resolution data on a single or multiple portions of the sample that represent the range of classes. Initial visual inspection of the LR and IR images of the 25mm core plug of sample 1 revealed what appeared to be several repeating ‘units’ or ‘lamellae’. It was therefore tempting to consider a classification-based approach. Since that is a fairly common technique my hope was that the data would not require a user-defined classification, but that it would naturally cluster based on some characteristic such as grain size, porosity, mineral fractions, etc. The first step to investigate this possibility was to develop the unitisation procedure described in section 4.3. The next step was the computation of the range of rock characteristics described in section 4.4. A scatter plot of grain size for the HR 5 µm/voxel 8mm image against grain size for the IR 16 µm/voxel data from the overlap region in the 25mm image showed that the three units identified by the unitisation procedure form three distinct clusters (figure 4.7a). However, a scatter plot of pore size (figure 4.7b) shows less evidence of clustering and indicates that each unit has sufficient internal variability to obscure the presence of three distinct units. Each data point represents an approximately cubic sub-volume from one of the units. The x,y,z voxel dimensions of the sub-volumes for sample 1 are: unit 1 = (330, 330, 330), unit 2 = (330, 330, 392), and unit 3 = (425, 425, 425). It is also interesting to note that pore size should have more influence over permeability, as it is a measure of pore length scale. It would therefore be reasonable to deduce that permeability would likely show similar intra-unit variability.

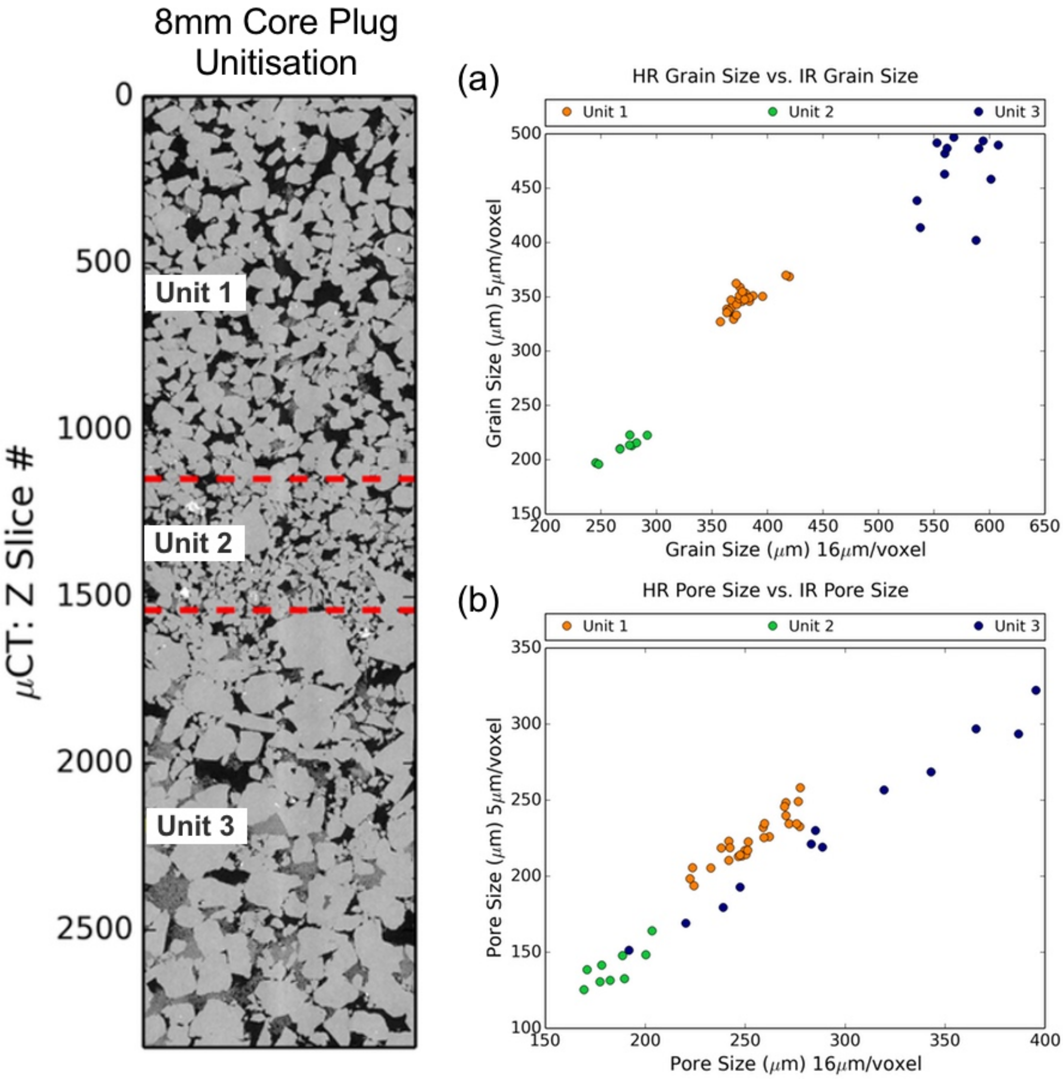

Figure 4.7: Plotting median grain size (a) and median pore size (b) from the HR 5 μm/voxel image of the 8mm sub-plug and the region of overlap in the IR 16 μm/voxel image of the 25mm core plug.

Figure 4.8 shows the grain size plotted against the pore size from the IR 16 μm/voxel image of the 25mm core plug in addition to the unitisation of the 25mm core plug image as a guide to the diagrams. Notably there is no distinct clustering of the grain and pore size data; instead, the data is spread across the range of observed grain and pore sizes. Figure 4.8 shows that there is a more distinguishable spread of the data with units 9, 10, 11, and 12 separating slightly from the rest of the units at the higher end of the grain size scale. The distinction is however not clear and there is no well-defined natural clustering similar to that of the grain size from the HR 5 μm/voxel image of the overlap regions (figure 4.7).

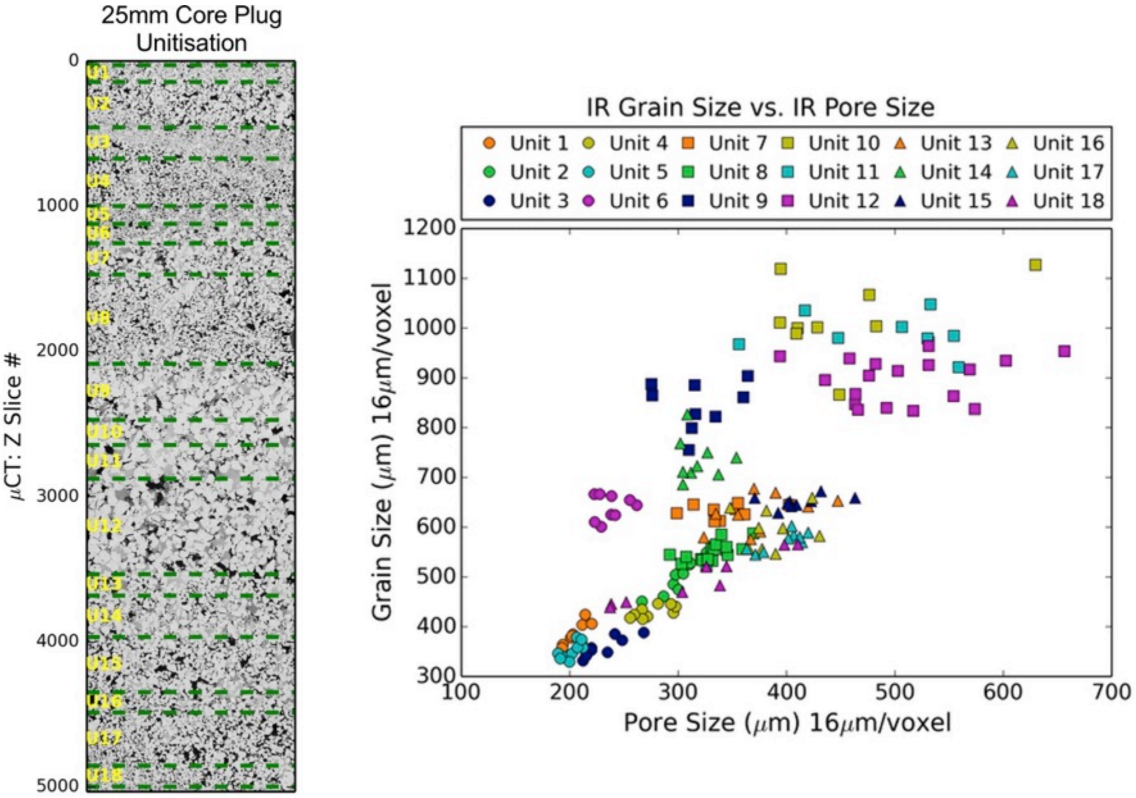

Figure 4.8: Plotting grain size versus pore size of the IR 16 μm/voxel image of the 25mm core plug. The data shows little evidence of natural clustering; instead, it shows a spread of data points along the range of grain and pore size values.

Braided river systems are complex depositional environments and include a range of geological components including rapidly shifting channels of variable width, sand bars that are characterised by elevated areas, which are generally only active during times of flooding (Miall, 1977). In combination with fluctuations of variables such as discharge, sediment load, stream velocity, and slope, (Leopold & Wolman, 1957) braided river deposits like the Precipice sandstone typically show considerable internal variability with large ranges of values for characteristics such as grain size and sorting, pore size, porosity, and mineral content. It is therefore unlikely that even a highly rhythmic depositional environment would produce lamellae with clear natural clustering based on grain and pore size. The data in figure 4.8 suggest that the natural product of the braided river system responsible for the deposition of this section of rock appears to be a set of lamellae that covers the entire range of grain and pore sizes. A small sample may capture a limited number of lamellae that form well-defined clusters such as those in figure 4.7; however, as the number of lamellae increases the spaces between the clusters are gradually filled with more data points, thereby creating a population of lamellae that exist as a continuum over a range of values. A simple classification system such as one based on the Udden-Wentworth grain size scale (Udden, 1914; Wentworth, 1922) will likely result in sub-volumes from the same unit being classified in different size classes because of intra-unit variability. It follows that the assumption that each sub-volume in each group has the same flow properties would result in potential high-frequency fluctuations of flow properties within a single unit. The results presented in this section suggest that a linear regression approach is more appropriate and is more likely to capture subtle variability in flow properties both within and across the units.

One cannot consider a statistical approach for the question of flow property predictions without also considering the use of machine learning algorithms. Machine learning, often referred to as neural networks, might be considered a sub-domain of artificial intelligence where an algorithm modifies the outcome of an analysis if it is introduced to more examples of how it is expected to behave. It makes use of the principal of training the algorithm using an example dataset with known input and output values and then applying the trained algorithm to unknown data to perform predictions. Dividing a dataset with known input and output values into training and testing subsets helps assess and validate the prediction accuracy. Machine learning is increasingly being used in predicting petrophysical properties in reservoir and aquifer systems. *Chen and Lin* [2006] use a committee machine, which is a type of neural network that combines the tasks of two or more “experts” to achieve a desired result. In this instance Chen and Lin incorporate three known empirical formulas into their committee machine to derive permeability from downhole logging data. They divide 82 datasets comprising well logging and core data in half to train and test their algorithm and conclude that the neural network that combines the three empirical formulas perform better than any one formula individually. In a similar approach *Karimpouli et al.* [2010] predict permeability from ten input parameters using well logging data that intersect various lithologies including limestone, dolomite, sandstone, and shale. Critically they perform a basic characterisation analysis to divide their datasets into low- and high-permeability groups to limit the output range over which the neural network needs to function at any given time. Using support vector machines (SVM) and the structural risk minimisation (SRM) principal, rather than neural networks that rely on the empirical risk minimisation (ERM) principal, *Al-Anazi and Gates* [2010] predict electrofacies and permeability distributions in a heterogeneous sandstone reservoir. Generally machine learning methods are good for prediction applications and have transformed image classification and speech recognition since 2013. However, in this study I am not only interested in predicting petrophysical properties, but also understanding how the predictor characteristics change with changes in image resolution, and which characteristics carry the most useful information for petrophysical predictions. Since machine learning methods are often opaque in their operation their use is beyond the scope of this thesis.

### 4.7.2 Statistical Methods

The workflow to predict petrophysical properties involves two stages of statistical calibration based on the 8mm sub-plug region in the HR, IR, and LR images. The first stage is the correlation between individual predictor character characteristics from the LR and IR images with numerically computed petrophysical properties from the HR image using ordinary least squares (OLS) linear regression. The statistical correlations are developed using response and predictor data from exactly the same physical rock volumes represented by different resolution images (see section 4.6). In OLS the coefficient of determination ($R^2$) is a measure of how much variance in the response variable can be explained by the predictor characteristics. $R^2$ is the difference between 1 and the ratio of the total sum of squares ($SS_{res}$) and the residual sum of squares ($SS_{tot}$) (eq. 4.2).

$$R^2 = 1 - \frac{SS_{res}}{SS_{tot}} \tag{4.2}$$

$SS_{res}$is equal to the sum of the squares of the difference between the observed values ($y$) and the predicted values ($x$) of the model (eq 4.3). $SS_{tot}$is equal to the sum of the squares of the difference between the observed values ($y$) and the mean of the observed values ($\bar{y}$) for the response variable (eq 4.4).

$$SS_{res} = \sum_{i=1}^{n} (y_i - x_i)^2 \tag{4.3}$$

$$SS_{tot} = \sum_{i=1}^{n} (y_i - \bar{y})^2 \tag{4.4}$$

$R^2$ ranges between 0 (no correlation between the predictors and the response variable) and 1 (the predictor characteristics perfectly describe the variability in the response variable). Based on 48 data points from sample 1 for each characteristic, we use $R^2$ as a measure of the predictive capability of individual rock characteristics, and to assess their relative contribution to predicting permeability in multiple linear models combining a subset of characteristics. Additionally, the F-statistic, expressed as a probability value (p-value), gives an indication if a model of the response variable is significantly different from a regression model with no predictor variables (intercept model).

In developing the statistical models used for permeability prediction I first assess the predictive ability of each individual characteristic. The next step is to consider if some combination of variables in a multiple linear model provides a more complete description of the permeability variations. As is generally accepted in regression analysis when considering multiple predictors with a range of values in different units, I standardize each predictor by subtracting the mean and normalizing to its standard deviation (Marquardt, 1980). Critically I must consider which characteristics to include in such a multiple model. One method is to assess each single variable model and decide, based on $R^2$, the model p-value, and an understanding of the physical meaning of each characteristic, which combination of predictors are most likely to define a reliable model. Because I am specifically interested in the ability of the formation factor characteristic to predict absolute permeability, this is the method I use to develop its multiple linear model. Another purely statistical approach of model selection is that of stepwise regression, which can either be performed as forward selection or backward elimination of variables (Hocking, 1976).

Forward selection starts by selecting the individual characteristic that describes the most variance in the response variable or has the lowest individual p-value. In a stepwise manner one starts to add additional variables. If the additional variable does not contribute significantly to the model (according to the variable's p-value) it is discarded and the next variable is tested. A variable is deemed significant if its p-value is smaller than some arbitrarily selected alpha threshold. In his study I select the 95% significance threshold, therefore the alpha value is 0.05, which indicates that any variable with a p-value greater than 0.05 has less than 5% probability of influencing the predictive capacity of the model. In other words the model is unlikely to be any different if that variable were omitted. Backwards elimination starts with all the characteristics in a multiple linear model. The variable with the largest p-value greater than 0.05, is removed from the model and the remaining characteristics are used for a subsequent model. At the end of the process one is left with a set of variables, each of which contributes significantly to the model (with p-values lower than 0.05). In the case of the capillary pressure parameters I make use of backwards elimination for model development.

Alternatively one could use a multivariate analysis technique such as principal component analysis (PCA) to help with model development and selection. I perform a PCA on standardized variables since it aims to identify directions of maximum variance (Jackson, 2005). The results include eigenvalues - the amount of variance - and eigenvectors - the principal components defining the direction of maximum variance. PCA of $n$ variables produces $n$ principal components, with each principal component a linear combination of the original variables (Jolliffe, 2014). The 'loadings' between each principal component and the original variables are computed using eq. 4.5.

$$r_{ij} = \frac{u_{ij}\sqrt{l_i}}{s_j} \tag{4.5}$$

in which $r$ is the correlation between the i$^{th}$ principal component and the j$^{th}$ original variable, $u$ is the eigenvector coefficient, $l$ is the eigenvalue, and $s$ is the variance of the original variable, which is 1 for standardized data. The loadings indicate how well each principal component is aligned with the original variables, i.e. how much information from each variable is reflected in each principle component (Abdi & Williams, 2010) (Please note that the popular statistics software package 'R' refers to eigenvectors as 'loadings', which is distinct from the definition used here). The loadings between the principal components and the original variables may reveal which original characteristics are best suited to construct a predictive multiple OLS model. Furthermore, the principal components can be used as new predictor variables of the response variable in a principal component regression; however, in this instance I choose not to make use of this regression method for statistical calibration, because the principal components cannot be interpreted directly in terms of their physical meaning.

# 5 Image Resolution Effects

In this chapter I take a closer look at the impact of changing image resolution on the computation of permeability and a range of rock characteristics, including grain and pore size, grain and pore sorting, porosity, the fraction of clay phase, and the set of Minkowski Functionals. The comparison of petrophysical properties and rock characteristics data from the sub-volumes (see section 4.6) are based on exactly the same physical rock volumes in each of the HR, IR, and LR images. The x,y,z voxel dimensions for the comparison sub-volumes from the HR image of the 8mm overlap region are: Unit 1 = (330, 330, 330), Unit 2 = (330, 330, 392), and Unit 3 = (425, 425, 425).

## 5.1 Permeability and Image Resolution

Whenever possible, one would determine permeability directly; indirect methods are required only when direct computation is impossible. The main objective of this section is to demonstrate that conventional methods of estimating permeability, such as Lattice-Boltzmann based simulations and Katz-Thompson calculations, fail when there is not sufficient resolution in the image to accurately represent the pore space. Figure 5.1a shows how the loss of geometric information impacts computed permeability using the Lattice-Boltzmann method. The 16 μm/voxel image yields unreliable results, returning zero or underestimating the permeability compared to the 5 μm/voxel data for values lower than ~2000 mD. From a geometric standpoint the Lattice-Boltzmann method requires 4 voxels across a connecting pore throat to return some permeability data. Two voxels define the boundary voxels where there are no-flow boundary conditions, and at least 1, but preferably 2 voxels, are required within the pore channel to allow fluid flow during the simulation. It follows that in this example, for those volumes returning zero or underestimated permeability values, the pore throats governing fluid flow are smaller than 48 μm (3 x 16 μm), which the 16 μm/voxel image is unable to capture, but larger than 15 μm (3 x 5 μm), which the 5 μm/voxel image is able to capture.

Figure 5.1b shows the good correlation between permeability computed using the Lattice-Boltzmann method and the Katz-Thompson equation for the 5 μm/voxel image. The resolution is sufficient to accurately represent the largest connecting pore throats and to allow reasonable estimates of the pore system critical length, and therefore its permeability using the Katz-Thompson method (eq 3.8 and, for convenience, eq 5.1).

$$k = Cl_c^2\left(\frac{\sigma}{\sigma_0}\right) = Cl_c^2\frac{1}{F} = Cl_c^2\tau \tag{5.1}$$

Note that to achieve the correlation in figure 5.1b the universal constant ($C$) in eq. 5.1, reported as on the order of $\frac{1}{226}$ by Katz and Thompson, was modified to $\frac{1}{21}$. The value for the universal constant was determined by modulating it until the best correlation was found. In their paper Katz and Thompson highlight that the constant value of $\frac{1}{226}$ is a function of choice of the critical length ($l_c$) from a capillary pressure curve, which is typically accurate to 15% of the true value. Specifically they point out that a chosen length value in the region of the actual $l_c$ would change the value of the universal constant. With µCT images the computed $l_c$ is directly related to the image resolution; therefore, it could be argued that the constant is effectively an additional scaling parameter to correct for scaling not taken into account by the computed length. Computing the $R^2$ statistic for the 1:1 line in figure 5.1b (an indication of how closely the data points fall on the line passing through zero with a 45° angle) yields a value of 0.86, indicating the Lattice Boltzmann and Katz-Thompson computations match one-another closely. Figure 5.1c shows the permeability using the Lattice-Boltzmann method for the 5 µm/voxel image against the permeability computed using Katz-Thompson and the 16 µm/voxel image. In this instance the universal constant was set to $\frac{1}{15}$. Note how the Katz-Thompson results for the 16 µm/voxel image returns zero permeability for several volumes. The lower image resolution is not sufficient to capture the permeability-controlling flow pathways, leading to zero critical length values and zero computed permeability. It follows that for the 16 and 64 µm/voxel images of these samples both the Lattice-Boltzmann and Katz-Thompson methods cannot produce reliable results and we need an alternative method of determining permeability.

The work by Katz and Thompson provides an opportunity to develop a basic workflow to estimate the minimum image resolution required to accurately capture the pore system geometry to allow fluid-flow simulation. Mercury injection porosimetry delivers the critical threshold pressure, which can be converted to a critical pore diameter using the Lucas-Washburn equation (Washburn, 1921). With the Lattice-Boltzmann method one requires four voxels across a pore throat for fluid flow simulation. The outer two voxels are no-flow voxels, while the inner two voxels allow fluid flow. It follows that one could simply divide the critical pore diameter (computed from MIP) by 4 to estimate the required minimum voxel dimensions.

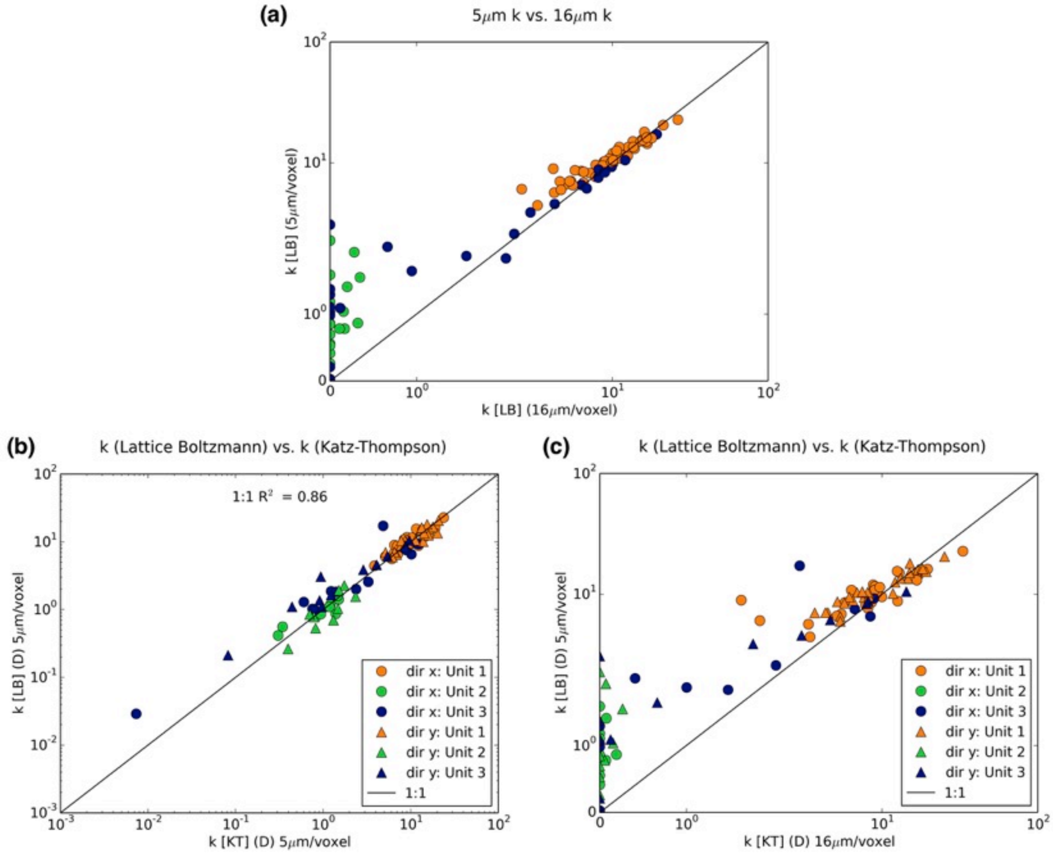

Figure 5.1: Using Katz-Thompson computed permeability to demonstrate why permeability simulations using the Lattice-Boltzmann method fail for lower resolution images. Simulated permeability using the Lattice-Boltzmann method for the 5 and 16 μm/voxel images shows that the computation fails in the lower resolution image (a). There is good agreement between computed permeability in the 5 μm/voxel image using the Lattice-Boltzmann and Katz-Thompson methods (b); however, plotting permeability from the Lattice-Boltzmann method for the 5 μm/voxel image against Katz-Thompson permeability computed from the 16 μm/voxel image shows how several computation volumes in the 16 μm/voxel image have zero critical length, and therefore, zero computed permeability (c). Plotted with the 'Matplotlib' python library with axis types set as 'symlog' (http://matplotlib.org/api/pyplot_api.html#matplotlib.pyplot.xscale), which provides logarithmic scales that include a small linear scale around zero, allowing zero to be plotted.

## 5.2 Rock Characteristics and Image Resolution

Before performing any statistical analyses let us first investigate the impact of image resolution on the computation of the various rock characteristics indented for use as predictor variables of the petrophysical properties. All data comparisons are performed on the region of overlap between the 8mm sub-plug and the intermediate- and low-resolution images of the 25mm core plug. Figure 5.2 demonstrates the relationship between grain size computed from the HR and IR images and between the HR and LR images (a and b respectively). Figure 5.2c and d show the same comparison for the pore size characteristic. Both the IR and LR images produce larger grain size and pore size values than the HR image because the superior voxel resolution HR image naturally captures more information on smaller features in the rock. Additionally, as the image resolution decreases the boundaries between adjacent grains are less easily distinguished by the watershed operation resulting in merged grains, which are treated as single larger grains in the computation. The resulting grain and pore size distribution curves for the HR image carry more information for smaller grains and pores, thereby producing smaller median grain and pore size values. It is also interesting to note that the degree to which the grain size values of individual units change when comparing the IR and LR images is not the same. Compared to units 1 and 3 the grain size characteristic changes more rapidly in unit 2 (green data points), which has the finest grain and pore textures of the three units. Pore size shows a more uniform rate of change. This indicates that the merger of phases with decreasing resolution is more significant for grain size, whereas decreasing resolution causes larger pores to be isolated from one another, thereby resulting in a more consistent rate of change from one unit to the next.

Apart from the fact that pore size is a geometric measurement and that fluid flow properties have been shown to depend on pore geometry, the fact that pore size changes at a more consistent rate across the units from one image resolution to the next might be an indication that it could be a useful predictor of geometry-dependent flow properties in low-resolution images.

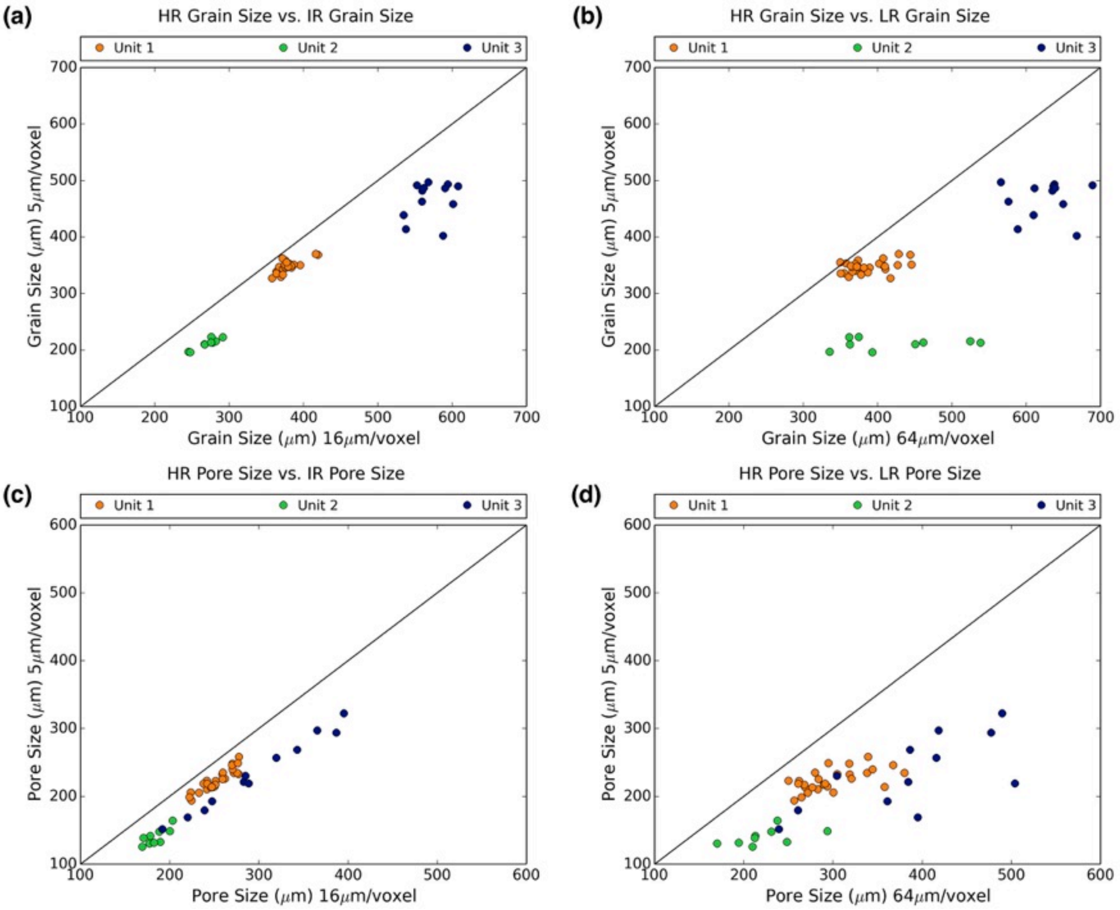

Figure 5.2: Comparing the grain size characteristic computed from the HR image of the 8mm sub-plug with the IR and LR images (a and b), and the pore size characteristic from the HR image with the IR and LR images (c and d) of the overlap regions from the 25mm core plug. The black diagonal lines show the 1:1 relationship on each diagram.

The grain and pore size distributions for each sub-volume in the 8mm overlap regions were expressed as sorting values (see section 4.6.1). Small sorting values indicate well-sorted grains or pores, and large sorting values indicate poorly sorted grains and pores. Figure 5.3 shows the changes associated with the grain and pore sorting data from the HR to the IR and LR images. The grain sorting characteristic has a surprisingly linear trend between the 5 μm/voxel HR image and the 16 μm/voxel IR image; however, the IR image produces slightly lower sorting values compared to the HR image (figure 5.3a). This is attributed to a smoothing effect where the boundaries between grains are less easily distinguished because of the decreased image resolution. It is interesting to note that the grain sorting from all three units appear to be affected to a similar degree from the HR to the IR image. The linearity of the relationship between HR and IR grain sorting indicates that the

IR 16 µm/voxel image contains some geometric information, which may be useful for predicting permeability. Figure 5.3b shows the changes in grain sorting compared between the HR and LR images. The change is much more dramatic and there is no relationship between the HR and LR image grain sorting data.

A comparison between the pore sorting of the HR and IR images (figure 5.3c), and between the HR and LR images (figure 5.3d) indicates similar behaviour compared to that of grain sorting; however the HR and IR pore sorting data do not show a particularly strong linear relationship. In both the 16 µm/voxel IR and 64 µm/voxel LR images pore sorting is underestimated compared to the 5 µm/voxel HR data. The pore network has a much smaller length scale than the grain component of the rock, for this reason the lower image resolution has a more significant impact on the pore sorting computation. With a decrease in image resolution smaller pores are effectively removed from the leaving behind the larger more similar size pores, which results in lower sorting values.

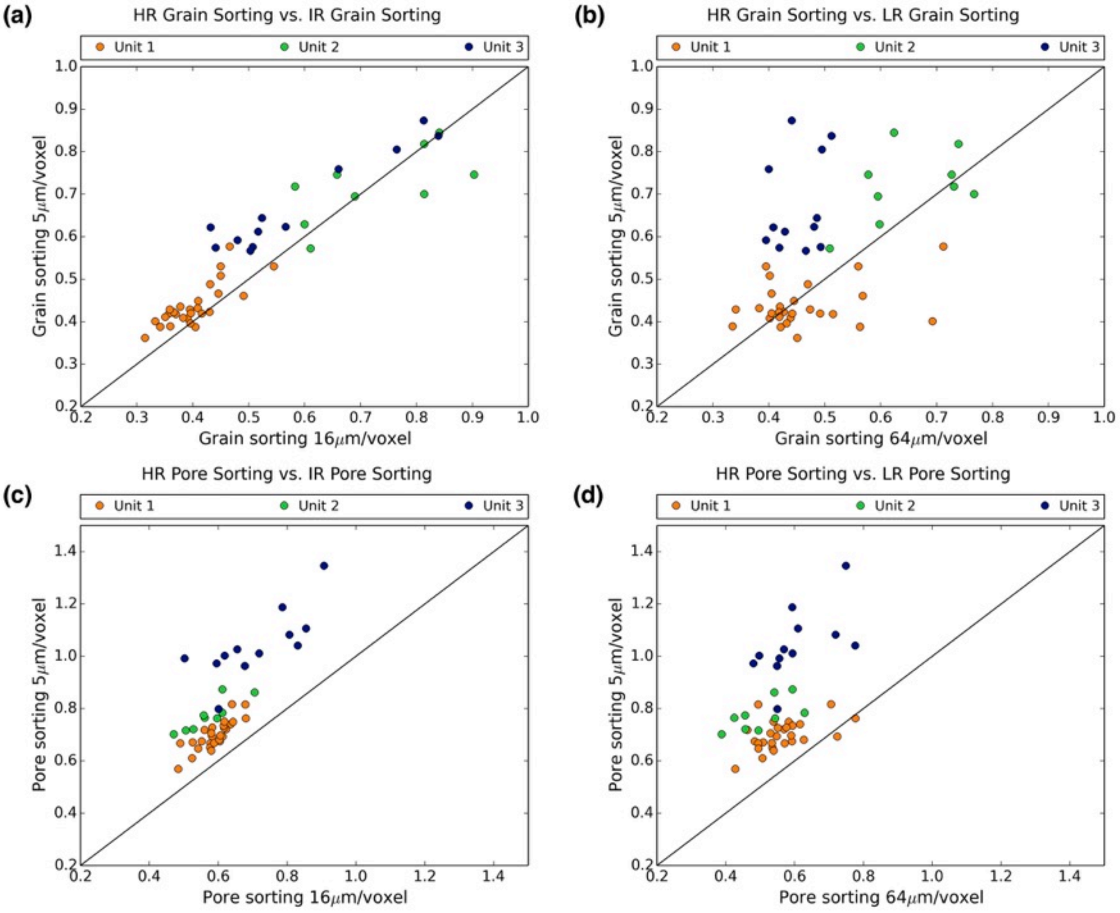

Figure 5.3: Comparing the grain sorting characteristic computed from the HR image of the 8mm sub-plug with the IR and LR images (a and b), and the pore sorting

characteristic from the HR image with the IR and LR images (c and d) of the overlap regions from the 25mm core plug. The black diagonal lines show the 1:1 relationship on each diagram.

The changes associated with porosity and clay fraction reflect the impact of the increasing proportion of voxels with intermediate gray scale values. Porosity and clay fraction are computed by taking into account sub-resolution porosity from the soft-segmentation data (see section 4.6.2). The resolution change from 5 μm/voxel in the HR image to 16 μm/voxel in the IR image of the overlap region is not large enough to have a significant impact on the porosity and clay fraction characteristics (figure 5.4a and c). The 64 μm/voxel LR image contains a considerable proportion of intermediate gray scale voxels, which increases the porosity and clay fraction values computed from the LR overlap image relative to those of the HR image (figure 5.4b and d). Based on these data it is possible that porosity may contribute to predictions of absolute permeability because it takes into account image gray scales, which includes connecting pore throats. However, the porosity characteristic cannot distinguish between connected and non-connected pores, and, in the LR image, even those pores that do not contribute significantly to fluid flow may be represented as intermediate gray scale voxels. For this reason porosity may not correlate with permeability.

A similar characteristic to porosity is the resolved pore spaces, here referred to as the Open Pore Fraction, which does not include sub-resolution porosity, but rather those voxels that are clearly defined as pore space in the segmentation process. Open pore fraction represents the first of the Minkowski functionals. Figure 5.5a demonstrates that there is a remarkably linear relationship between the open pore fraction computed from the HR and IR images. As expected the IR 16 μm/voxel image resolves fewer open pore spaces because of the reduced resolution and therefore produces a lower open pore fraction relative to the HR image. Unit 2 (the green data points) shows the most significant deviation from the 1:1 line. Being the finest-grained unit in the overlap region with the smallest pores it is expected that its open pore fraction would be most affected by changes in image resolution. A comparison between the HR image and the 64 μm/voxel LR image shows that the reduction in resolution is large enough to significantly impact the open pore fraction of all three units (figure 5.5b). As for the IR image the fine-grained unit 2 experiences the most dramatic shift, followed by units 1 and 3, which respectively contain medium and large size grains and pores.

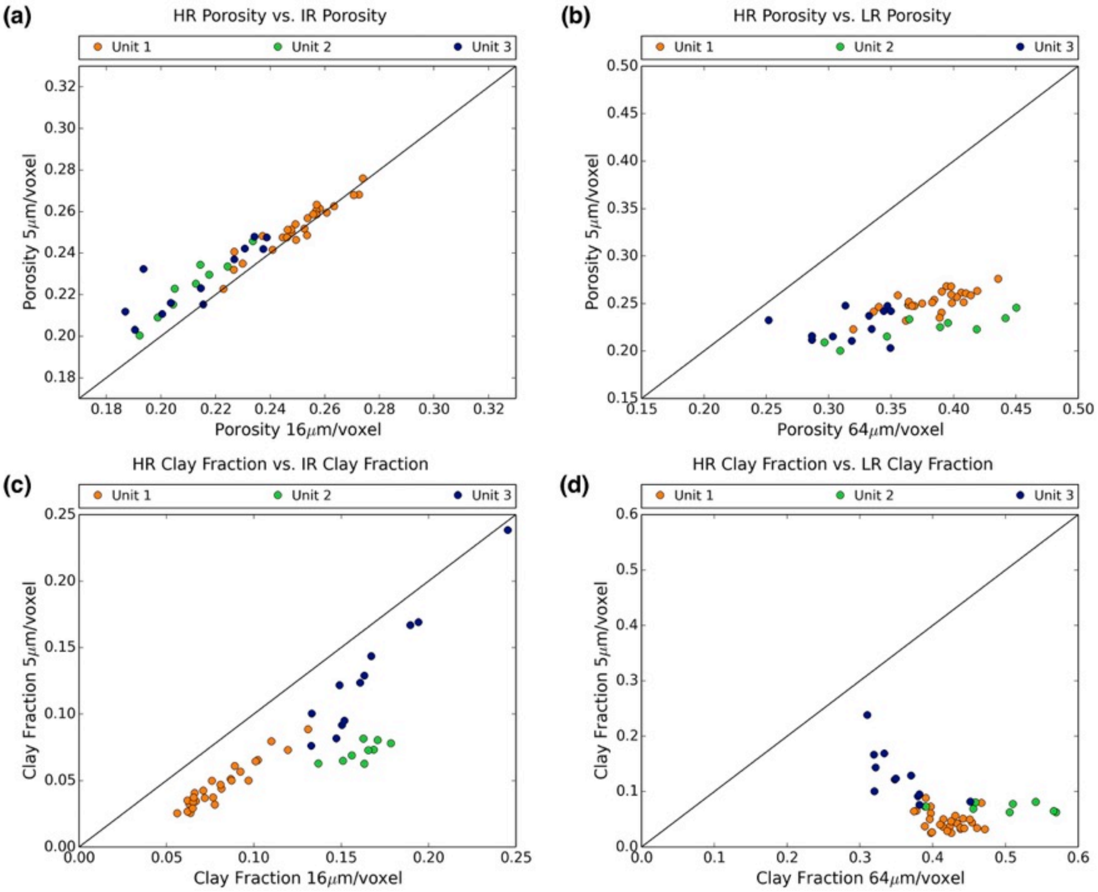

Figure 5.4: Comparing the porosity characteristic computed from the HR image of the 8mm sub-plug with the IR and LR images (a and b), and the clay fraction characteristic from the HR image with the IR and LR images (c and d) of the overlap regions from the 25mm core plug. The black diagonal lines show the 1:1 relationship on each diagram.

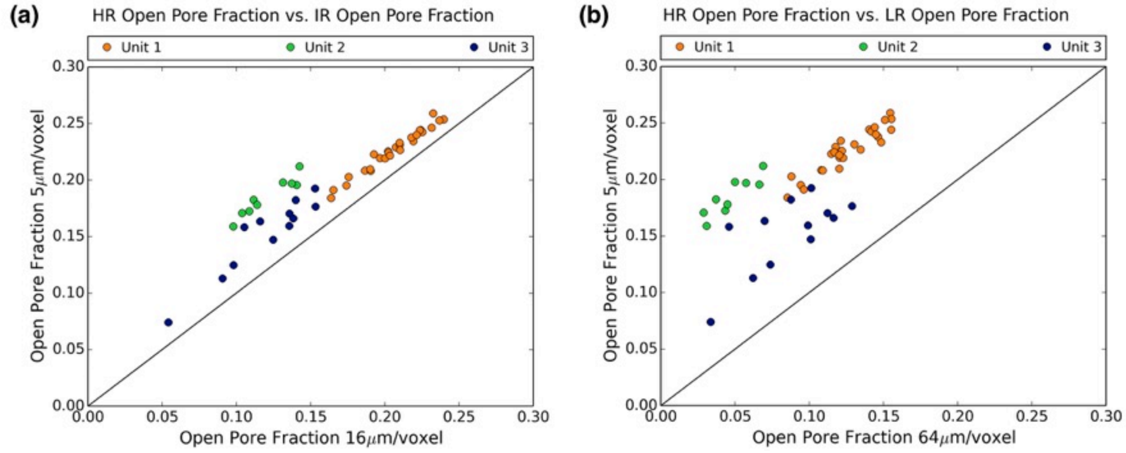

Figure 5.5: Comparing the open pore fraction characteristic computed from the HR image of the 8mm sub-plug with the IR and LR images (a and b) of the overlap regions from the 25mm core plug. The black diagonal lines show the 1:1 relationship on each diagram.

Figure 5.6 shows the comparison between the remaining Minkowski functionals, i.e. surface area (a and b), mean curvature (c and d), and the Euler characteristic (e and f), computed for the overlap regions of the HR 5 µm/voxel, IR 16 µm/voxel, and LR 64 µm/voxel images. Here the Minkowski functionals are measured in the pore space and reported in standardised real units (not voxel units). The change in image resolution has a significant effect on these characteristics and for all three of them there is no clear relationship between the computed values from various resolutions. For all three Minkowski functionals the distribution of the data points remain relatively consistent in the image pairs; however, the scale of the computed values change significantly in the IR and LR images. The only notable change in the distribution of the data points is the relative positioning of those sub-volumes from unit 3, which, for the surface area (a and b) and mean curvature (c and d), are located slightly to the right on the x-axis for the LR 64 µm/voxel images (figures 5.5b and d) compared to IR 16 µm/voxel images (figures 5.6a and c). This may be expected since surface area and surface curvature are likely to be highly resolution dependent for rough surfaces. In both cases the changes for the sub-volumes from unit 3 are in the same order of magnitude as units 1 and 2. Unit 3 has the largest grains and pores, therefore, it is expected that as the image resolution decreases the surface area would decrease at a slightly lower rate, while the mean curvature increases at a slightly faster rate.

*Vogel* [2008] explains that the Euler number ($\chi$) can be computed by combining the basic topological measures i.e.: the number of isolated objects ($N$), the number of redundant connections in the pore space ($C$), and the number of enclosed cavities ($H$) as shown in eq. 5.2. It follows that the Euler number is an indication of pore connectivity; with positive and negative values typically indicating poorly connected ($N > C$) and well connected ($N < C$) structures respectively. It can be argued that $H$ is inconsequential for most porous rocks since the occurrence of isolated grains within a pore space is not common.

$$\chi = N - C + H \tag{5.2}$$

The data in figure 5.6e indicate that unit 1 in the IR 16 µm/voxel image, with intermediate grain and pore size relative to units 2 and 3, generally has a better connected pore system compared to those of unit 2 (the finest grained) and unit 3 (the coarsest grained but least well sorted). At the lowest resolution of the 64 µm/voxel (figure 5.6f) most of the sub-volumes have positive Euler numbers showing poor connectivity in all three units, even though the relative positioning of the units along the x-axis remains fairly consistent.

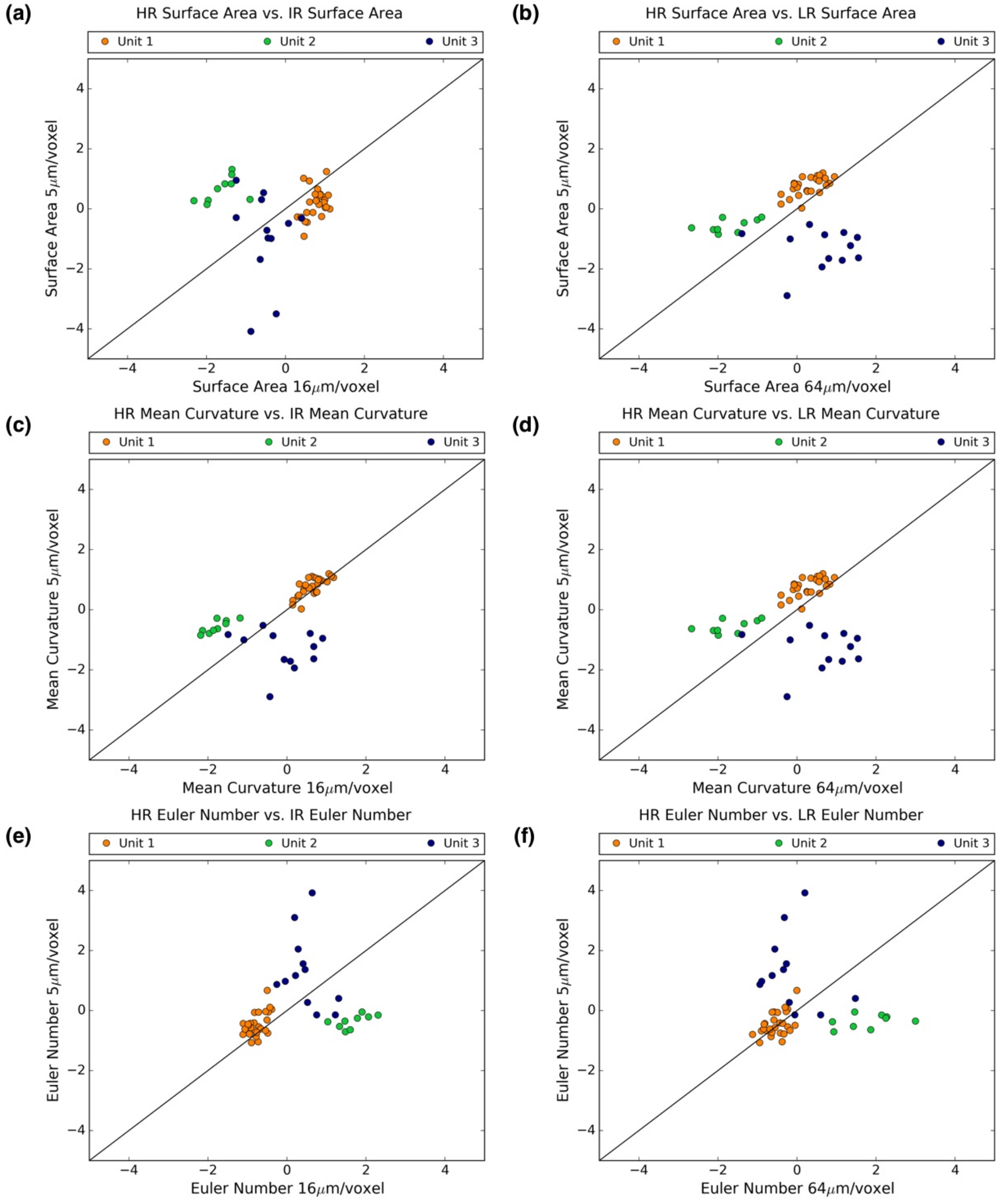
(a) HR Surface Area vs. IR Surface Area

(b) HR Surface Area vs. LR Surface Area

(c) HR Mean Curvature vs. IR Mean Curvature

(d) HR Mean Curvature vs. LR Mean Curvature

(e) HR Euler Number vs. IR Euler Number

(f) HR Euler Number vs. LR Euler Number

Figure 5.6: Comparing the surface area (a and b), mean curvature (c and d), and Euler number (e and f) Minkowski functionals computed from the HR image of the 8mm sub-plug with the IR and LR images of the overlap regions from the 25mm core plug. The changes in the characteristics are too large to plot a practical 1:1 line.

# 6 Permeability Results and Discussion: Sample 1

In this chapter I compile and discuss the results of the statistical correlations between permeability and predictor rock characteristics. The chapter starts with a look at the commonly used porosity-permeability plot, which is followed by an explanation of the development of the single and multiple linear statistical models from the overlap regions in the HR, IR, and LR images. The chapter concludes with the application of the chosen statistical models to estimate absolute permeability in the 25mm 16 and 64 µm/voxel images of the sample 1 core plug. The statistical correlations are developed using response and predictor data from exactly the same physical rock sub-volumes represented by different resolution images.

The x,y,z voxel dimensions for the sub-volumes used to develop statistical correlations in the high-resolution image of the 8mm overlap region are:
Unit 1 = (330, 330, 330),
Unit 2 = (330, 330, 392), and
Unit 3 = (425, 425, 425).

## 6.1 Porosity-Permeability

In his review paper *Nelson* [1994] highlights the use of porosity-permeability relationships to assist in the determination of permeability from well logs and core samples. He references the work of several authors demonstrating the often linear relationship between porosity and permeability. *Beard and Weyl* [1973] investigate artificially mixed unconsolidated sand packs with a range of grain sizes and sorting. Their results are extremely informative and demonstrate how, for each grains size class, the permeability increases with increases in porosity as a function of changes in sorting from poorly to well sorted. Permeability also increases as the average grain size increases. Their results contain subtle information regarding the relationship between porosity, grain size, grain packing, and permeability. Sand packs containing well-sorted grains are grain size independent (as for uniforms spheres) and porosity decreases slightly as grains become less well sorted while the permeability increases with increasing grain size. Beard and Weyl's results demonstrate the complexity of flow through porous rocks and the range of parameters impacting on permeability.

Figure 6.1 shows the general linear relationship between the logarithm of the permeability and porosity in the HR 5 µm/voxel image of sample 1. An interesting observation is the large spread of data points with little evidence for clustering on either axis, thereby providing further support for a statistical approach over a classification-based methodology. Furthermore, from simple visual observation there is a considerable range of permeabilities for any given porosity. In particular the finer unit 2 is a factor of 10 lower in $k$ for the same porosity. As demonstrated by the work of *Katz and Thompson* [1986] the porosity measure is not capable of capturing the length scale in which fluid flow must occur, and, even though these data were collected from consolidated material, in the context of the results of *Beard and Weyl* [1973] porosity is but part of the story.

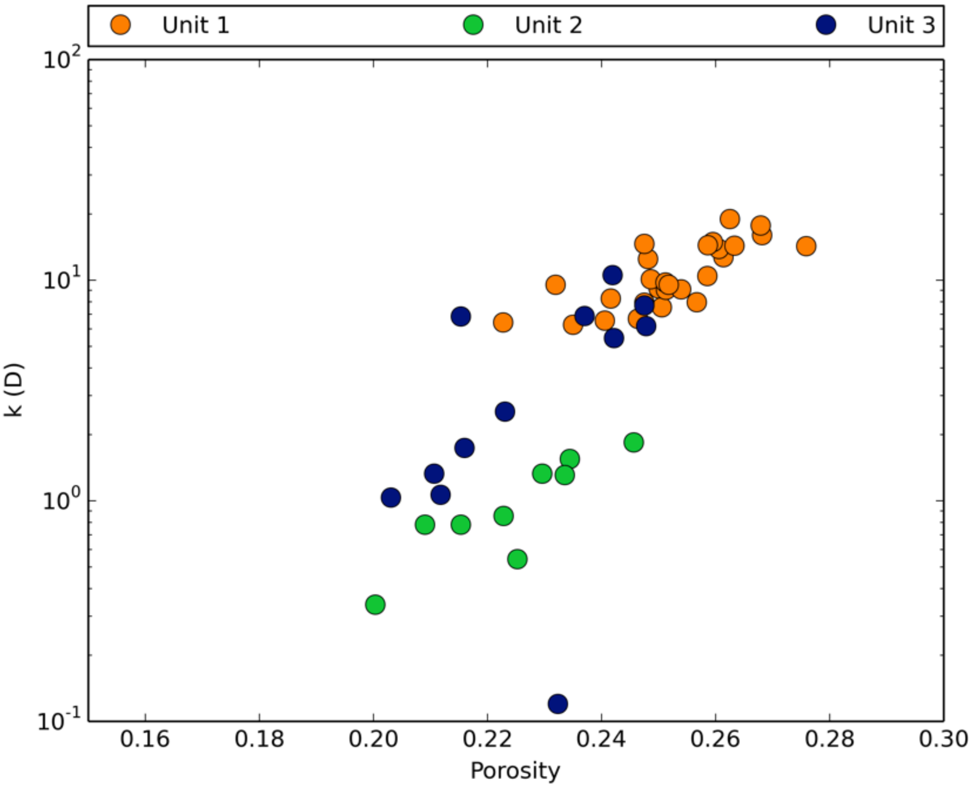

Figure 6.1: A porosity-permeability plot for the HR 5 μm/voxel image of the overlap region of sample 1. The graph shows a roughly linear relationship and the nearly continuous spread of the data points.

## 6.2 Statistical Calibration: Individual Characteristics

As a first step I compile ordinary least squares (OLS) models between the logarithm of each characteristic and the logarithm of permeability. The second stage of statistical calibration combines some subset of the individual characteristics into multiple linear models (section 4.5.2) to provide a more complete statistical description of permeability. One method of identifying predictor variables for a multiple OLS linear model is a principal component analysis. The results from the PCA (table 6.1) show that the first three principal components explain 90% of the variance in the predictor characteristics for both the 16 and 64μm/voxel images. For the 16 μm/voxel data the first two principal components, PC1 and PC2, correlate well with permeability based on their $R^2$ values. The loadings for the 16 μm/voxel data indicate that PC1 shares considerable information with open pore fraction, porosity, formation factor, grain sorting, clay fraction, and mean curvature, while PC2 shares information with pore and grain size and pore sorting. For the 64 μm/voxel image PC1 correlates best with permeability. The loadings of PC1 show a similar trend compared to that of 16 μm/voxel image, but with the addition of the Euler characteristic, which also shares considerable information with the first principal component.

Table 6.1: Principal component analysis results for the 16 and 64 μm/voxel data showing the coefficient of determination ($R^2$) between the first three principal components and permeability, the fraction of variance explained by the components, and the loadings (correlations) of the components onto the original variables.

| | **$R^2$ w. Perm.** | **Variance Fraction** | **OPF** | **P** | **PS** | **F** | **GS** | **Gsort** | **Psort** | **CF** | **SA** | **MC** | **EC** |
|---|---|---|---|---|---|---|---|---|---|---|---|---|---|
| 16 μm/voxel Image | | | | | | | | | | | | | |
| **PC1** | 0.8 | 0.6 | -0.9 | -0.9 | -0.5 | 0.8 | 0.0 | 0.9 | 0.1 | 0.9 | -1.0 | -0.9 | 1.0 |
| **PC2** | 0.7 | 0.2 | 0.3 | 0.1 | -0.8 | 0.2 | -0.9 | 0.0 | -0.8 | -0.4 | 0.0 | -0.3 | 0.0 |
| **PC3** | 0.3 | 0.1 | 0.3 | 0.3 | -0.1 | -0.3 | -0.3 | 0.3 | 0.6 | 0.1 | -0.1 | -0.2 | 0.1 |
| 64 μm/voxel Image | | | | | | | | | | | | | |
| **PC1** | 0.8 | 0.5 | -0.9 | -0.3 | -0.6 | 0.9 | 0.2 | 0.7 | -0.4 | -0.3 | -1.0 | -0.9 | 0.9 |
| **PC2** | 0.2 | 0.3 | 0.2 | 0.9 | -0.6 | -0.2 | -0.9 | 0.1 | -0.3 | 0.9 | -0.1 | -0.4 | 0.1 |
| **PC3** | 0.1 | 0.1 | 0.1 | -0.2 | -0.2 | 0.1 | 0.0 | -0.2 | -0.8 | -0.1 | 0.2 | 0.1 | -0.2 |

Another method of choosing the characteristics for a multiple regression model is to consider the predictive capability of the individual characteristics by interpreting the coefficient of determination from OLS regressions (table 6.2). Based on the $R^2$ statistic the characteristics relating to rock fabric in neither the 16 nor 64μm/voxel images correlate well with permeability, while specifically open pore fraction and formation factor, which relate more directly to the pore system, show much stronger correlations. Mean curvature, surface area, and the Euler Characteristic correlate reasonably well and justify further investigation. Each model's p-value of the F-statistic is lower than 0.05. With a chosen significance threshold of 95% the p-values indicate that each model has less than 5% probability of being equal to the intercept model; therefore, each individual characteristic provides a statistically significant description of permeability variance.

Table 6.2: The coefficient of determination from ordinary least squares modelling of each calculated characteristic (from the 5 µm/voxel, 16 µm/voxel, and 64 µm/voxel images) with Lattice Boltzmann permeability from the 5 µm/voxel image.

| **Characteristic** | $R^2$ **for log (k) vs. log (5µm/voxel characteristics)** | $R^2$ **for log (k) vs. log (16µm/voxel characteristics)** | $R^2$ **for log (k) vs. log (64µm/voxel characteristics)** |
|---|---|---|---|
| ***Rock Fabric*** | | | |
| Grain Size (GS) | 0.114 | 0.018 | 0.206 |
| Grain Sorting (Gsort) | 0.556 | 0.544 | 0.275 |
| Clay Fraction (CF) | 0.393 | 0.542 | 0.286 |
| ***Pore System*** | | | |
| Porosity Fraction (Po) | 0.612 | 0.780 | 0.221 |
| Open Pore Size (µm) (PS) | 0.564 | 0.332 | 0.216 |
| Open Pore Sorting (Psort) | 0.103 | 0.019 | 0.033 |
| Formation Factor (m=2) (F) | 0.770 | 0.932 | 0.871 |
| Formation Factor (m=2.5) (F) | 0.754 | 0.931 | 0.850 |
| Formation Factor (m=4) (F) | 0.740 | 0.928 | 0.875 |
| ***Minkowski Functionals*** | | | |
| Open Pore Fraction (OPF) | 0.567 | 0.841 | 0.899 |
| Surface Area (SA) | 0.071 | 0.770 | 0.643 |
| Mean Curvature (MC) | 0.555 | 0.719 | 0.488 |
| Euler Characteristic (EC) | 0.187 | 0.752 | 0.626 |

We now choose the most suitable predictor characteristics based on the combined results of the principal component analysis and the regression for each individual characteristic with permeability.

### 6.2.1 Rock Fabric

In unconsolidated sands, grain size, grain sorting, and packing structure have fundamental control over the pore system, and have shown strong correlation with permeability (R. R. Berg, 1970; Chapman, 1981; Detmer, 1995; Krumbein & Monk, 1943). However, diagenetic and lithification processes, such as chemical dissolution, recrystallization of minerals, and compaction alter the flow properties in consolidated systems (Hayes, 1979). Even though the PCA results show that grain size and sorting align well with the main principal components, table 6.2 indicates that Precipice Sandstone grain properties do not correlate well with permeability. One could argue that such rock properties have a significant influence on fluid flow; however, the relationships between these simple measurements of fabric properties and permeability are not evident in this dataset. In the remainder of the thesis, I focus on those characteristics that relate more directly to the pore system and show stronger individual correlation with computed permeability.

### 6.2.2 Open Pore Fraction, Pore Size, and Formation Factor

The PCA results show that open pore fraction and formation factor share considerable information with the first principal component in both image resolutions (table 6.1). Table 6.2 indicates that these are the characteristics that correlate best with permeability, for both 16 and 64 μm/voxel images. $R^2$ for the correlation between open pore fraction and permeability is lower in the 5μm/voxel image, compared to the 16 and 64 μm/voxel images. Figure 6.2a and b plot simulated permeability against open pore fraction for the 16 and 64 μm/voxel images of the 8 mm sub-plug. The correlation is relatively poor at 5μm/voxel image resolution since relevant factors such as the length scale and connectedness of the pore system make no direct contribution to the open pore fraction characteristic. However, at lower image resolutions open pore fraction is no longer a direct measure of sample porosity, but rather the resolved fraction of the larger actual pore volume; i.e. pores larger than some resolution-dependent length cut-off. Figure 6.2b demonstrates an excellent correlation between open pore fraction and permeability in the 64 μm/voxel images. I postulate that when the resolution is such that the length cut-off is close to a controlling length scale of the pore system (e.g. the critical length), then the fraction of open pore space correlates well to the number of transport pathways relevant for permeability.

The correlation coefficient for pore size shows that it is a stronger predictor characteristic in the 16μm/voxel image, which retains more geometric information compared to the 64μm/voxel image (table 6.2 and figure 6.2c and d). Even though the pore size correlation coefficient is relatively low, being the only direct measure of size in these low-resolution images it may contribute to the statistical description of permeability in a multiple model, and we choose to include it in the subset of characteristics for further analysis.

Formation factor represents relative electrical conductivity; however, in low-resolution images, where electrical flow paths are poorly characterized, formation factor computations do not provide reliable information on the electrical properties of the rock. This study shows similar results than those of *Arns et al.* [2001a] with higher computed formation factor for lower resolution images. Additionally, the correlation coefficient between formation factor computed on the 5 µm/voxel image and that from the 16 and 64 µm/voxel images is 0.5 and 0.3 respectively, indicating that formation factor is poorly correlated with itself between image resolutions. Here the formation factor computation is tuned to take into account the scaled micro-porosity information contained in the gray scale value of each intermediate voxel. Computation results with $m = 2$, 2.5, and 4 show only minor differences in the correlation coefficients when modelled against permeability (see section 4.6.3 for a discussion on the motivation for selecting these values for $m$). For each value of $m$ the correlation coefficient for formation factor is lowest in the 5 µm/voxel image and highest in the 16 µm/voxel image. I suggest that in the lower resolution images, the formation factor computation appears to incorporate some measure of connecting channel size from image gray scales and therefore becomes a reasonable predictor of permeability (figure 6.2e and f). Additionally, when computing gray scale sensitive formation factor values in lower resolution images, the smaller pores, which contribute to permeability but which are not fully resolved in lower resolution images, are still taken into account because they are represented as intermediate gray scale values. It is expected that the range of resolutions for which formation factor is a useful predictor will vary between samples as a function of rock texture, and it is likely that the correlation coefficient will drop off at even lower resolutions.

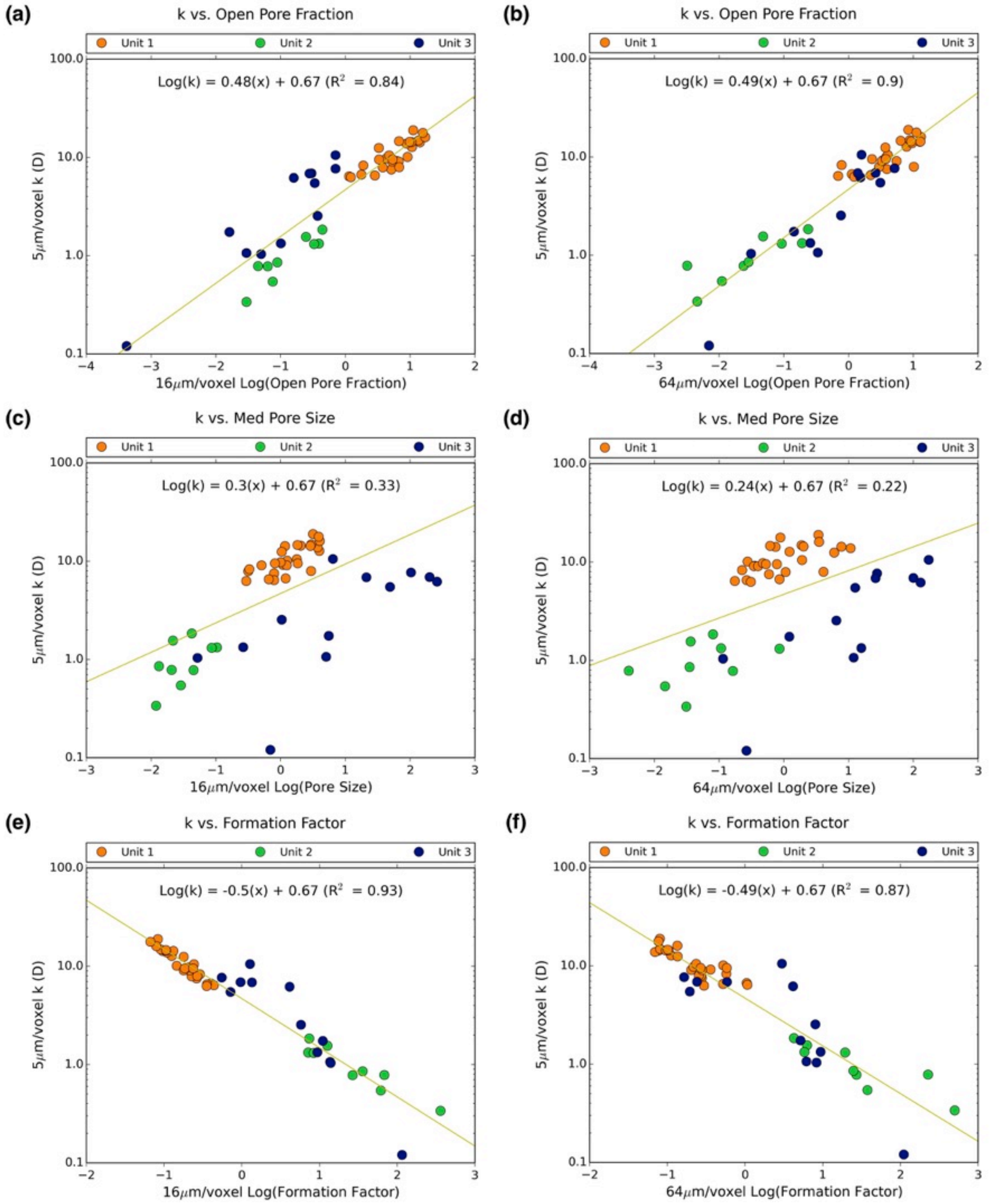

Figure 6.2: The correlations between permeability and open pore fraction (a and b), open pore size (c and d), and formation factor (e and f) calculated from the 16 and 64 μm/voxel images.

### 6.2.3 Sensitivity to Segmentation Parameters

Unlike formation factor, which takes into account the gray scale values from the original tomogram, open pore fraction is directly dependent on the image gray scale segmentation threshold, therefore, the sensitivity of this promising correlation to the segmentation threshold parameter should be explored. Figure 6.3a and b show open pore fraction from the 64 μm/voxel image and its correlation with permeability as a function of simple gray scale thresholding. As the threshold increases the open pore fraction and its range increase indefinitely as more voxels are included in the segmented pore phase. The correlation coefficient with permeability increases to a maximum and then decreases. The maximum $R^2$ of 0.915 is very similar to the $R^2$ of 0.899 (reported in table 2), indicating that the component of the pore system that correlates well with permeability can be captured over a relatively large range of gray scale thresholds (200 gray scale values between 1900 and 2100). Even if I set a minimum correlation coefficient value of 0.85 (only 0.05 from the reported value in the table 6.2) the range of gray scale segmentation thresholds to achieve a $R^2$ value 0.85 increases from 200 to ~400 between 1800 and ~2200. This result indicates that the predictive model based on open pore fraction is relatively independent of the segmentation parameters used for the low-resolution image; however, it does not eliminate the need to carefully select the appropriate segmentation thresholds during image processing.

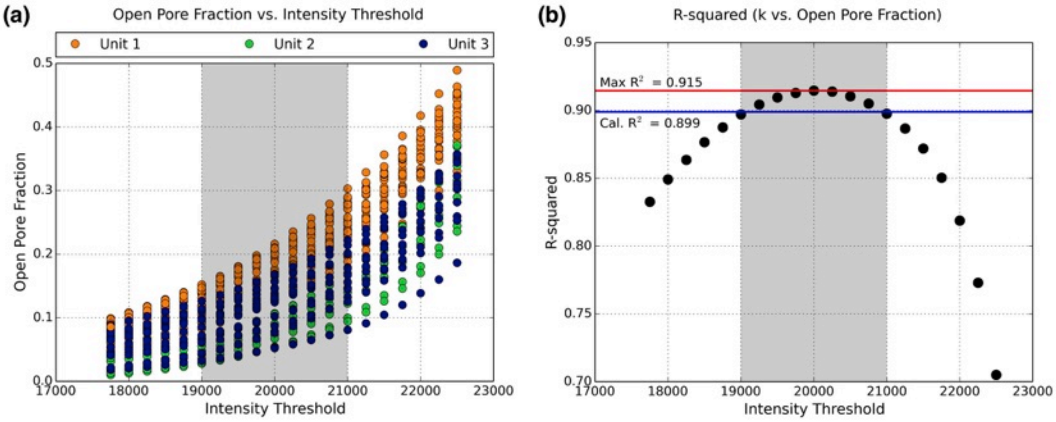

Figure 6.3: a) Open pore fraction as a function of the gray scale threshold value; b) The correlation $R^2$ between permeability and open pore fraction as a function of the gray scale threshold. The shaded areas show the range of gray scale values over which permeability remains highly correlated to open pore fraction, indicating that the statistical model is relatively independent of the image segmentation parameters.

The question now arises whether it is possible to optimise image acquisition based on sample composition. Sheppard et al. (2004) describe the challenges of segmenting natural materials with multiple phases and often sub-resolution features that blur the edges defining boundaries between phases. Clearly one would always desire the highest possible image quality, regardless of image resolution; therefore, it is important to optimize the acquisition conditions (flux, sample positioning to optimize field of view, sample stability to prevent drift, etc.). In lower resolution images the proportion of voxels with intermediate gray scale values increase as a result of the mixed volume effect, therefore there is increased potential for segmentation errors. The "cascading active contour" segmentation method used in this project (see section 4.2) requires input values for the gray scale threshold and gradient between two phases. The segmentation method uses these parameters to actively optimize the positioning of the boundary in the segmented image. In lower resolution images the gradient between two phases are generally lower compared to high-resolution images. For complex samples with multiple clay phases producing intermediate gray scale values it could be worth considering the use of an injected contrasting agent to elevate the attenuation of the pore volume above the lower attenuation grain phases. I suggest that this approach ought to increase the gradient between pores and the main framework grain boundaries, which should simplify the segmentation process to an extent.

## 6.3 Statistical Calibration: Multiple Characteristics

Combining predictor characteristics into multiple linear models has the potential to improve predictive capabilities and serves as the second step in calibrating the statistical models. With the knowledge of the predictive behaviour of each individual rock characteristic I make use of the statistical method known as forward selection (see section 4.7.2 Statistical Methods) to compile multiple linear models to predict absolute permeability. Based on the results from the principal component analysis and the regression of each characteristic with permeability, I suggest that some combination of open pore fraction, pore size, formation factor and the Minkowski Functionals are likely to generate good multiple linear models of absolute permeability. It is important to emphasise that the intention is to develop a workflow rather than an empirical model for predicting permeability. It is possible that other samples will require different statistical models depending on their textures and the image resolution.

Table 6.3 shows six multiple models and their $R^2$ values for regressions using characteristics from the 5, 16, and 64 μm/voxel images. Each model's p-value of the F-statistic is lower than 0.05, indicating that each model is significantly different from the intercept model. The two best individual characteristics are open pore fraction and formation factor, and a multiple linear model containing both (model 1) provides an excellent description of permeability, especially in the 16 μm/voxel image.

Table 6.3: The coefficient of determination from ordinary least squares modelling of five combinations of predictor characteristics (from the 5 μm/voxel, 16 μm/voxel, and 64 μm/voxel images) with Lattice Boltzmann permeability from the 5 μm/voxel image.

| **Multiple Model** | $R^2$ **for log (k) vs. log (5μm/voxel characteristics)** | $R^2$ **for log (k) vs. log (16μm/voxel characteristics)** | $R^2$ **for log (k) vs. log (64μm/voxel characteristics)** |
|---|---|---|---|
| 1) OPF, F | 0.843 | 0.932 | 0.908 |
| 2) OPF, PS, F | 0.965 | 0.963 | 0.912 |
| 3) SA, MC, EN | 0.696 | 0.777 | 0.677 |
| 4) OPF, SA, MC, EN | 0.830 | 0.955 | 0.922 |
| 5) SA, MC, EN, F | 0.910 | 0.953 | 0.875 |
| 6) OPF, PS, F, SA, MC, EN | 0.971 | 0.969 | 0.927 |

Even though pore size alone does not appear to contain any significant predictive capability (table 6.2 above), adding it to model 1, to produce multiple model 2, significantly increases the correlation coefficient in the 16μm/voxel image. This is not true for the 64 μm/voxel data, where adding pore size to model 1 only increases the $R^2$ by 0.004. This indicates that at low-resolution the pore size characteristic no longer has any predictive capability, showing that the 64 μm/voxel image contains no direct geometric information that contributes to a model for permeability. Instead the pore geometry is now represented by intermediate gray scale values and is accounted for by the formation factor, which incorporates gray scales during computation.

As individual characteristics the Minkowski functionals generate promising $R^2$ values, particularly for the 16 μm/voxel image (table 6.2 above). However, when combined in model 3, the correlation coefficient is less impressive at 0.8, 0.78, and 0.67 for the 5, 16, and 64 μm/voxel images respectively. Only when open fraction or formation factor is added to surface area, mean curvature and the Euler Characteristic in models 4 and 5 does the $R^2$ improve. Furthermore, model 6 contains open pore fraction, pore size, and all three of the remaining Minkowski Functionals, and produces an $R^2$ of 0.968 and 0.927 for the 16 and 64 μm/voxel data, which is only marginally better than the correlation coefficients for models 1 and 2. It is therefore clear that the Minkowski Functionals do not contribute additional information to a multiple model, which is not already accounted for by open pore fraction, pore size, and formation factor. Based on the results in table 3 we therefore identify models 1 and 2 for use in predicting permeability in the 25 mm 64 and 16 µm/voxel images respectively.

The coefficient of determination alone, though a valuable measure of precision, cannot be used to determine the quality of a model. Model residuals (the differences between the predicted and observed values) should ideally show a random distribution around zero with no clustering of the data points and no clearly discernable patterns, the presence of which may point to some systematic bias in the model (Draper & Smith, 2014). Figure 6.4a shows the simulated permeability from the 5 µm/voxel image plotted against the predicted permeability from the 16 µm/voxel image using multiple linear model 2 (open pore fraction, open pore size, and formation factor). Figure 6.4b shows the model residuals plotted against the predicted values. Figure 6.4c and d show similar data for the 64 µm/voxel image obtained from model 1 (open pore fraction and formation factor). Upon visual inspection the residuals in figures 6.4b and d show relatively random distributions indicating that a linear model is unbiased and appropriate for the data. There are a few data points at lower permeabilities with higher residual values, which I propose is a consequence of the low-permeability data being more scattered. It also shows the difficulty of predicting lower permeability values (<1000 mD) from such low-resolution images.

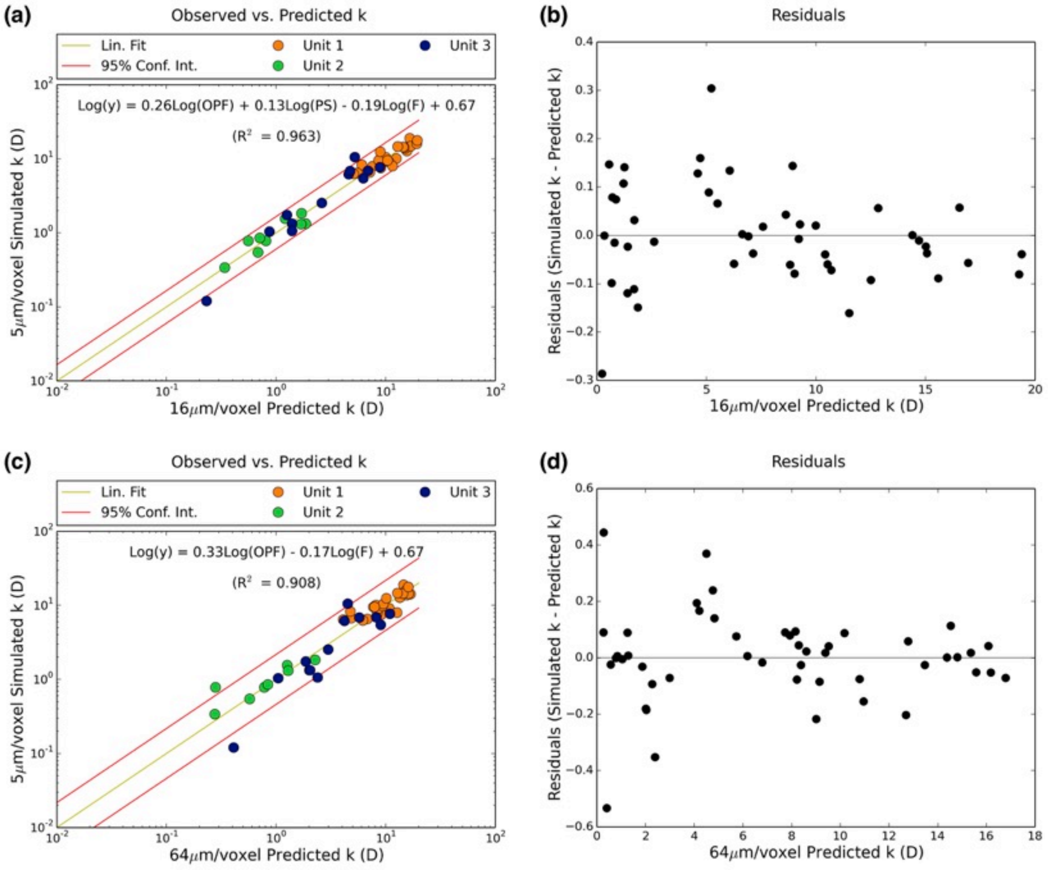

Figure 6.4: Calibration of statistical models over the small field of view of the highest resolution image. The simulated permeability from the 5 µm/voxel image plotted against the predicted permeability from the multiple model containing open pore fraction, open pore size, and formation factor from the 16 µm/voxel image (a) and open pore fraction and formation factor from the 64 µm/voxel image (c). Multiple linear model residuals plotted against the predicted permeability values have no apparent systematic bias (b and d).

## 6.4 Predicting Permeability in the 25mm Core Plug

The last step in the workflow is to predict permeability from the images of the full 25 x 80 mm core plug. Using the statistical calibration of model 1 (open pore fraction and formation factor) for the 64 µm/voxel image and model 2 (open pore fraction, open pore size, and formation factor) for 16 µm/voxel image, figure 6.4 shows the predicted absolute permeability for the 25 mm core plug from both image resolutions. As before, the predictor characteristics are computed on several sub-volumes within each unit separately. Figure 6.5 shows permeability as a single value for each rock unit, which is the average of the predicted permeability of the sub-volumes. Each unit indicated in figure 6.5 contains 9 sub-volumes (3 x 3 x 1), except units 8 and 12, which both contain 18 sub-volumes (3 x 3 x 2). All sub-volume x and y dimensions are 310 x 310 voxels. Certain sections in the core plug such as units 2 and 3 show relatively high permeability, despite their fine-grained rock fabric and apparently closed pore systems compared to that of units 11 and 12.

The best imaging resolution that could be achieved over the full 25 x 80 mm volume was 16 μm/voxel, a dataset of 1800 x 1800 x 5000 voxels, which was shown in section 5.1 to be insufficient to allow direct simulation of permeability. In the absence of accurate direct simulations, and having achieved excellent statistical permeability predictions from the 16 μm/voxel calibration data (figure 6.4a), the predicted permeability over the full 25 x 80 mm volume serves as a proxy for directly computed permeability.  One of the key results in the thesis the comparison between predicted permeability for the 8 mm sub-plug (the calibration volume) and 25 mm core plug, which are shown in figure 6.5. The 1:1 $R^2$ values show that predictions from the low-resolution 64 μm/voxel image match those from the 16 μm/voxel image very well for both the 8 x 15 mm calibration volume ($R^2$ = 0.93) and the as-yet-unexplored 25 x 80 mm volume ($R^2$ = 0.90). This is an exciting result since two different statistical models, applied to two images with different resolutions, predict very similar permeabilities.

As a word of caution, the high-resolution data from the 8 mm sub-plug underpins the permeability predictions made over the full 25 x 80 mm volume from the 16 and 64 μm/voxel images. If the sub-plug does not represent an adequate range of rock textures, so that significant extrapolation of the statistical model is required beyond the range of rock characteristics captured in the 8 mm sub-plug, then uncertainties in the predicted permeability are bound to increase. Future research will need to look into this aspect in more detail. An approach likely to provide some quantitative data is to collect a second sub-plug from a different location, and test the predicted permeability over the whole 25 mm core plug from the two calibration volumes.

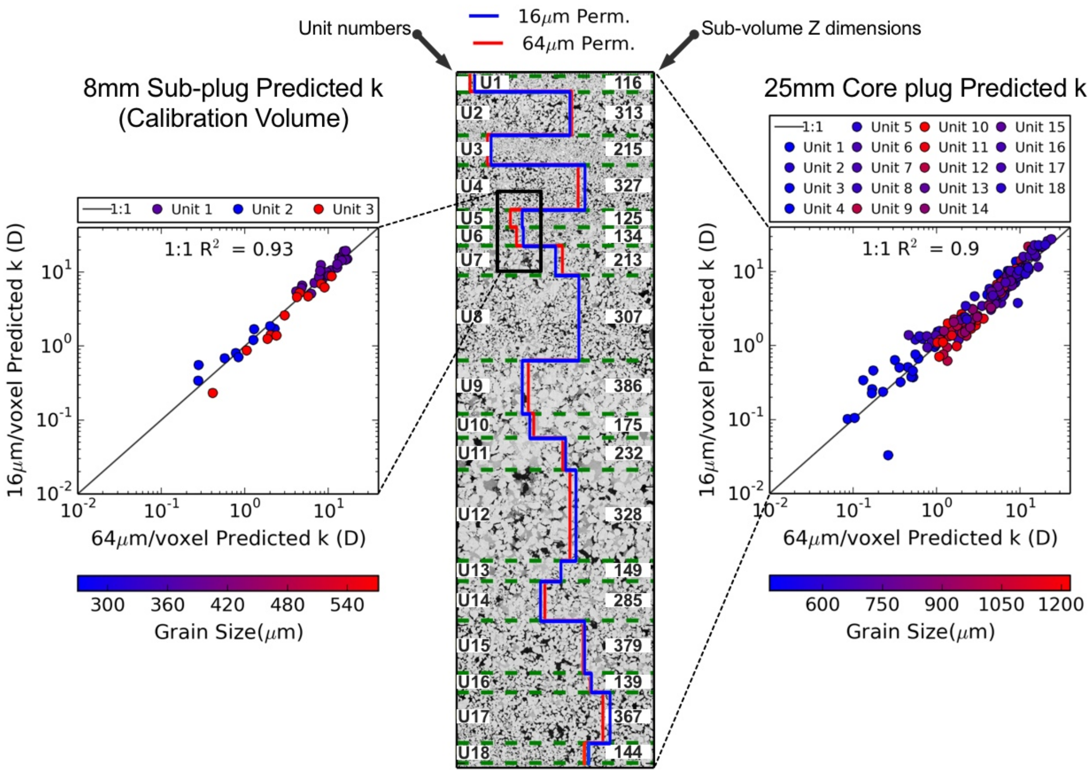

Figure 6.5: The predicted permeability of the 25 mm core plug computed from multiple linear model 2 (open pore fraction, open pore size, and formation factor) for the 16 μm/voxel image, and multiple linear model 1 (open pore fraction and formation factor) for the 64 μm/voxel image. Green horizontal stippled lines indicate the boundaries between rock units and the black box indicates the approximate location of the 8mm sub-plug. The scatterplots compare the predicted permeabilities from the 16 and 64 μm/voxel images for the 8 mm sub-plug calibration volume (left) and the 25 mm core plug (right).

Closer inspection of figure 6.5 above shows there is one sub-volume for which the predicted permeability value using the 16 μm/voxel image of the 25 mm core plug plots well below the 1:1 line. Further investigation reveals that this sub-volume is from unit 1 and that it contains a significant amount of masked area (figure 6.6). I propose that this sub-volume is therefore not representative of the unit and that the formation factor and open pore fraction computations from this sub-volume do not fall within the appropriate range expected by the statistical model. The adjacent sub-volume also contains some masked area; however, in this case it is clearly not enough to influence the permeability prediction (figure 6.6).

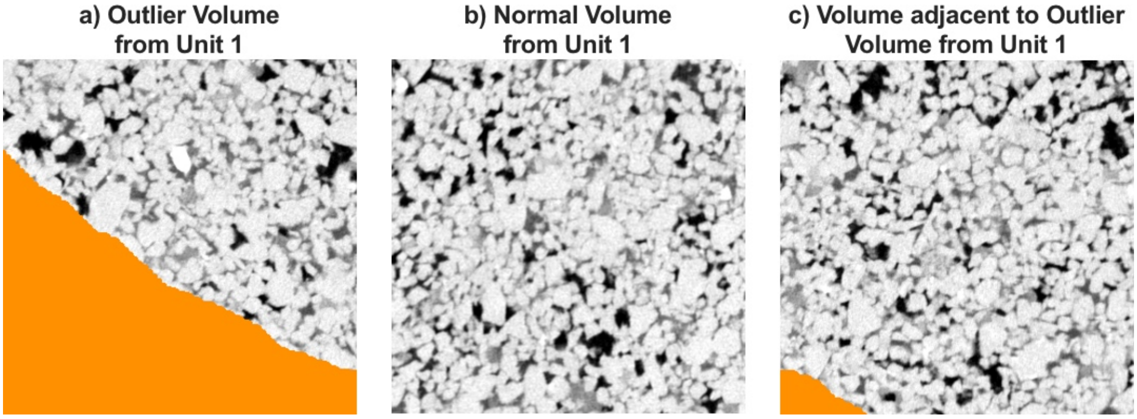

Figure 6.6: Example images from the outlier sub-volume containing masked area (orange) and plotting far from the 1:1 line (a); a normal sub-volume without any masked area plotting near the 1:1 line (b); and a normal sub-volume with a small amount of masked area plotting near the 1:1 (c).

# 7 Permeability Results and Discussion: Sample 2

After initial development of the workflow (using sample 1) I apply the workflow to sample 2, another Precipice core plug of similar character to sample 1. Sample 2 is generally finer grained and overall better sorted compared to sample 1 based on a visual assessment of 2D slices from the 3D μCT tomograms. Sample 2 contains a range of grain sizes and lamellae in the mm to cm range. As for sample 1, the 25 mm core plug of sample 2 was first imaged rapidly as part of a bundle with other cores to produce image 1) a low-resolution image (LR) at ~ 61 μm/voxel, after which image 2) an intermediate resolution image (IR) at ~16 μm/voxel was acquired through a high-fidelity scan of the core plug in isolation. Finally, image 3) a high-resolution image (HR) at ~5 μm/voxel was acquired by means of a region of interest scan of a 8mm diameter 15 mm long region in the original core plug (whereas the HR image for sample 1 was collected from a physically cored sub-plug). The three images are aligned to one another using the algorithm described in section 4.2 (Latham, Varslot, & Sheppard, 2008; Latham, Varslot, Sheppard, et al., 2008), after which one is left with the following image pairs:

a. 5 μm/voxel HR image overlapped with the 16 μm/voxel IR image,
b. 5 μm/voxel HR image overlapped with the 61 μm/voxel LR images,
c. 16 μm/voxel IR image overlapped with the 61 μm/voxel LR images

Figure 7.1 shows the difference in resolution between the images and the approximate location of the sub-plug for sample 2 and figure 7.2 shows the results from the unitisation procedure applied to the 8mm region of interest.

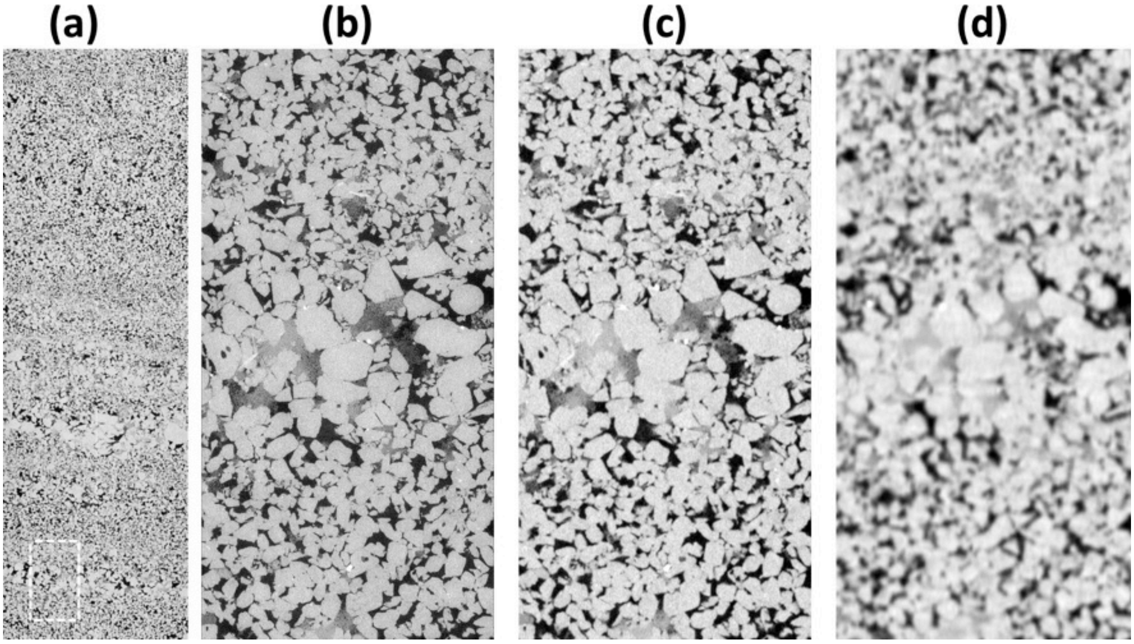

Figure 7.1: a) The 25 mm core plug of sample 2 imaged at 16 μm/voxel; b) the 5 μm/voxel image of the 8 mm region of interest; and the overlap regions from the 16 μm/voxel and 61 μm/voxel images (c and d respectively). The white square indicates the approximate location of the 8 mm region of interest.

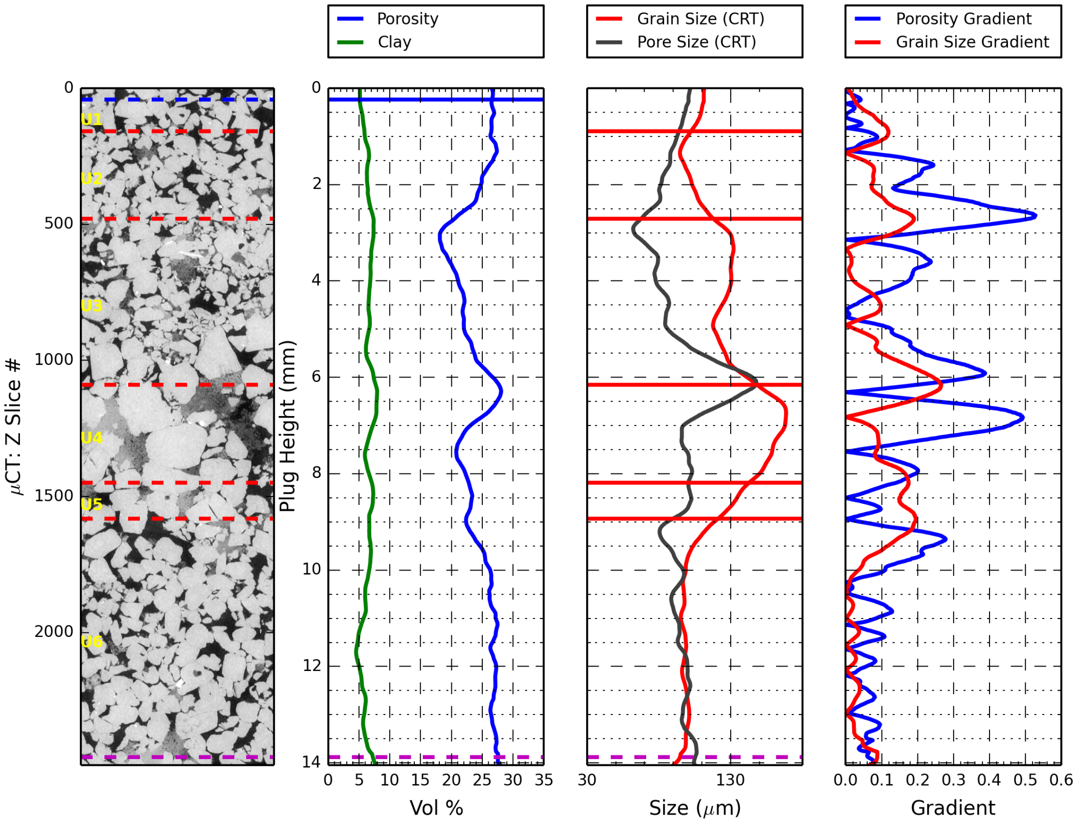

Figure 7.2: 8mm region of interest image unitisation for sample 2. Horizontal red and blue lines indicate boundaries from the grain size and porosity logs respectively.

Sample 2 statistical calibrations and permeability predictions in the 25 mm core plug were done using the same multiple linear models as for sample 1 (see chapters 6.2 and 6.3). For the IR 16 µm/voxel data calibration and permeability prediction were based on multiple linear model 2 (open pore fraction, open pore size, and formation factor), while for the 61 µm/voxel data calibration and permeability prediction were based on multiple linear model 1 (open pore fraction and formation factor). Principal component analysis was not performed on sample 2. Figure 7.3 shows statistical calibration data for the intermediate resolution 16 µm/voxel image (figure 7.3a) and the low-resolution 61 µm/voxel image (figure 7.3b). Notably the $R^2$ of the models are not as high as for the first sample; however, they appear good enough to suggest that the low-resolution images contain the relevant information on the pore system to allow permeability prediction.

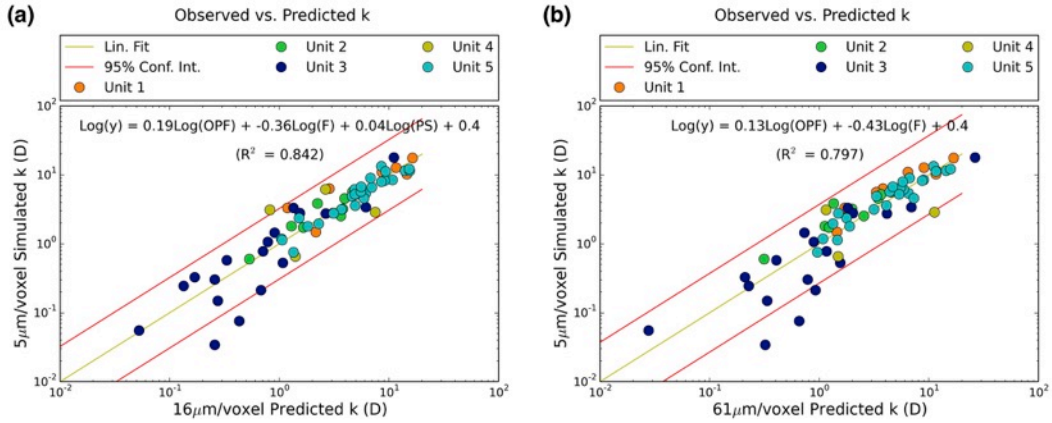

Figure 7.3: Calibration of statistical models for sample 2. The simulated permeability from the 5 µm/voxel image plotted against the predicted permeability from the 16 µm/voxel image (a) and the 61 µm/voxel image (b).

I suggest that the two main causes of the poor correlations are related to a) the quality of the high-resolution image used for permeability computation, and b) the fact that unit 3 has the smallest average pore size (figure 7.2 above). Here the high-resolution image was not collected on a physically cored sub-plug, but rather as a ‘region of interest scan’, which means that the high-resolution image was collected by physically positioning the original large scale sample closer to the x-ray source, thereby reducing the field of view and increasing the image resolution. This technique reduces the contrast-to-noise ratio in the high-resolution image (figure 7.4a), directly impacting image segmentation. Most notably the pore space contains isolated groups of non-pore voxels (figure 7.4b), which in turn impact the permeability computation because non-pore voxels do not allow fluid flow. More critically however, the pore channels controlling fluid flow would also be constricted or completely blocked as a result of the presence of inaccurate non-pore voxels. The resulting permeability data for calibration are therefore less reliable, thereby leading to poorer statistical correlations. Please note that the predictor characteristics are computed from high-quality intermediate- and low-resolution images, which are not affected by the region-of-interest scanning method. Figure 7.3 shows that even though most units contribute to the larger variance and therefore smaller correlation coefficient in this model, unit 3 shows the most spread of all. I propose that the increased spread from unit 3 is a result of its small pore size, which increases the pore surface area and therefore results in higher proportions of intermediate gray scale voxels. The effect is confounded by the relatively poor image quality in the high-resolution image, which further increases the fraction of intermediate gray scale voxels at pore-grain boundaries.

To test the hypothesis of non-pore voxels blocking the pore channels critical for fluid flow I compute a new set of permeability data using a micro-porosity segmented image; specifically I set the first 26 gray scale values of the 100 intermediate gray scale voxels to permit fluid flow as if they were open pore voxels, thereby removing the negative effect of some of the isolated non-pore voxels and those in the connecting pore channels (figure 7.4c). An unavoidable affect of this procedure, especially given the low signal to noise ratio of the original tomogram, is the impact on other parts of the image where legitimate intermediate gray scale voxels may be changed to permit fluid flow in the same way as open pore space. The calibration results using this new set of permeability data show significant improvement and give $R^2$ values of 0.93 and 0.91 for the 16 and 61 µm/voxel images respectively (figure 7.5a and b). The 1:1 comparisons of the predicted permeability data are nearly as good as for sample 1 (figure 7.5c and d), showing that 16 and 61 µm/voxel models produce similar predicted permeability values. This result demonstrates that a region of interest scan HR image can be sensitive to errors in segmentation and the resultant computed permeability directly impact the statistical calibrations and the quality of the predicted data.

It is true that removing isolated clusters would completely remove the impact of isolated clusters in the pore spaces; however, the main objective of this section of work was to investigate whether non-pore voxels in the connecting pore channels impact on permeability computations and the resulting statistical correlations. Non-pore voxels in the pore channels are unlike to be impacted by removing isolated clusters, which is why I chose to set the first 26 gray scale voxels to permit fluid flow. This method targets both the isolated clusters in the larger pore spaces and the intermediate gray scale voxels in the pore channels, and provides support for the conclusion that accurate representation of pore connectivity is more important for developing statistical models than completely removing isolated clusters. Furthermore, high-quality images that sufficiently capture the connecting pore channels are unlikely to have detrimental imaging artefacts in the larger pore spaces.

Samples 1 and 2 presented in this thesis contain a wide range of rock textures from fine to coarse grained, which makes them ideal for testing correlations between rock characteristics and petrophysical properties. However, both samples are from the same formation of sandstone, which may limit the generality of the results. Further work is required to fully understand the impact of the choice of sub-plug location and whether or not similar statistical relationships exist in samples from other sandstone formations.

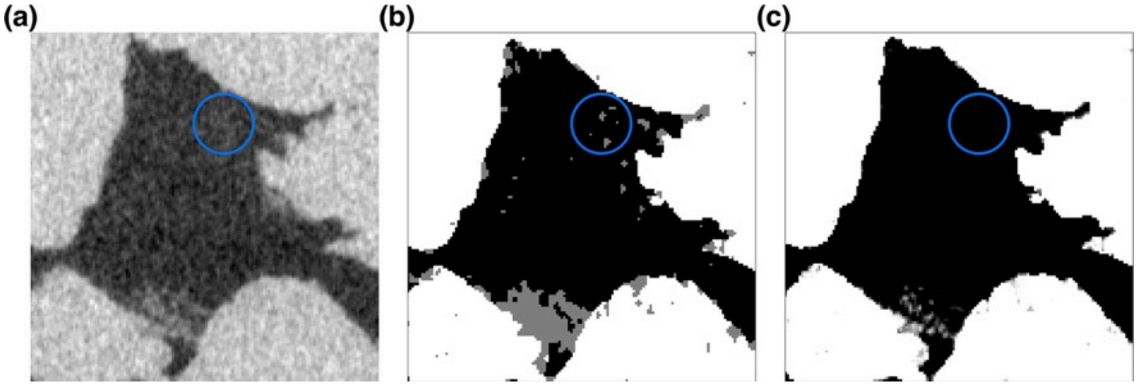

Figure 7.4: A 2D slice from the original tomogram showing the presence of noise (a), the segmented image of the same area showing isolated clusters of non-pore voxels in the pore space (b), a slice of the micro-porosity segmented image where the first 26 gray scale values are set to permit fluid flow (c). It is also important to note that this procedure has the potential to impact other parts of the image, as can be seen in the cluster of legitimate intermediate gray scale values in the bottom centre of the image, which changes to allow fluid flow from image (b) to (c).

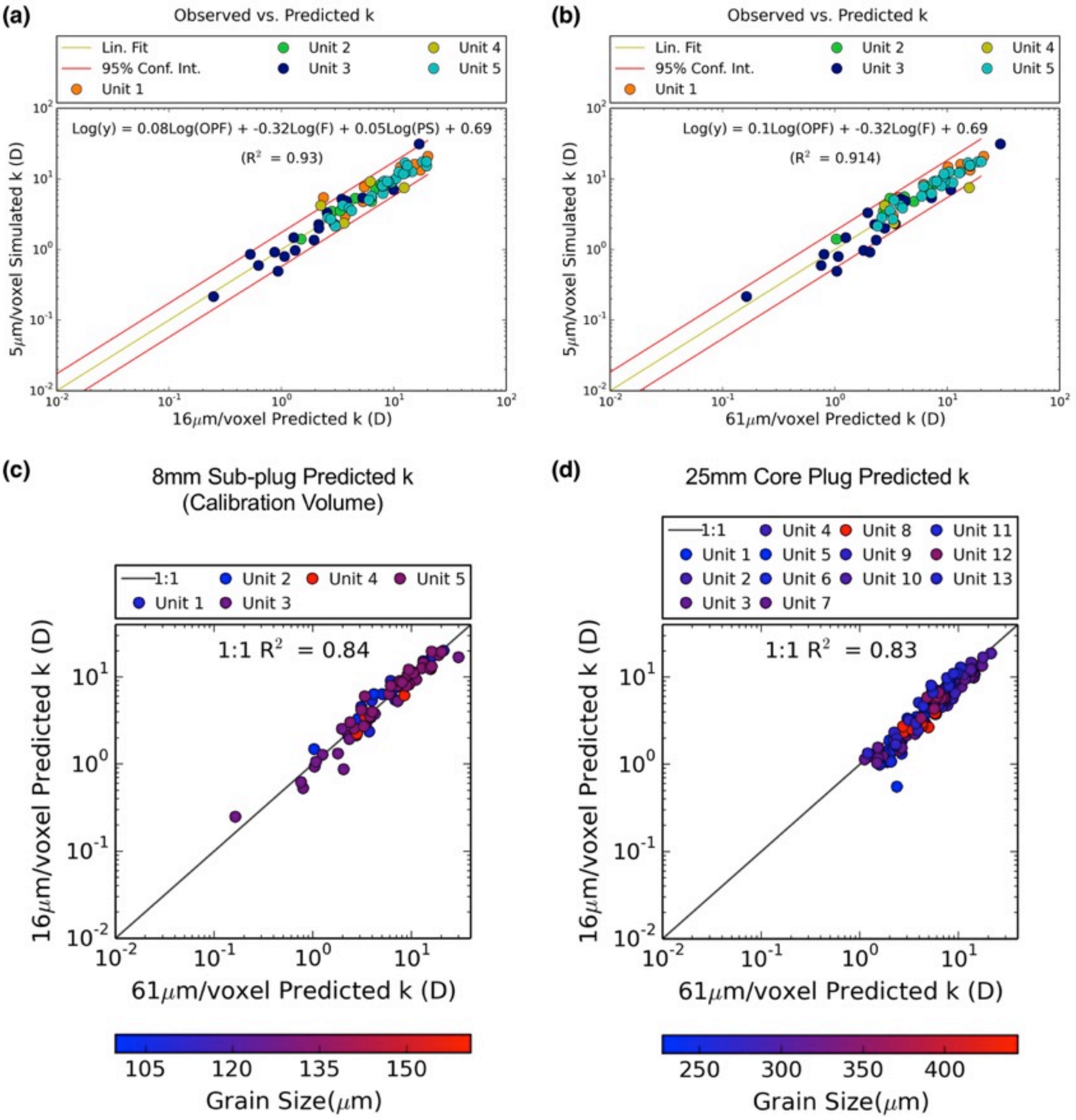

Figure 7.5: The simulated permeability from the 5 µm/voxel image plotted against the predicted permeability from the 16 µm/voxel image (a) and the 61 µm/voxel image (b) making use of a micro-porosity segmentation to adjust the permeability computation. Comparing the predicted permeability for the 8 mm sub-plug (c) and the 25 mm core plug (d).

# 8 Capillary Pressure Results and Discussion: Sample 1

In this chapter I demonstrate the use of morphology-based capillary pressure simulations on segmented µCT images to produce primary drainage and imbibition curves. Furthermore I process the capillary pressure data by fitting the Brooks-Corey function to extract threshold pressure and lambda (a parameter describing the shape of the drainage flow capillary pressure curve and is related to pore size distribution), which, in addition to residual non-wetting phase saturation, I later use in statistical correlations with predictor characteristics.

## 8.1 Pore Morphology-Based Capillary Pressure Simulations

As a first step to produce primary drainage and imbibition curves I performed pore-morphology-based simulations on the segmented HR images. The simulation requires Euclidean distance transform (EDT) data to which it applies a covering radius transform (CRT). For drainage flow the simulation starts by setting a CRT threshold equal to the maximum radius in the pore space (indicating low capillary pressure) and determines the wetting phase saturation of the pore space by computing the fraction of pore volume occupied by spheres of that threshold and smaller (Knackstedt et al., 2004). Selecting successively smaller sphere radii thresholds increases the capillary pressure and alters the corresponding wetting phase saturation. For imbibition flow the CRT threshold is set equal to the minimum value (indicating high capillary pressure) followed by the computation of the fraction of pore volume occupied by spheres of the threshold size and larger. Selecting successively larger sphere radii thresholds decreases the capillary pressure and alters the corresponding wetting phase saturation. The imbibition simulation also checks for isolated clusters of pore space below the threshold value, which are not included in the computations at subsequent threshold values. These isolated clusters represent the trapped fraction of non-wetting phase. The results include drainage and imbibition curves expressed in terms of the pore radius, the reciprocal of which is a measure of pressure (1/pore radius), the wetting phase saturation as a fraction of the total resolved pore volume, and the fraction of trapped non-wetting phase (figure 8.1).

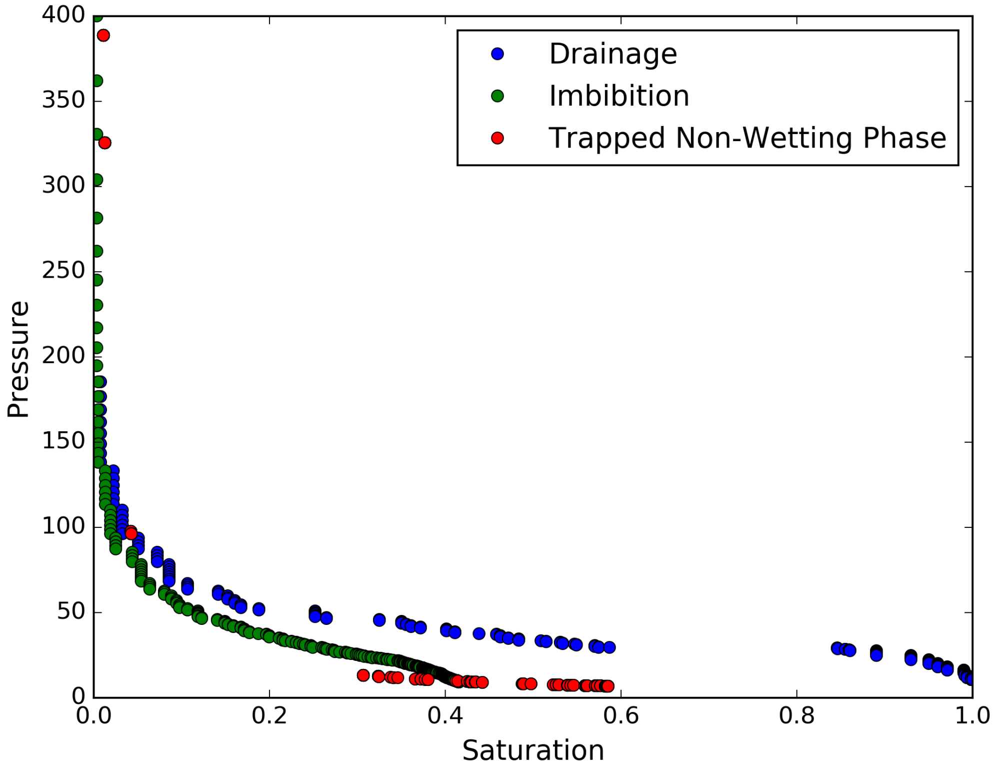

Figure 8.1: Drainage and imbibition curves from pore morphology-based capillary pressure simulations (capillary pressure on the y-axis). The trapped non-wetting phase curve defines the pressure at which snap-off occurs to trap a fraction of the non-wetting phase.

## 8.2 Parameterisation of Morphology-Based Capillary Pressure Curves

Absolute permeability is a relatively simple petrophysical property in that the simulation results provide a single number for each sub-volume, which could be used for statistical analysis. Here the result for each simulation volume is a series of data points defining a set of curves. I process each drainage curve by describing the capillary pressure ($P_c$) mathematically in terms of the Brooks-Corey function (Brooks & Corey, 1964) (eq. 8.1), which contains three critical parameters: the threshold injection pressure ($P_{ct}$), residual water saturation ($S_{wr}$), and lambda ($\lambda$).

Another option would have been to compute the Leverett-J function (Leverett, 1941) for each sub-volume. The Leverett-J function depends on several input values, which include capillary pressure, porosity, permeability, and fluid contact angle. It is possible to derive porosity and permeability from the high-resolution images (and has been done in this thesis); however, the contact angle in this instance would be an assumed value. Furthermore the Leverett-J function provides just one output value for each sub-volume to describe the drainage capillary curve. Here I have chosen to use the Brooks-Corey function because it relies directly on the measured capillary pressure and fluid saturation values computed during simulation. By fitting a Brooks-Corey function to the simulated data I am presented with at least three parameters that describe the drainage capillary curve for each sub-volume. It follows that there are three parameters available for statistical correlation testing, rather than the one value derived from the Leverett-J function.

$$P_c = P_{ct}\left(\frac{1 - S_{wr}}{S_w - S_{wr}}\right)^{1/\lambda} \tag{8.1}$$

The injection threshold pressure represents a relatively intuitive value describing the pressure required to initiate breakthrough of a non-wetting phase into the pore system of a porous medium. The residual water saturation quantifies the fraction of wetting phase, in many cases water, which cannot be driven from the formation by the non-wetting phase, regardless of increases in the injection pressure. Lambda is less intuitive, but essentially controls the rate at which the steepness of the curve increases as the injection pressure increases. In physical terms the part of the curve that increases sharply in steepness generally relates to when non-wetting fluid starts to invade the smaller pore spaces and the crevices and corners of the pore volume.

In general, and not with specific reference to the method based on CRT values used here, the imbibition curve combined with the physical phenomena of hysteresis makes it possible to quantify the fraction of residual non-wetting phase. Here the CRT method can only represent the trapping aspect of the hysteresis phenomena. In terms of $CO_2$ storage the fraction of residual non-wetting phase represent the fraction of $CO_2$ remaining in the pore system as a result of capillary trapping. The difference between one and wetting phase saturation at the end of imbibition flow represents the trapped fraction of non-wetting phase.

Notably the data points for the drainage curve in figure 8.1 do not define a smooth curve. For a range of pressure values there may be just a single saturation value, which demonstrates that the pressure needs to increase to a certain value for the injected non-wetting phase to access the next pore space and cause a change to the wetting-phase saturation. Additionally, the drainage simulation is not capable of computing realistic residual water saturations and reports zero as the lowest water saturation. In the data processing stage prior to performing the Brooks-Corey modelling, for those data points with duplicate saturation values I retain only the maximum pressure value and the corresponding saturation value (figure 8.2a). The data series also contains several large jumps from one saturation value to the next. These gaps correspond to when the non-wetting phase gains access to and fills a pore space without the need for an increase in pressure. The range of saturation values spanning each of the jumps clearly exists in reality, but is not recorded by the simulation. The data processing step adds data points to these ranges to construct a capillary pressure curve that is more appropriate for Brooks-Corey modelling (figure 8.2b).

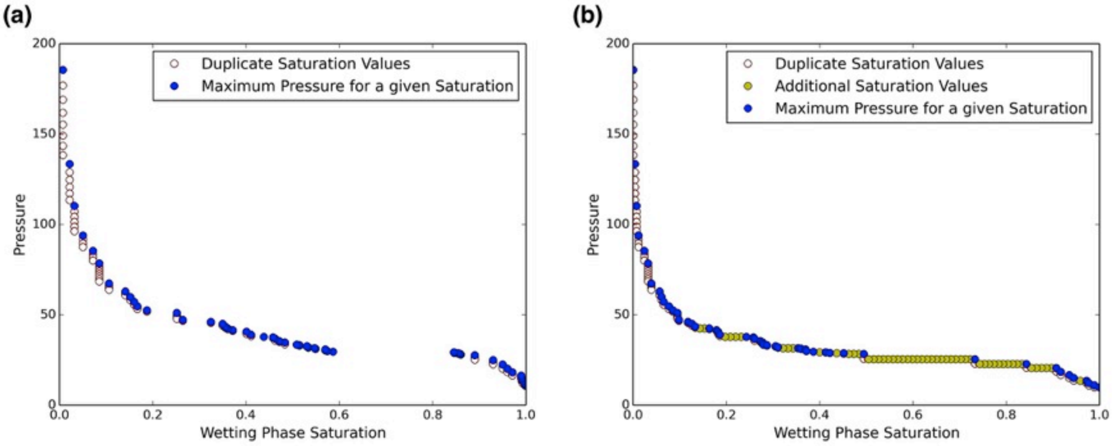

Figure 8.2: a) The original drainage simulation data showing duplicate saturation values (white dots with black edges) for a range of pressures. The blue data points are used for further processing. b) Additional data points in yellow filling the jumps in saturation values.

The parameters from the simulation results are used to correlate with the same rock characteristics to develop statistical models that are used to estimate the multi-phase flow parameters in volumes where there is not sufficient resolution for direct computation.

I perform the Brooks-Corey modelling using Python’s Curvefit module, a least squares method that requires an initial guess for each parameter in the function. The simplest approach is to set the initial guess for the residual water saturation

($S_{wr}$) to zero and lambda ($\lambda$) to 1. Testing indicated that the model fit is insensitive to initial guess lambda values below 5. At high wetting phase saturation values, as the pressure increases, the curve rises steeply and sometime irregularly before flattening out. The initial flattening of the curve is associated with the threshold capillary pressure. To estimate the threshold pressure for use in the Curvefit module I start by computing the ratio between pressure and saturation data, performing a linear interpolation between each data point, smoothing the ratio curve, and plotting it against saturation (figure 8.3a). The pressure to saturation ratio curve shows an inflection point at high saturation values, which corresponds with the threshold pressure. The next step is an iterative process that uses each saturation value as a break point in the ratio curve and computes a line of best fit for those data points below the breakpoint and a second line of best fit for those data points above the breakpoint, resulting in a set of lines for data below and above the series of breakpoints. The final step is identifies the pair of lines with a minimum intercept angle, and uses the pressure associated with the saturation of the intercept point as the threshold pressure (figure 8.3b). Before performing the Brooks-Corey modelling those data points below the estimated threshold pressure are removed. In physical terms these data points relate to the initial infiltration of the fluid into the rock and do not provide additional information useful to modelling the data with the Brooks-Corey function. In a final step of pre-modelling processing I include additional data points to extend the curve to a wetting phase saturation of 1. Figure 8.4 shows an example of the Brooks-Corey modelling performed on the x-direction simulated drainage capillary pressure curve for one of the sub-volumes from unit 1 in sample 1.

For the purposes of this study I focus on the injection threshold pressure for statistical modelling and prediction. Because the original simulation results do not approach the actual residual water saturation I do not consider $S_{wr}$ from morphology-based simulations for statistical modelling. The difference between 1 and the wetting phase saturation at the end of imbibition flow represents the non-wetting phase saturation ($S_{or}$), or in the case of $CO_2$ injection, the fraction of trapped liquid $CO_2$. In section 8.1.2 I briefly present and discuss the results of statistical modelling of $\lambda$ and $S_{or}$, however, in the case of $S_{or}$, because of the nature of morphology-based flow simulations, snap-off occurs at lower capillary pressure values than in reality, thereby increasing the residual non-wetting phase saturation.

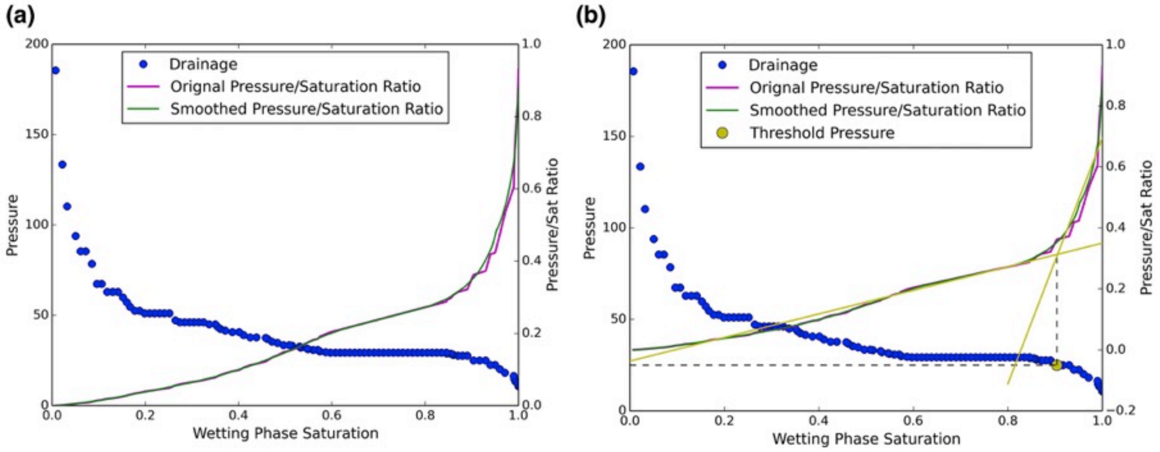

Figure 8.3:a) Plotting the ratio between pressure and saturation against saturation and smoothing the curve for analysis; and b) showing the set of linear models for data above and below the saturation breakpoints with a minimum intercept angle to define the threshold pressure and saturation coordinate.

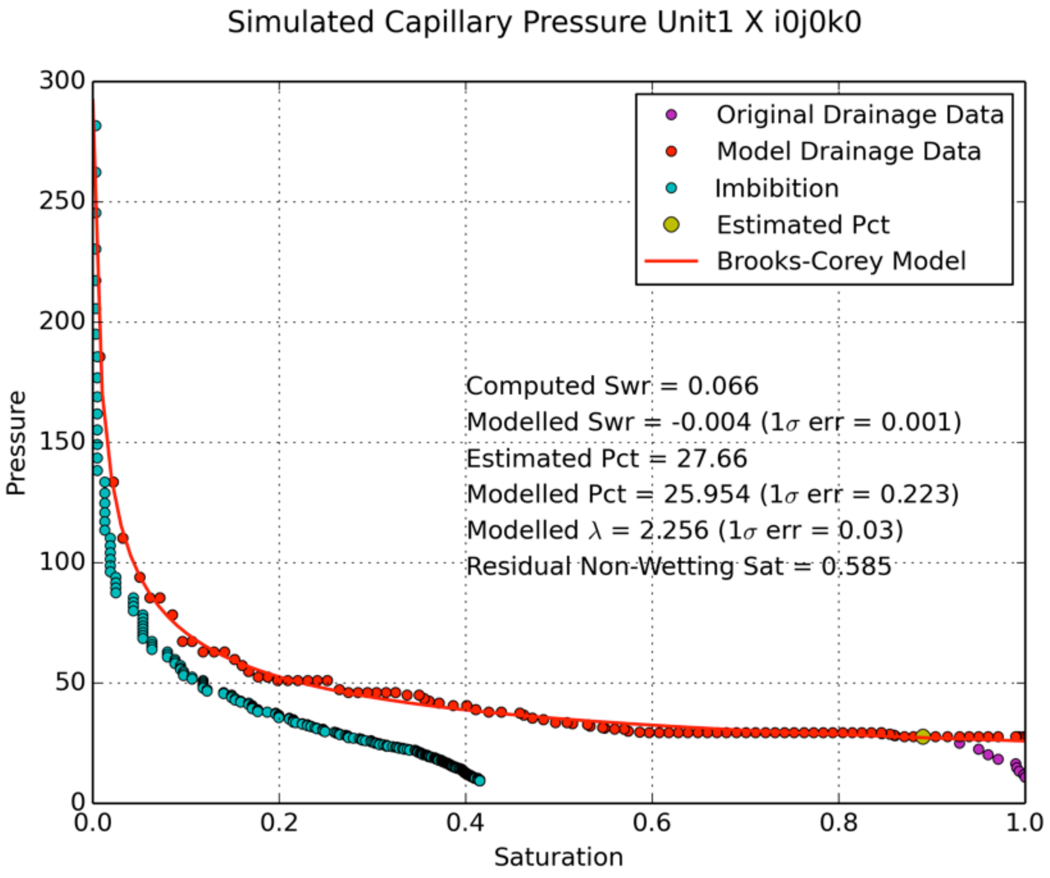

Figure 8.4: Morphology-based simulated capillary pressure data in the x-direction showing the drainage and imbibition curves and the Brooks-Corey model for drainage flow. Note once more the relatively low wetting phase saturation at the end of imbibition flow and the resulting high non-wetting phase saturation.

## 8.3 Threshold Pressure Statistical Calibration: Individual Characteristics

The threshold pressure used for correlation with predictor rock characteristics was computed from the parameterisation of the of the primary drainage pore-morphology-based capillary pressure curves using the Brooks-Corey function (eq. 8.1). These parameters are the threshold pressure ($P_{ct}$), describing the pressure required to initiate breakthrough of a non-wetting phase into the pore system, which establishes a connected cluster of fluid between the inlet and outlet faces. To understand their individual predictive ability I investigate the coefficient of determination ($R^2$) from ordinary least squares modelling between each individual rock characteristic computed from the 5, 16, and 64 μm/voxel images and $P_{ct}$ (table 8.1).

Table 8.1: The coefficient of determination ($R^2$) from ordinary least squares modelling of the logarithm of each rock characteristic (from the 5 μm/voxel, 16 μm/voxel, and 64 μm/voxel images) with the logarithms of threshold pressure ($P_{ct}$) computed from the Brooks-Corey models of the pore-morphology-based primary drainage simulations performed on the 5 μm/voxel image.

| **Characteristic** | $R^2$ **for log ($P_{ct}$) vs. log (5 μm/voxel characteristics)** | $R^2$ **for log ($P_{ct}$) vs. log (16 μm/voxel characteristics)** | $R^2$ **for log ($P_{ct}$) vs. log (64 μm/voxel characteristics)** |
|---|---|---|---|
| ***Rock Fabric*** | | | |
| Grain Size (GS) | 0.520 | 0.289 | 0.003 |
| Grain Sorting (Gsort) | 0.414 | 0.535 | 0.344 |
| Clay Fraction (CF) | 0.061 | 0.270 | 0.006 |
| ***Pore System*** | | | |
| Porosity Fraction (Po) | 0.407 | 0.429 | 0.002 |
| Open Pore Size (μm) (PS) | 0.886 | 0.723 | 0.464 |
| Open Pore Sorting (Psort) | 0.001 | 0.061 | 0.073 |
| Formation Factor (m=4) (F) | 0.217 | 0.635 | 0.700 |
| ***Minkowski Functionals*** | | | |
| Open Pore Fraction (OPF) | 0.089 | 0.343 | 0.754 |
| Surface Area (SA) | 0.039 | 0.696 | 0.852 |
| Mean Curvature (MC) | 0.105 | 0.903 | 0.841 |
| Euler Characteristic (EC) | 0.003 | 0.633 | 0.794 |

The results in table 8.1 indicate that in the 5 μm/voxel data open pore size shows the most promising ability as a predictor of $P_{ct}$ with an $R^2$ of 0.886. The threshold pressure on a capillary pressure curve is generally considered the pressure required to establish a connected cluster of non-wetting phase from the inlet to the outlet of the sample and is an indication of the largest connecting pore throat diameter. As I discuss in section 3.1 several authors have investigated and demonstrated the relationships between pore geometry and permeability and capillary pressure (Katz & Thompson, 1986; Purcell, 1949; Swanson, 1981; Thomeer, 1960). It is therefore not surprising, yet reassuring, that the 5 µm/voxel pore size characteristic correlates well with the threshold pressure. It is also important to note, however, that in this instance the pore size value is the median size computed from a volume weighted size distribution curve of the total resolved pore volume, which includes pore bodies and pore throats.

With decreasing image resolution there is an associated loss of geometric information and changes in the ability of the rock characteristics to predict $P_{ct}$. In the 16 µm/voxel image the $R^2$ value for the pore size characteristic decreases to 0.723 (table 8.1 and figure 8.5a), while in the 64 µm/voxel data it decreases further to 0.464 (table 8.1 and figure 8.5b). Compared to an $R^2$ of 0.217 in the 5 µm/voxel data, Formation factor ($F$) shows an improved correlation with $P_{ct}$ in the 16 and 64 µm/voxel images with $R^2$values of 0.635 and 0.700 respectively (table 8.1 and figure 8.5c and d). This result is similar to that of correlations between pore size and formation factor with absolute permeability (section 6.1.2). In the IR and LR images pore-grain boundaries and pore throats are represented as intermediate gray scale voxels. For the IR and LR images formation factor is gray scale sensitive computation, i.e. it incorporates gray scale values representing pore-grain boundaries and pore throats. I suggest that in this instance formation factor is able to capture some information on pore geometry based on the distribution of intermediate gray scale voxels.

A surprising result is the lack of correlation between the Minkowski functionals from the 5 µm/voxel image and $P_{ct}$ (table 8.1). Even more surprising is the significantly improved predictive abilities of surface area and the Euler characteristic in the IR and LR images. For the IR image their $R^2$ values are 0.696 and 0.633, and for the LR data $R^2$ improves to 0.852 and 0.794 respectively (table 8.1). Unlike the statistical calibration to predict absolute permeability the open pore fraction characteristic shows little correlation with $P_{ct}$ in the 16 µm/voxel data ($R^2$ = 0.343), while in the 64 µm/voxel image the correlation is somewhat stronger with $R^2$ = 0.754 (table 8.1). In particular mean curvature shows a very strong correlation with $P_{ct}$ in both the IR and LR images, with correlation coefficients of 0.903 and 0.841 for the 16 and 64 µm/voxel images respectively (table 8.1 and figure 8.5e and f). The Minkowski functional computations in the IR and LR images are applied to the fraction of resolved pore space and does not take into account voxel gray scale values from the original tomogram.

As discussed in section 6.1.2 the resolved fraction of pore space in the IR and LR images capture some physically larger component of the actual pore fraction that seems to correlate well with the number of transport pathways relevant for controlling absolute permeability. The improved correlation between open pore fraction from the LR 64 μm/voxel image and $P_{ct}$ computed from the HR 5 μm/voxel image suggests a similar behaviour in that the resolved pore fraction represents a larger component of the pore system that has some control over the threshold pressure. Taking into account the predictive ability of the mean curvature characteristic in the IR and LR images, which is computed on the resolved pore fraction, I suggest that the geometry of the open pore fraction, and specifically the curvature, either plays a role in controlling the injection threshold pressure, or, at least in the case of relatively clean sandstone, serves as an indirect measure of the pore throat characteristics. In general it might be expected that larger pore bodies be connected via larger pore throats. It could be argued that the lack of correlation between mean curvature and $P_{ct}$, both computed from the HR 5 μm/voxel image, support this hypothesis, since the HR mean curvature computation includes connecting pore throats. The IR and LR images effectively separate the pore bodies from the connecting pore throats. The geometries of the pore bodies and the pore throats are then accounted for respectively by the mean curvature and formation factor characteristics.

On the other hand the negative correlation between mean curvature and $P_{ct}$ may generate more questions than answers. In general the expectation is that smaller pore features ought to correspond to higher $P_{ct}$. In terms of mean curvature, smaller pore features produce higher mean curvature values; however, in this instance higher mean curvature values correspond to lower pressure. It follows that in this instance it may be that mean curvature simply serves as a predictor variable of the $P_{ct}$, but that there is no causality, i.e. the mean curvature of the resolved pore bodies do not have a controlling effect on $P_{ct}$. To investigate the nature of the negative correlation in more detail would require computing the correlation at a range of image resolutions to determine what happens with progressive closure of the pore throats. This amount of work falls well outside the scope and budget of this project.

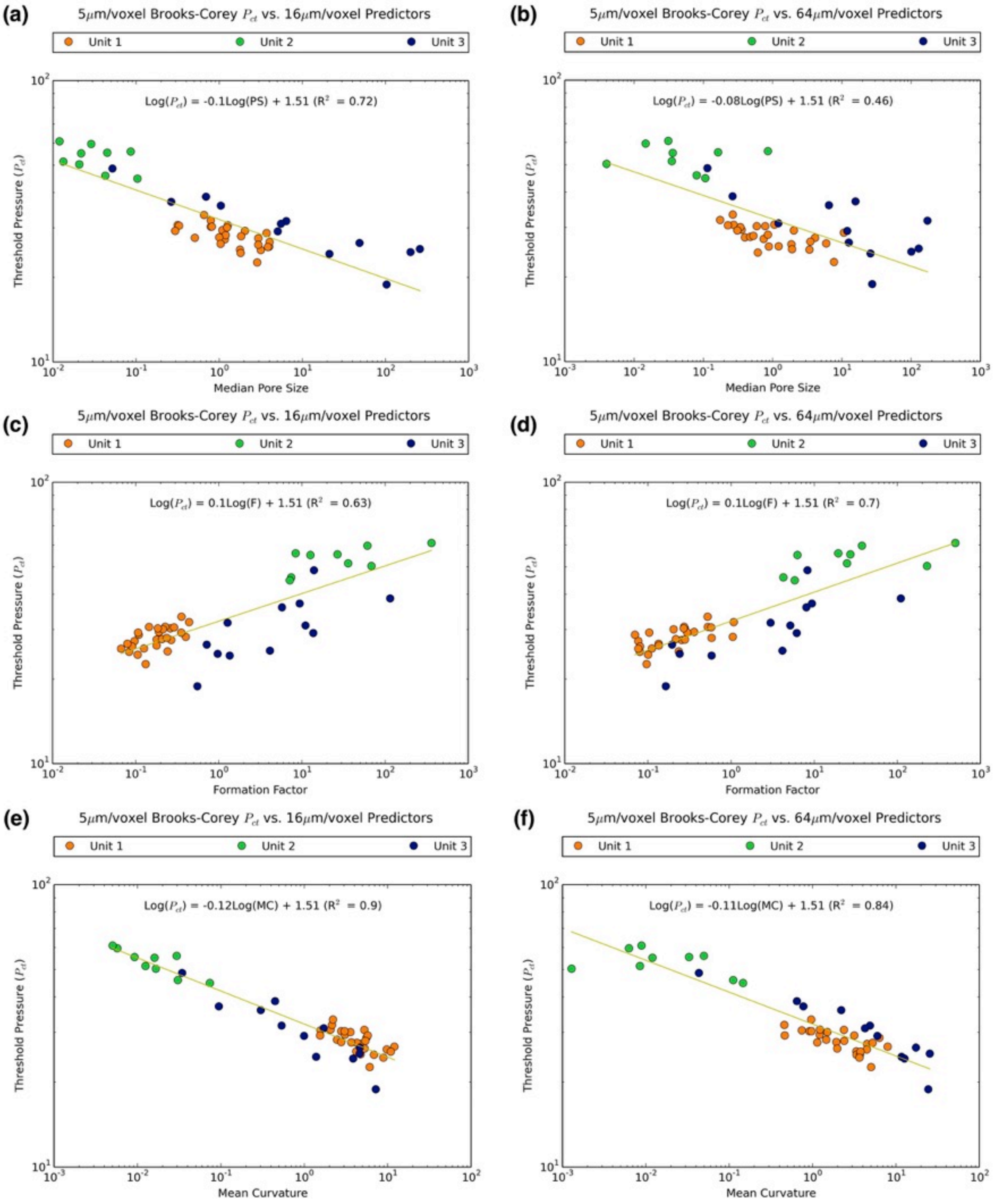

Figure 8.5: The correlations between threshold pressure (computed from the HR 5 µm/voxel image) and open pore size (a and b), formation factor (c and d), and the mean curvature Minkowski functional (e and f) calculated from the 16 and 64 µm/voxel images.

## 8.4 Threshold Pressure Statistical Calibration: Multiple Characteristics

For multiple linear modelling of threshold pressure, lambda, and trapped non-wetting phase I chose to make use of the backwards elimination procedure. Starting with the complete set of predictor characteristics in a multiple linear model, one proceeds to the next model by removing the statistically least significant characteristic according to their p-values. Sequential application of this procedure eventually arrives at a multiple linear model in which all remaining characteristics provide a statistically significant contribution (section 4.5.2).

In multiple linear regressions the coefficient of determination ($R^2$) increases with each additional predictor characteristic added to the model. Too many explanatory variables, causes the model to be overly sensitive to small changes in predictor characteristics that do not provide significant contributions to the model, i.e. noise. The implication is that an overfitted model is likely to produce unreliable predictions when applied to data outside the calibration set. A general rule of thumb states that one needs approximately ten events for every predictor variable in the model (Harrell et al., 1984; Peduzzi et al., 1996). In this instance, with 48 data points in the calibration set, it would therefore be reasonable to select a calibration model with between three and five predictor characteristics. An additional parameter that helps to select an appropriate calibration is the adjusted r-squared ($\bar{R}^2$). The adjusted r-squared (eq. 8.2) includes the number of variables ($p$) and the sample size ($n$) to modify the standard r-squared (eq. 4.2) to apply a penalty if an additional variable does not improve the model by more than what would be expected by chance.

$$\bar{R}^2 = 1 - (1 - R^2) - \frac{p}{n - p - 1} \tag{8.2}$$

In combination with the p-values for the individual characteristics and the rule of thumb suggesting the use of three to five predictors, $\bar{R}^2$ is a powerful tool in choosing the most appropriate calibration models.

Table 8.2 summarises the results for the stepwise multiple linear modelling of the logarithm of $P_{ct}$ with the logarithms of the characteristics computed from the 5, 16, and 64 μm/voxel data using the backwards elimination technique (section 4.5.2). The backwards elimination technique is distinctly different from the approach used to develop permeability models and I include the full set of models in table 8.2. It shows the characteristics included in each successive model, the characteristic with the highest p-value, and the $R^2$ and $\bar{R}^2$ for each model in the sequence. Figure 8.6 plots the $R^2$ and $\bar{R}^2$ for the series of multiple linear models constructed using the 16 μm/voxel data and shows the results of multiple linear model 10 from table 8.2. As expected $R^2$ decreases with each sequential model containing one less predictor characteristic on each occasion (figure 8.6a). Conversely $\bar{R}^2$ increases as predictor characteristics are removed for each sequential model reaching a maximum at model 7 with a value of 0.94, which contains open pore fraction, pore size, mean curvature, clay fraction, and porosity (with porosity as the least significant predictor with a p-value of 0.08). $\bar{R}^2$ increases because there are fewer predictor characteristics in each successive model resulting in a lower penalty for an overfitted model. After $\bar{R}^2$ reaches its maximum it starts to decrease because the remaining characteristics explain less of the variability in the response variable. Model 10 with an r-squared of 0.937 and an adjusted r-squared of 0.934 is the first model in which all the predictors (pore size and mean curvature) are statistically significant, i.e. they have p-values smaller than 0.05. It is interesting to note that even though a characteristic may be classified as insignificant according to its p-value, which is a good statistical measure to help guide model development and selection, that characteristic may still describe some portion of the variance in the response variable. Evidence of this effect is clearly visible in models 7 to 10, which include non-significant characteristics, yet the adjusted r-squared increases with the addition of those insignificant variables from model 10 to model 7. Given the negligible difference in the coefficient of determination between model 7 and 10, and the fact that model 10 contains all significant characteristics, model 10, with pore size and mean curvature as predictors, is chosen here as the calibration model for $P_{ct}$ using the 16 μm/voxel data (figure 8.6b). This result suggests that there is likely enough geometric information in the 16 μm/voxel image for purely geometric characteristics to adequately describe the variance in threshold pressure. The residuals for model 10 (the difference between the observed and predicted pressure values plotted against predicted $P_{ct}$) shows no observable bias in the data.

Table 8.2: The R-squared ($R^2$) and adjusted R-squared ($\bar{R}^2$) results from backwards elimination stepwise multiple linear modelling of the logarithm of $P_{ct}$ with the logarithms of the characteristics computed from the 5, 16, and 64 µm/voxel images.

| | **5um/voxel Characteristics** | | | **16um/voxel Characteristics** | | | **64um/voxel Characteristics** | | |
|---|---|---|---|---|---|---|---|---|---|
| **Model #** | **Multiple Model (Least Sig. Char: P-val)** | **$R^2$** | **Adj. $R^2$** | **Multiple Model (Least Sig. Char: P-val)** | **$R^2$** | **Adj. $R^2$** | **Multiple Model (Least Sig. Char: P-val)** | **$R^2$** | **Adj. $R^2$** |
| 1 | OPF, PS, Psort, GS, Po, F, SA, MC, EC, CF, GSort (GSort: 0.875) | 0.942 | 0.924 | OPF, PS, Psort, GS, P, F, SA, MC, EC, CF, GSort (SA: 0.987) | 0.949 | 0.934 | OPF, PS, Psort, GS, P, F, SA, MC, EC, CF, GSort (Psort: 0.836) | 0.948 | 0.932 |
| 2 | OPF, PS, Psort, GS, Po, F, SA, MC, EC, CF (CF: 0.451) | 0.942 | 0.926 | OPF, PS, Psort, GS, P, F, MC, EC, CF, GSort (F: 0.963) | 0.949 | 0.936 | OPF, PS, GS, P, F, SA, MC, EC, CF, GSort (MC: 0.842) | 0.948 | 0.933 |
| 3 | OPF, PS, Psort, GS, Po, F, SA, MC, EC (GS: 0.502) | 0.941 | 0.927 | OPF, PS, Psort, GS, P, MC, EC, CF, GSort (EC: 0.916) | 0.949 | 0.937 | OPF, PS, GS, P, F, SA, EC, CF, GSort (P: 0.679) | 0.948 | 0.935 |
| 4 | OPF, PS, Psort, Po, F, SA, MC, EC (SA: 0.075) | 0.94 | 0.928 | OPF, PS, Psort, GS, P, MC, CF, GSort (GSort: 0.762) | 0.949 | 0.939 | OPF, PS, GS, F, SA, EC, CF, GSort (EC: 0.748) | 0.947 | 0.936 |
| 5 | OPF, PS, Psort, Po, F, MC, EC (P: 0.167) | 0.935 | 0.923 | OPF, PS, Psort, GS, P, MC, CF (GS: 0.653) | 0.949 | 0.94 | OPF, PS, GS, F, SA, CF, GSort (GS: 0.681) | 0.947 | 0.938 |
| 6 | OPF, PS, Psort, F, MC, EC (EC: 0.254) | 0.932 | 0.922 | OPF, PS, Psort, P, MC, CF (Psort: 0.415) | 0.949 | 0.941 | OPF, PS, F, SA, CF, GSort (SA: 0.35) | 0.947 | 0.939 |
| 7 | OPF, PS, Psort, F, MC (Psort: 0.086) | 0.929 | 0.921 | OPF, PS, P, MC, CF (P: 0.08) | 0.948 | 0.942 | OPF, PS, F, CF, GSort (GSort: 0.19) | 0.946 | 0.939 |
| 8 | OPF, PS, F, MC (MC: 0.264) | 0.924 | 0.917 | OPF, PS, MC, CF (OPF: 0.087) | 0.944 | 0.939 | OPF, PS, F, CF (PS: 0.12) | 0.943 | 0.938 |
| 9 | OPF, PS, F (OPF: 0.004) | 0.922 | 0.917 | PS, MC, CF (CF: 0.137) | 0.94 | 0.936 | OPF, F, CF (OPF: 0.001) | 0.94 | 0.936 |
| 10 | PS, F (F: 0.004) | 0.905 | 0.901 | PS, MC (PS: 0.0) | 0.937 | 0.934 | F, CF (CF: 0.0) | 0.923 | 0.919 |
| 11 | PS (PS: 0.0) | 0.886 | 0.884 | MC (MC: 0.0) | 0.903 | 0.901 | F (F: 0.0) | 0.7 | 0.694 |

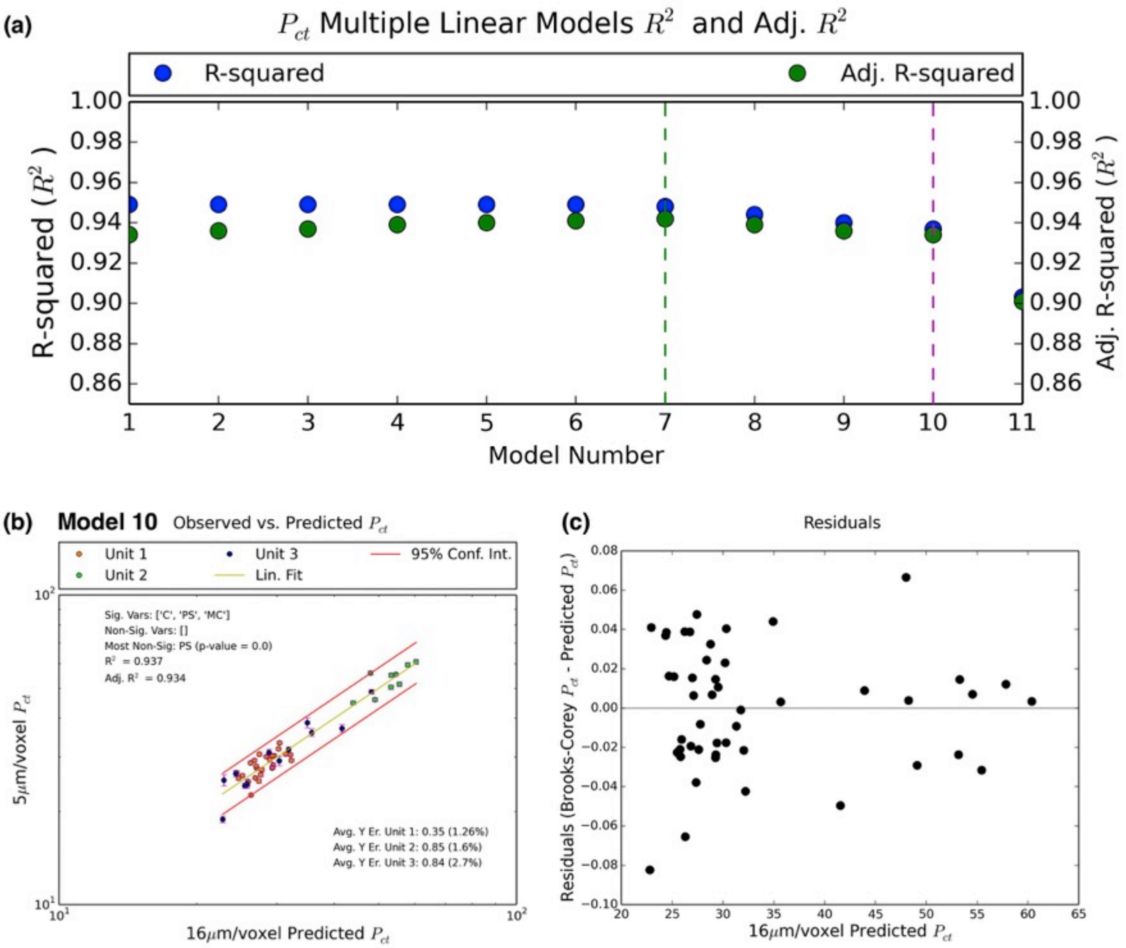

Figure 8.6: The R-squared and adjusted R-squared of multiple linear models of threshold pressure computed from the 5 μm/voxel image using sequentially fewer predictor characteristics calculated from the 16 μm/voxel image. Model 1 contains all eleven characteristics, while model 11 contains only one predictor (a). The vertical green and magenta stippled lines indicate respectively the models with the highest adjusted r-squared and with all significant characteristics (table 8.2). The computed threshold pressure plotted against the predicted pressure calculated with model 10 containing pore size and mean curvature as predictor characteristics (b). The residuals for model 10 plotted against the predicted threshold pressure values have no apparent systematic bias apart from an overabundance of data points towards lower pressure values (c).

Figure 8.7 plots the $R^2$ and $\bar{R}^2$ for the series of multiple linear models constructed using the 64 μm/voxel data and shows the results of multiple linear model 9 from table 8.2 above. The backwards elimination of characteristics results in a maximum adjusted R-squared of 0.939 at model 6 (note that table 8.2 reports that model 7 also has an adjusted r-squared of 0.939). The first model in which all the characteristics are significant according to their p-values is model 9 with open pore fraction, formation factor, and clay fraction and predictor characteristics (figures 8.7a and b). In a result similar to the modelling of absolute permeability using the LR data it would appear that the open pore fraction characteristic is able to capture some larger scale portion of the actual pore system that partly controls the threshold pressure. The range of resolutions at which open pore fraction correlates with $P_{ct}$ is likely to depend on the dominant pore length scales in the sample in question. The open pore fraction characteristic for a sample with a smaller (or larger) length scale pore system, imaged at the same 64 μm/voxel, may not contribute as significantly to a model of threshold pressure. As with the 16 μm/voxel data a plot of the residuals (figure 8.7c) shows a slight bias towards the lower threshold pressure values. This bias in the distribution of the data points is likely to be sampling effect as a function of the range of pressures represented in the calibration volume. This, along with the question of length scale dependence, remains a topic for further investigation.

As with the modelling of absolute permeability, formation factor, used here in a manner that incorporates the intermediate gray scale values, again appears to capture some geometric information about the pore system in regions where the image resolution is insufficient to accurately capture its geometry. A surprising inclusion in model 9 is that of the clay fraction characteristic, which is computed as a function of the intermediate gray scale voxels (section 4.4.4) and, in the LR 64 μm/voxel image, is not a true measure of the clay fraction in the sample. Instead it represents the sum of those voxels depicting actual clay phase and some fraction of those voxels depicting the boundaries between the grain and pore phases. In the LR image of this relatively clean sandstone sample the proportion of intermediate gray scale voxels representing grain-pore boundaries is likely to be much greater than those from actual clay mineral phases. Additionally, the open pore fraction and formation factor characteristics both take into account the fraction of resolved pore space, whereas clay fraction incorporates the unresolved portion of the pore system. I suggest that, like the formation factor, the clay fraction characteristic is able to capture some additional information on the pore system that controls the distribution of wetting and non-wetting phases and the entry threshold pressure.

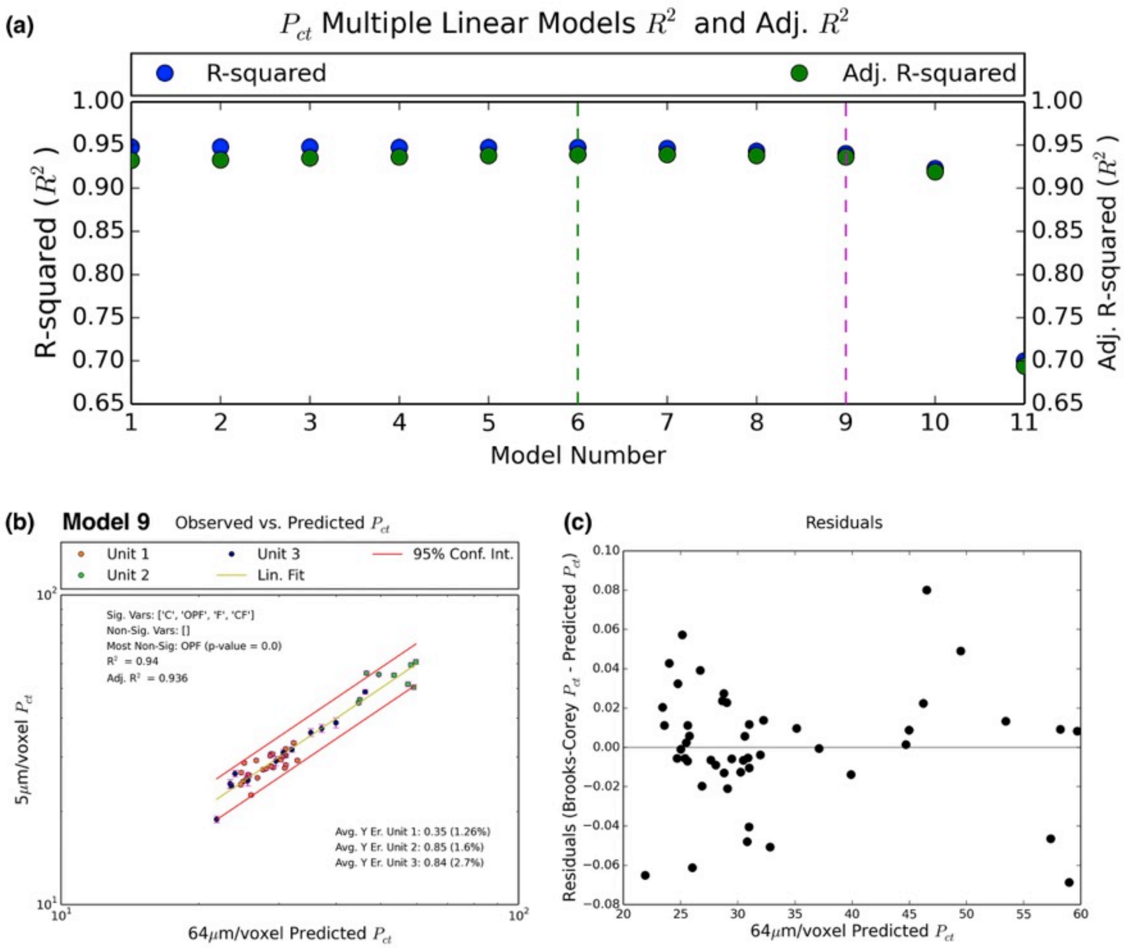

Figure 8.7: The R-squared and adjusted R-squared of multiple linear models of threshold pressure computed from the 5 μm/voxel image using sequentially fewer predictor characteristics calculated from the 64 μm/voxel data. Model 1 contains all eleven characteristics, while model 11 contains only one predictor (a). The vertical green and magenta stippled lines indicate respectively the models with the highest adjusted R-squared and with all significant characteristics (table 8.2). The computed threshold pressure plotted against the predicted pressure calculated with model 9 containing open pore fraction, formation factor, and clay fraction as predictor characteristics (b). The residuals for model 9 plotted against the predicted threshold pressure values have no apparent systematic bias apart from an overabundance of data points towards lower pressure values (c).

With the threshold pressure calibration models selected for the 16 and 64 μm/voxel images of the region of overlap, figure 8.8 compares the predicted values from the IR and LR data. The 1:1 $R^2$ provides an encouraging result indicating that there is 96% agreement between the predicted threshold pressure values from the 16 and 64 μm/voxel data for the 8mm overlap region used for statistical calibration. This result emphasises the ability of gray scale data in low-resolution images to capture important information pertaining to pore-geometry, which has some control over the threshold pressure as derived from Brooks-Corey models of morphology-based drainage flow simulations.

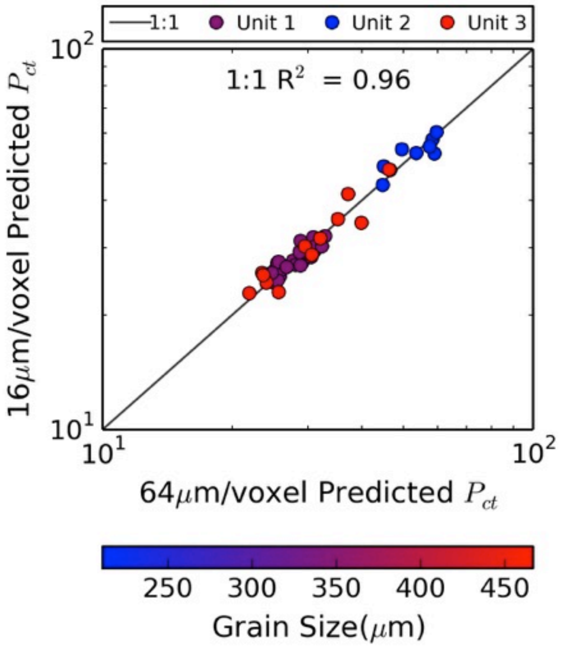

Figure 8.8: Comparing the predicted threshold pressure from the 16 and 64 µm/voxel calibration data for the 8 mm sub-plug.

## 8.5 Lambda and Residual Non-Wetting Phase Saturation

Here I briefly show the results of statistical modelling of lambda ($\lambda$) and residual non-wetting phase saturation ($S_{or}$). Figure 8.9a plots the reference lambda parameters derived from the HR 5 µm/voxel image against predicted lambda using a multiple linear model containing formation factor, mean curvature, and clay fraction from the IR 16 µm/voxel data. Figure 8.9b shows the correlation between lambda and predictors from the LR 64 µm/voxel image, which includes open pore fraction and mean curvature. The correlation results of lambda are not as convincing as the results for threshold pressure. The correlation coefficients are 0.62 and 0.48 using predictors from the IR and LR data respectively. A low $R^2$ is not necessarily grounds for declaring a model as bad, but it means that the predictors may not explain enough variance in the response variable to make useful and reliable predictions.

Calibration models of residual non-wetting phase saturation (1 – wetting phase saturation at the end of imbibition flow) using predictors from the 16 and 64 µm/voxel images (figure 8.10a and b) have correlation coefficients of 0.67 and 0.76 respectively, with predictors in the form of the Euler characteristic and clay fraction for the 16 µm/voxel data and porosity and formation factor for the 64 µm/voxel image.

The models presented in figures 8.9 and 8.10 all show a roughly linear trend between the logarithms of the response variable and the predicted values, however, it is clear that these models will not be able to produce reliable predictions results, especially considering the scale of the y-axis and the range and scatter over which the predicted values occur. These results may be interpreted in several ways. Either the results suggest that the morphology-based capillary pressure simulations are not able to produce accurate estimates of the modelled parameters, or that the predictor characteristics do not contain the relevant information to accurately predict those parameters. I suggest that both of these explanations are valid. Because of the limitations to morphology-based simulations explained in section 4.5.1 estimates of lambda from the capillary pressure curve are not accurate; therefore, resulting in poor correlations. In the case of correlations with residual non-wetting phase saturation I refer the reader to chapter 10 where I present data collected using network model-based capillary pressure simulations, which are generally considered more accurate. In support of the poor correlations in figure 8.10, in chapter 10 I provide further evidence that the predictor characteristics may not have the relevant information to make accurate predictions of residual non-wetting phase saturation.

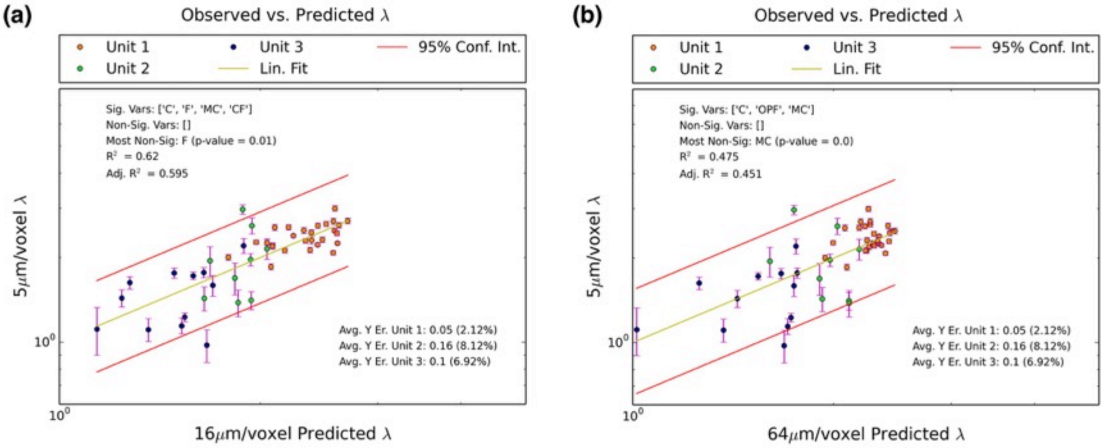

Figure 8.9: The computed lambda ($\lambda$) from the HR 5 µm/voxel image plotted against the predicted $\lambda$ using predictors from the 16 (a) and 64 (b) µm/voxel data.

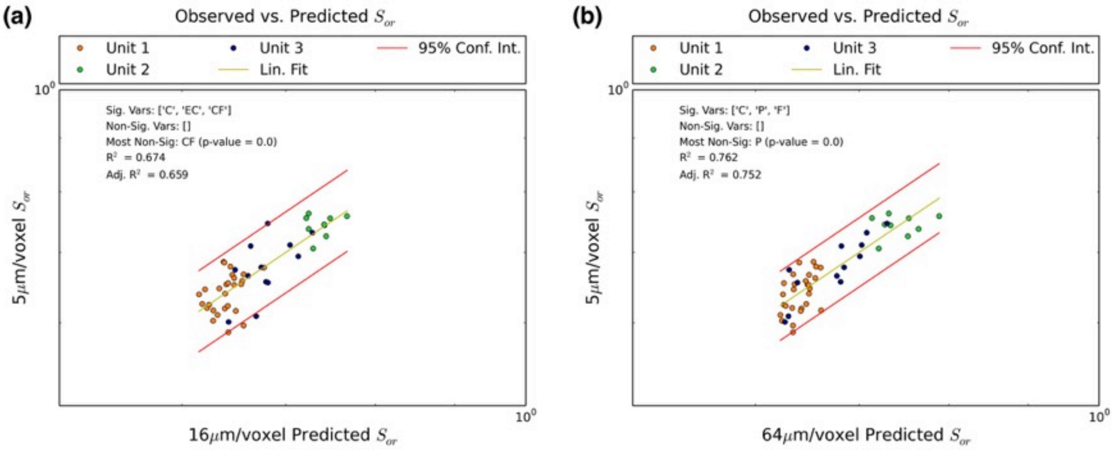

Figure 8.10: The residual non-wetting phase saturation ($S_{or}$) computed from the HR 5 μm/voxel image plotted against the predicted $S_{or}$ using predictors from the 16 (a) and 64 (b) μm/voxel data.

# 9 Capillary Pressure Results and Discussion: Sample 2

As for absolute permeability here I investigate a second sample with a similar character to that of sample 1. The 25 mm diameter 100 mm tall core plug of sample 2 was collected at 1217.32 m (sample 1 was collected at 1195.39 m). I follow the same procedure as from sample 1, i.e. perform a unitisation procedure to identify distinct regions, compute capillary pressure curves using a pore-morphology-based simulation method, model the curves using the Brooks-Corey function (eq. 4.1) to determine the threshold pressure for each sub-volume, and compute statistical correlations between the predictor characteristics from the overlapping IR (16 μm/voxel) and LR images (61 μm/voxel) with the modelled threshold pressure using the backwards elimination procedure.

Chapter 7 provides the results for the statistical calibration of absolute permeability for sample 2 and highlights that the HR 5 μm/voxel image of the sample 2 sub-plug was collected using a region of interest scan, which resulted in complications for the accurate modelling of absolute permeability. Because of the low signal to noise ratio in a region of interest scan the data I present in chapter 7 suggest that the pore system, and, more specifically, the connecting pore throats are not accurately depicted in a region of interest scan. Additionally the segmentation step of an image with a low signal to noise ratio produces isolated clusters of intermediate gray scale voxels in the within what should be open pore phase. The data in chapter 7 show that the combined effects of these images artefacts impact the numerical permeability computation and therefore the statistical calibration and prediction stages of the procedure. For absolute permeability I was able to correct for this effect by making digital adjustments to the HR image, which involved making of the micro-porosity segmentation method (see section 4.2) to depict the intermediate gray scale voxels on a linear scale between 1 and 100. By setting the first 26 phases on this linear scale to permit fluid flow (essentially converting those voxels to pore phase) I was able to remove the effect of some of the isolated clusters and improve the permeability calibration, bearing in mind that this procedure has some unavoidable effects on areas of the image that represent actual clay phase as intermediate gray scale voxels. The first 26 phases were chosen because in 3D images the centre voxel in a cluster of 27 voxels (3 x 3 x 3 voxels) is surrounded by 26 voxels. By setting the first 26 phases on the linear gray scale to permit fluid flow one essentially allows the 26 voxels surrounding an actual pore voxel to also allow fluid flow.

For the threshold pressure correlations in sample 2 I make use of the same modified image as used for permeability correlations in chapter 7. Given that several authors have demonstrated the use of capillary pressure curves and the concept of the critical threshold pressure to predict permeability (Katz & Thompson, 1986; Swanson, 1981; Thomeer, 1960), and the fact that sample 2 produces good correlation between the predictor variables and permeability, the expectation is that statistical correlations between the predictor characteristics and the modelled threshold pressure values would be similarly good. Figure 9.1 shows the results of the backwards elimination statistical modelling procedure by plotting the R-squared and adjusted R-squared statistics for each successive model, each with one fewer predictor characteristic, for the IR 16 μm/voxel data. Noticeably the coefficient of determination is considerably lower compared to the results of sample 1. In a similar result to that of sample 1 there is not a large difference between the R-squared and adjusted R-squared for model 1 (containing all predictors) and model 9, the first model where all the included characteristics are considered significant according to their p-values, indicating that only a few characteristics describe the bulk of the variance in threshold pressure. Table 9.1 provides a summary of the series of multiple linear models for both the 16 and 64 μm/voxel data. Surprisingly the formation factor characteristic, which actively takes into account the image gray scale data, is deemed insignificant in model 5 and for the IR 16 μm/voxel image the statistically significant characteristics in model 9 are porosity, pore sorting, and grain sorting (table 9.1 and figure 9.2). The 61 μm/voxel data tell a slightly different story mainly in terms of the characteristics that contribute to the first model with all-significant characteristics, i.e. model 8 with open pore fraction, formation factor, mean curvature, and clay fraction.

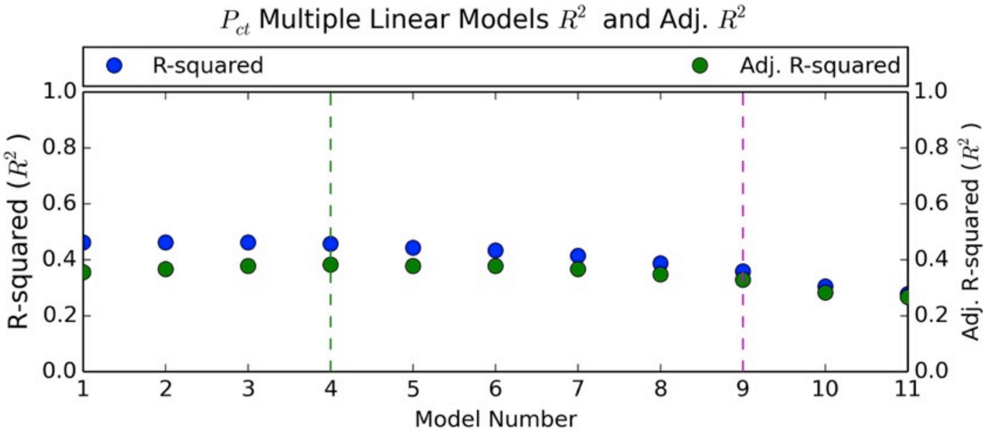

Figure 9.1: The R-squared and adjusted R-squared of multiple linear models of threshold pressure computed from the 5 μm/voxel image using sequentially fewer predictor characteristics calculated from the 16 μm/voxel data. Model 1 contains all eleven characteristics, while model 11 contains only one predictor.

Table 9.1: The R-squared ($R^2$) and adjusted R-squared ($\bar{R}^2$) results from backwards elimination stepwise multiple linear modelling of the logarithm of $P_{ct}$ with the logarithms of the characteristics computed from the 16 and 61 μm/voxel images.

| | **16um/voxel Characteristics** | | | **61um/voxel Characteristics** | | |
|---|---|---|---|---|---|---|
| **Model #** | **Multiple Model (Least Sig. Char: P-val)** | **R²** | **Adj. R²** | **Multiple Model (Least Sig. Char: P-val)** | **R²** | **Adj. R²** |
| 1 | OPF, PS, Psort, GS, Po, F, SA, MC, EC, CF, GSort (SA: 0.908) | 0.462 | 0.355 | OPF, PS, Psort, GS, Po, F, SA, MC, EC, CF, GSort (PS: 0.709) | 0.504 | 0.405 |
| 2 | OPF, PS, Psort, GS, Po, F, MC, EC, CF, GSort (PS: 0.881) | 0.462 | 0.366 | OPF, Psort, GS, Po, F, SA, MC, EC, CF, GSort (GS: 0.366) | 0.503 | 0.414 |
| 3 | OPF, Psort, GS, Po, F, MC, EC, CF, GSort (CF: 0.443) | 0.462 | 0.377 | OPF, Psort, Po, F, SA, MC, EC, CF, GSort (SA: 0.226) | 0.496 | 0.416 |
| 4 | OPF, Psort, GS, Po, F, MC, EC, GSort (OPF: 0.234) | 0.457 | 0.382 | OPF, Psort, Po, F, MC, EC, CF, GSort (Psort: 0.249) | 0.482 | 0.411 |
| 5 | Psort, GS, Po, F, MC, EC, GSort (F: 0.343) | 0.443 | 0.377 | OPF, Po, F, MC, EC, CF, GSort (GSort: 0.166) | 0.47 | 0.407 |
| 6 | Psort, GS, P, MC, EC, GSort (EC: 0.161) | 0.434 | 0.378 | OPF, Po, F, MC, EC, CF (EC: 0.093) | 0.453 | 0.398 |
| 7 | Psort, GS, Po, MC, GSort (GS: 0.091) | 0.415 | 0.367 | OPF, Po, F, MC, CF (P: 0.167) | 0.426 | 0.379 |
| 8 | Psort, P, MC, GSort (MC: 0.1) | 0.387 | 0.348 | OPF, F, MC, CF (OPF: 0.04) | 0.408 | 0.369 |
| 9 | Psort, Po, GSort (GSort: 0.023) | 0.359 | 0.329 | F, MC, CF (CF: 0.165) | 0.366 | 0.335 |
| 10 | Psort, Po (Psort: 0.116) | 0.304 | 0.283 | F, MC (MC: 0.219) | 0.346 | 0.325 |
| 11 | Po (P: 0.0) | 0.277 | 0.266 | F (F: 0.0) | 0.33 | 0.32 |

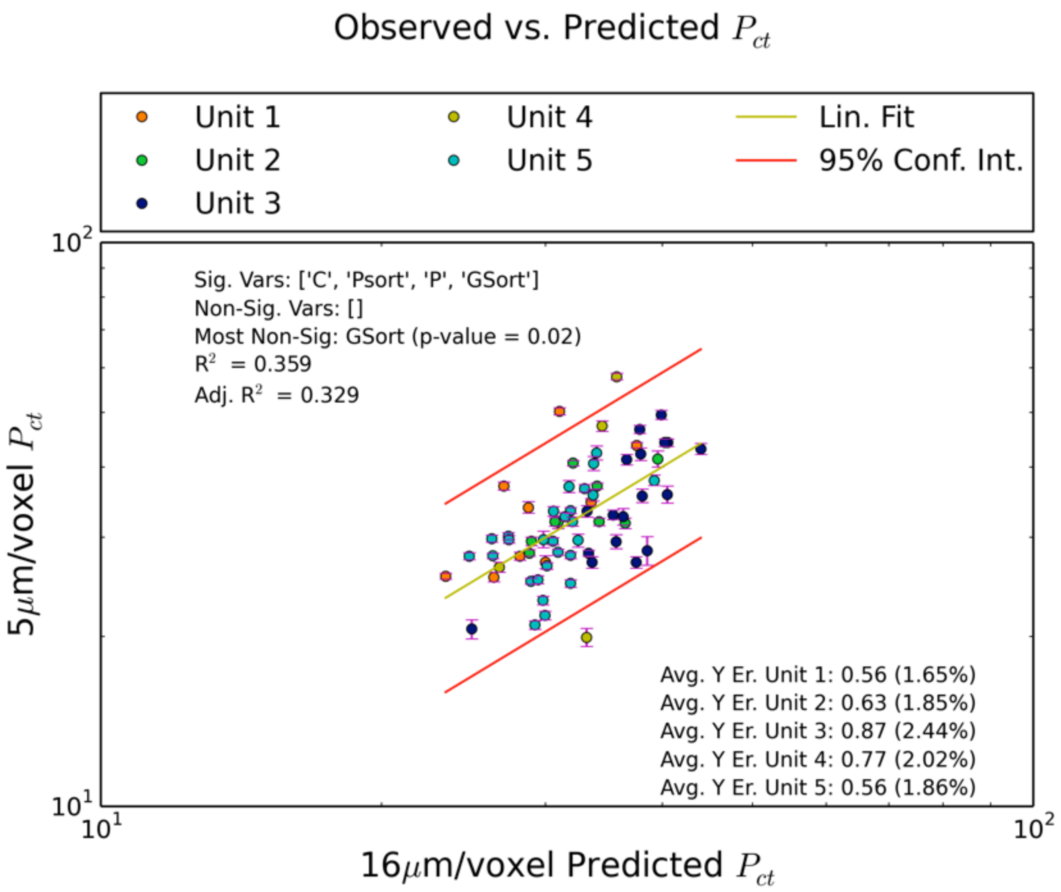

Figure 9.2: The computed threshold pressure plotted against the predicted threshold pressure calculated with model 9 containing porosity, pore sorting, and grain sorting as predictor characteristics from the IR 16 μm/voxel data.

Here I propose that the lack of good correlations between the predictor characteristics and the modelled threshold pressure is again the result of the low signal to noise ratio in the HR 5 μm/voxel region of interest scan of the sample 2 sub-plug. The low signal to noise ratio has two effects: a) the connecting pore throats are not accurately represented, and b) the pore bodies often contain isolated clusters of non-pore voxels. Both scenarios have a detrimental effect on both single- and multi-phase fluid flow simulations. To investigate the reasons for the poor correlations between predictor characteristics and threshold pressure I modified the region of interest HR 5 μm/voxel image first by increasing the number of intermediate gray scale voxels to be converted into the pore phase and second by means of an isolated clusters analysis.

The first modification to the image makes use of the same mechanism as when changing the image to improve the correlations between predictors and absolute permeability (chapter 7). Instead of selecting only the first 26 gray scale values in the micro-porosity segmentation, here the first 40 phases are converted to the pore phase (figure 9.3). In this instance 40 was chosen as an arbitrary number larger than 26 as the first step in testing the impact of incrementally increasing the number of gray scale values to permit fluid flow. The effect of this modification is that the number of voxels in the spaces that ought to represent pore bodies, and that would potentially affect the capillary pressure simulation, is reduced, and the pore throat diameters are increased. Additionally true clay phase voxels are also converted to pore phase, which has the effect of creating pore space where in reality the image should show clay phase. Essentially this procedure has a similar effect to applying a new set of segmentation parameters in which the gray scale threshold between the pore volume and solid material is increased. The second modification to the image is the direct removal of isolated clusters of non-pore voxels, the hypothesis being that isolated voxels of solid material in the pore phase have a negative impact on the capillary pressure simulations. After the HR 5 µm/voxel image was modified a new set of capillary pressure curves were computed and analysed for threshold pressure.

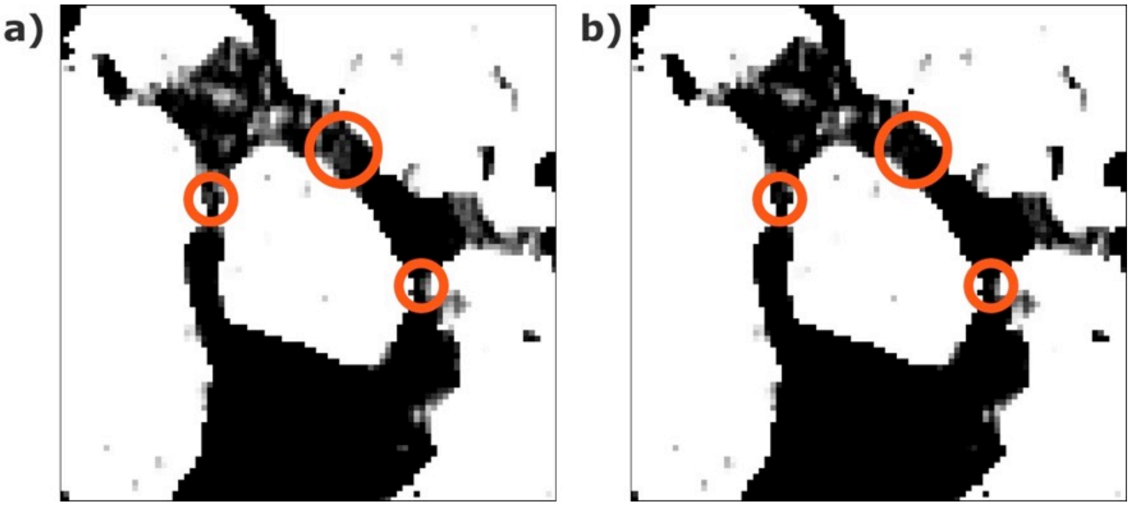

Figure 9.3: Demonstrating the subtle effect of opening the pore throats and removing and decreasing the size of some isolated clusters of voxels by increasing the number of intermediate gray scale values to convert to the pore phase. The original image in which the first 26 gray scale values were converted to pore volume (a), and the new image with the first 40 intermediate gray scale values converted to pore phase (b).

In the sequence of multiple linear models making use of the threshold pressure data computed from the modified HR 5 µm/voxel image the models with all significant predictor characteristics for the 16 and 61 µm/voxel data both contain grain size and formation factor (figure 9.4a and b). The coefficient of determination is still relatively low for both the 16 and 61 µm/voxel data compared to what was achieved for sample 1. Additionally the presence of grain size in these models is surprising, considering the lack of geometric information in the IR and LR images.

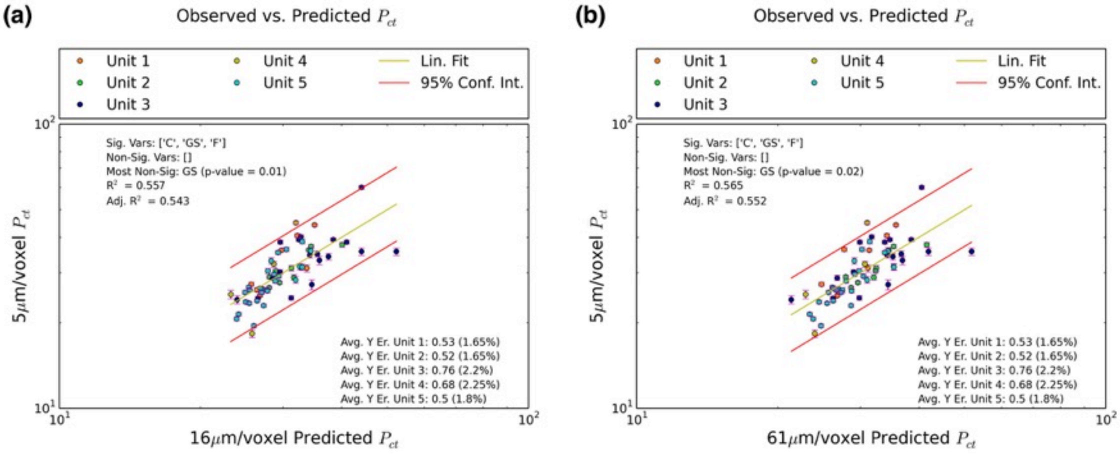

Figure 9.4: The computed threshold pressure from the modified HR 5 µm/voxel image plotted against the predicted threshold pressure calculated using model 10 with grain size and formation factor as predictor characteristics.

Modification of the HR 5 µm/voxel image of sample 2 did not result in a dramatic improvement in the correlations between predictor characteristics and the threshold pressure computed from the HR data. Here I restate the suggestion that the lack of correlation is related to the fact that the HR image does not capture the true structure of the pore system. One might argue that the correlations with permeability produced much more promising results; however, in this instance I suggest that the geometry of the pore bodies play a more important role in capillary pressure simulations, which is already sensitive to problems with image quality. With permeability in sample 2 the correlations were improved by opening the pore throats with the inclusion of the first 26 intermediate gray scale values in the pore phase. This operation also converted a small fraction of isolated clusters in the pore bodies to the pore phase. If capillary threshold pressure were purely a function of the critical length of the pore system in the form of the largest diameter sphere that can be passed through the pore structure, it would be reasonable to expect good correlations for threshold pressure using the same image as for permeability. In this instance the correlation with threshold pressure is poor, and further modification of the image by opening the pore throats and removing isolated clusters from the pore bodies did not improve the correlations significantly. The presence of non-gray scale sensitive predictors such as grain size and sorting also suggest that the gray scale information from the IR and LR images do not correspond with the HR data used for capillary pressure simulation. The HR image does not accurately represent the pore structure and the location of grain and clay mineral phases, while the IR and LR gray scale data represent actual features that the simulations on the HR data does not take into account. The only way of properly testing this hypothesis is by drilling a physical sub-plug and collecting a high quality HR image, which was outside the budget and time constraints for this project.

# 10 Capillary Pressure Results from Network Models

In this chapter I document and discuss the results from network modelling capillary pressure simulations and multiple linear modelling of threshold pressure ($P_{ct}$), lambda ($\lambda$), and residual non-wetting phase saturation ($S_{or}$). The objective is to explore the extent to which network modelling data can be used for statistical calibration and prediction of these parameters in low-resolution images where they cannot be computed directly. The irreducible wetting phase saturation ($S_{wi}$) of network model simulations is not computed by any intelligence in the algorithm, but is controlled by the proportion of intermediate gray scale voxel and their fractions of sub-resolution porosity, therefore, similar to the morphology-based data I do not investigate correlations between $S_{wi}$ and the predictor characteristics. This work is intended as a preliminary investigation to explore some of the differences between morphology- and network model-based simulations. Because network modelling is not the main focus of this thesis I perform simulations on thirteen sub-volumes, which prevents me from drawing significant conclusions about the predictor characteristics; however, the data provide positive indications of what might be possible with larger datasets.

## 10.1 Comparing Network Model and Pore Morphology Simulations

Pore network models are commonly used for multi-phase flow simulations to better understand fluid flow in terms of capillary pressure, relative permeability, wettability, and hysteresis. Generally in 3D images of porous rock and other materials the pore phase is extracted and analysed for parameters such as coordination number (the number of throat connections with each pore body) and pore and pore throat size, which is then used to construct a ball and stick representation of the pore network, which is further used for flow simulation. I generate network models using Thermo Fisher Scientific's eCore software package and perform capillary pressure simulations on thirteen sub-volumes (four from unit 1, four from unit 2, and five from unit 3) from the HR 5 µm/voxel image of the overlap region in sample 1. The methods used here to generate the network models and to perform the capillary pressure simulations are described in detail by *Bakke and Øren* [1997] and *Oren et al.* [1998]. The sub-volumes from units 1 and 2 are $330^3$, while the sub-volumes from unit 3 are $425^3$. The pore network extractor requires cubic volumes for analysis, therefore the sub-volumes from unit 2 used for network modelling are slightly smaller in the z-direction compared to the volumes used for pore morphology-based capillary pressure simulations, which are 330 voxels in the x and y directions, and 392 in the z-direction (as determined by the unitisation procedure – section 4.3). Other than the size difference for the volumes in unit 2 the volumes used for network modelling are the same as those used for morphology-based simulations.

Figure 10.1 plots the morphology and network modelling capillary pressure simulation results for one sub-volume from each of the three units (figure 10.1a, b, and c), while figure 10.1d, e, and f directly compare the critical threshold pressure ($P_{ct}$), lambda ($\lambda$), and the residual non-wetting phase saturation computed from Brooks-Corey modelling of the network model and morphology-based simulation drainage curves. To produce the plots in figure 10.1a, b, and c I convert the pressure data from the network models, expressed in Pascal, to the same units as the morphology-based pressure data (1/pore radius) by dividing the Pascal units by the interfacial tension (set to 30 dynes/cm) and the contact angle of 10 degrees. Here the purpose of the comparison is to demonstrate that one is able to set the contact angle of the network model simulation to a non-zero value, and that the result is likely to be a more accurate representation of reality. I acknowledge that it is more appropriate to also perform a network model simulation with the contact angle set to zero, however, limitations on computational resources and time prevented those tests in this project.

The results in figure 10.1a, b, and c demonstrate that for units 1, 2 and 3 the estimated and computed threshold pressures using Brooks-Corey modelling of the network modelling simulation drainage curves are consistently higher compared to that of the morphology-based simulations. Moreover, there appears to be a general linear relationship between the network model and morphology-based threshold pressure data (figure 10.1d). As expected both the morphology and network modelling results show that unit 2 (the finest grained unit of the three) has the highest threshold pressure values, while unit 1, with intermediate grain size, has the lowest threshold pressure values. Unit 3, which is generally coarser grained, with poorer sorting and higher proportions of clay minerals, produce intermediate threshold pressure data that fall between those of units 1 and 2. A comparison of the lambda ($\lambda$) parameter estimated from Brooks-Corey modelling shows no discernable relationship between $\lambda$ derived from network modelling and morphology-based drainage simulations, except that the $\lambda$ estimates from network modelling simulation curves of sub-volumes in unit 1 are generally lower compared to the morphology-based data, and for most, though not all, sub-volumes from units 2 and 3 the network modelling-based lambda data are higher compared to the morphology based values (figure 10.1e). Additionally, lambda depends largely on the corners and crevices of the pore system, which are quite different between pore network models and the morphology-based analysis. Figure 10.1f compares the residual non-wetting phase ($S_{or}$) results and, similar to the $\lambda$ comparison, shows no clear trend in the data, except that the estimates of $S_{or}$ from the network modelling imbibition curves are considerably lower compared to the morphology-based data. This is not a surprising result considering that the morphology-based drainage simulations approach zero as the irreducible wetting phase saturation. Additionally the imbibition flow simulations cannot account for multi-phase flow phenomena such as wettability (contact angle) and therefore it cannot account for flow hysteresis, therefore the $S_{or}$ is over-estimated compared to results derived from network model simulations.

The summarised results in figure 10.1 clearly demonstrate the main advantages of network modelling over morphology-based capillary pressure simulations. A network modelling method incorporates parameters such as wettability in the form of contact angle, therefore the simulation is able to produce more realistic estimates of the residual non-wetting phase saturation (the difference between 1 and the wetting phase saturation at the end of imbibition flow) compared to morphology-based simulations, which have no method for distinguishing drainage and imbibition flow. The network model drainage curves do not approach zero like their morphology-based counterparts, therefore estimates of lambda, essentially the parameter controlling the rate at which the curve rises from the threshold pressure value to the maximum pressure at the end of drainage flow, are potentially more accurate.

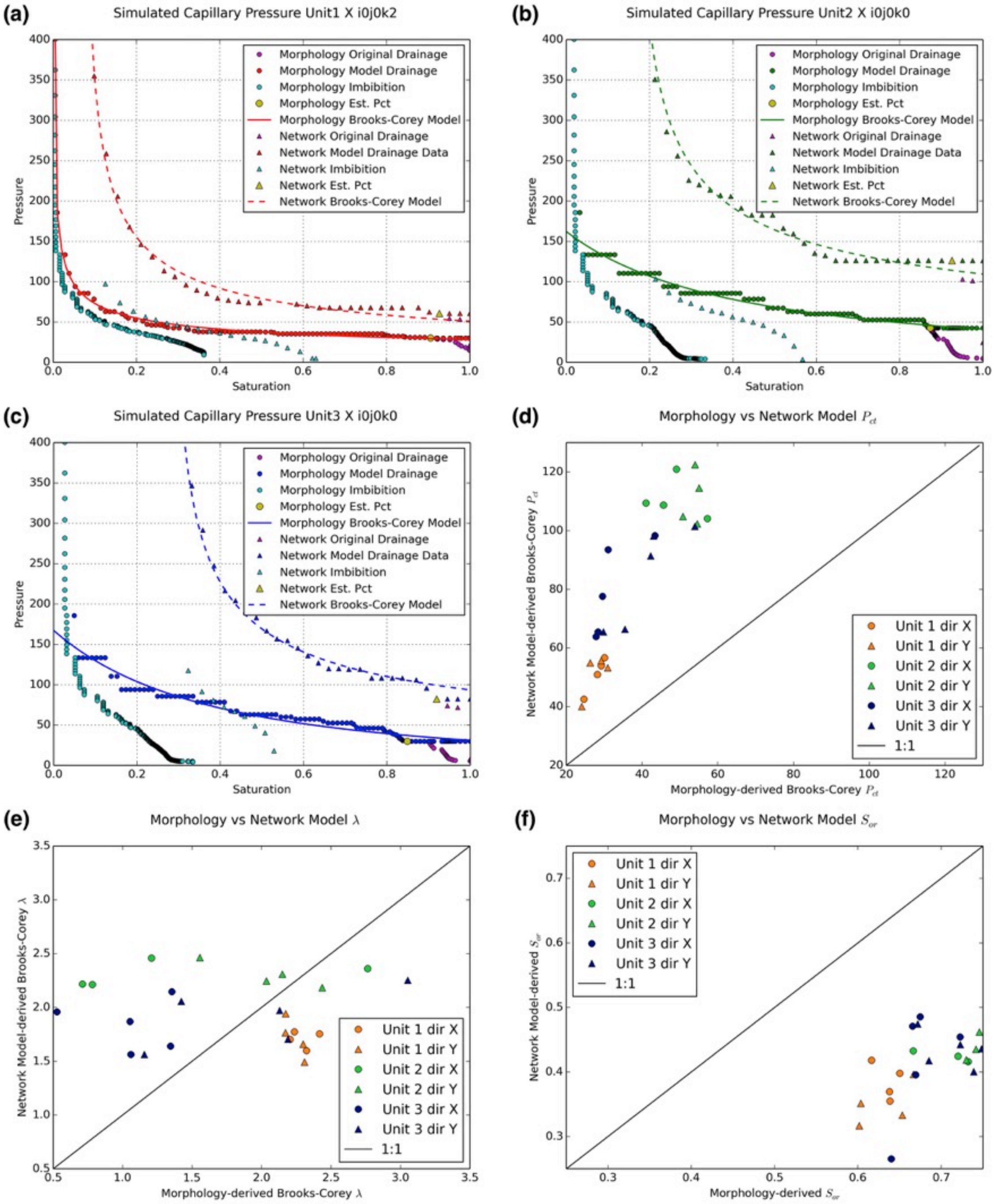

Figure 10.1: A visual comparison of x-direction network model and pore morphology-based capillary pressure simulation results of one sub-volume from units 1 (a), 2 (b), and 3 (c) in the HR 5 µm/voxel image of sample 1; diagrams comparing the threshold pressures (d) and lambda ($\lambda$) (e) parameters computed from Brooks-Corey modelling (section 8.2) of the network model and morphology-based drainage curves; and, a diagram comparing the estimated residual non-wetting phase saturation at the end of network model and morphology-based imbibition flow simulations (f).

In the early stages of investigating capillary pressure in this study I concluded that network modelling would likely provide useful data for parameters such as residual non-wetting phase saturation; however, the data I present here in figure 10.1 demonstrate that, even though there is a difference in the absolute values of threshold pressure computed from network modelling and morphology-based drainage simulations, there is a general linear relationship, therefore morphology-based simulations can provide valuable insights into the flow behaviour of heterogeneous systems such as the Precipice sandstone. Moreover, performing morphology-based capillary pressure simulations are computationally efficient and is a convenient method for generating large amounts of data in a short timeframe.

As valuable as pore network models are, it is worth considering some of its limitations. Most flow simulation methods rarely take into account dynamic effects on the pore structure as a result of fluid flow or fluid-rock interaction. It follows that contact angle and wettability in pore network model-based simulations are assumed to be constant from the beginning to the end of the simulation, whereas, in reality, the pore geometry may have changed as a result of fluid flow and fluid-rock interaction effects such as diffusion or precipitation. Additionally, pore network models do not take into account variables such as temperature and its influence on wettability. To compensate for these variables a simulation may be run several times using different parameters in an attempt to understand the potential impacts. Finally, wettability is typically set for the entire network model, while in reality wettability is different for various components of the pore network where pore-grain boundaries are defined by different minerals, e.g.: quartz, calcite, or clay.

## 10.2 Multiple Linear Statistics with Network Model-Derived Parameters

In this section I present and discuss the multiple linear modelling of the capillary pressure parameters derived from network model simulations of drainage and imbibition flow. Brooks-Corey modelling of the drainage curves produce threshold pressure, lambda, and irreducible wetting phase saturation (section 8.2), while residual non-wetting phase saturation is computed by subtracting the wetting phase saturation at the end of imbibition flow from 1. Here I make use of the same backwards elimination statistical procedure used for the morphology-based statistical model development in section 8.4 (see section 4.7.2 for a description of the backwards elimination method). I perform network modelling on a small exploratory data set of thirteen sub-volumes, therefore I choose to consider only model 10, which contains just two predictor characteristics for each response variable.

Figure 10.2 shows the multiple linear statistical modelling of threshold pressure using IR 16 µm/voxel and LR 64 µm/voxel predictor characteristics (a and b). The IR and LR models respectively contain pore size and formation factor, and formation factor and clay fraction, with $R^2$ values of 0.91 and 0.93. The results clearly demonstrate that, even with the small number of data points, a multiple linear model containing some combination of predictor characteristics is likely to describe a large proportion of the variance in the threshold pressure data. The comparative model containing just two characteristics to describe the variance of the morphology-based threshold pressure data using 16 µm/voxel characteristics also include pore size, but it lacks formation factor, which is substituted by mean curvature (table 8.2). The comparative 64 µm/voxel model contains the same characteristics (formation factor and clay fraction) as the model of network modelling threshold pressure data (table 8.2). These results demonstrate some consistency in the low-resolution characteristics that correlate with threshold pressure, regardless of the method used for its computation.

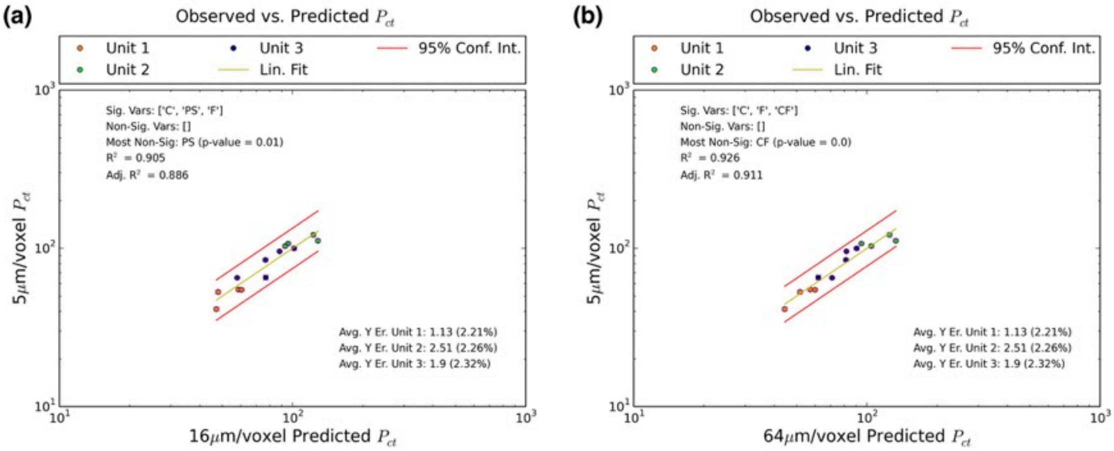

Figure 10.2: Threshold pressure computed from network model drainage curves simulated using the HR 5 µm/voxel image plotted against the predicted threshold pressure of multiple linear models using characteristics from the IR 16 µm/voxel data (a) and the LR 64 µm/voxel image (b). The 16 µm/voxel model contains pore size and formation factor, while the 64 µm/voxel model contains formation factor and clay fraction.

Figures 10.3 shows the multiple linear models of lambda using IR 16 μm/voxel and LR 64 μm/voxel predictor characteristics (a and b). Surprisingly the statistical correlations between the response parameter lambda and the IR 16 μm/voxel and LR 64 μm/voxel predictor characteristics produce encouraging results. The predictor characteristics included in the model are surface area and mean curvature for the IR data (figure 10.3a), and formation factor and clay fraction for the LR data (figure 10.3b), with coefficients of determination of 0.95 and 0.93 respectively. Threshold pressure and lambda are modelled with the same 64 μm/voxel predictor characteristics in the form of formation factor and clay fraction.

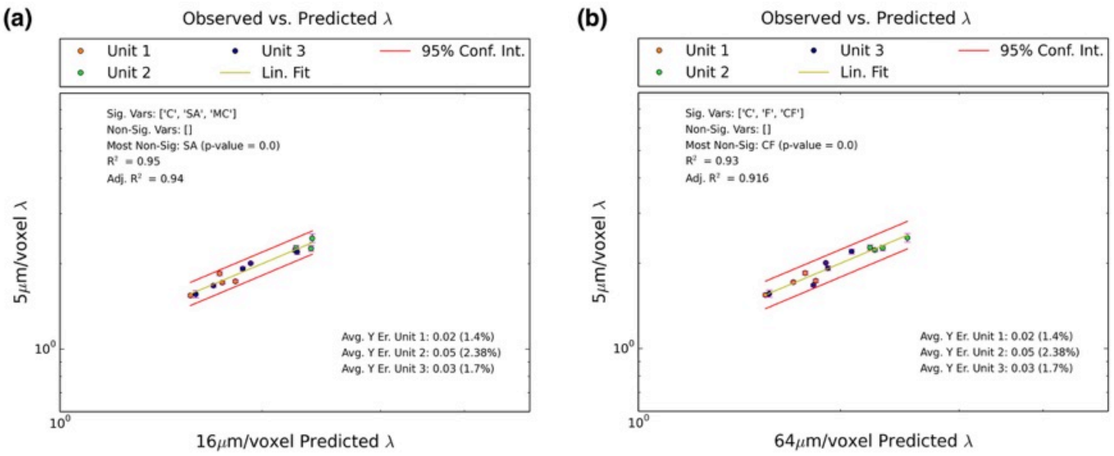

Figure 10.3: Lambda computed from network modelling drainage curves using the HR 5 μm/voxel image plotted against the predicted lambda of multiple linear models using characteristics from the IR 16 μm/voxel data (a) and the LR 64 μm/voxel image (b). The 16 μm/voxel model contains surface area and mean curvature, while the 64 μm/voxel model contains formation factor and clay fraction.

Figure 10.4 shows the multiple linear statistical modelling of $S_{or}$ using IR 16 μm/voxel and LR 64 μm/voxel predictor characteristics (a and b). The IR and LR models respectively contain open pore fraction and the Euler characteristic, and the Euler characteristic and mean curvature. In this instance the results are less encouraging compared to the modelling results of those parameters derived from the drainage curves. The coefficients of determination of the IR and LR data are 0.67 and 0.61 respectively. The model containing three characteristics from the IR 16 μm/voxel image has an $R^2$ of 0.85. It is therefore possible that with a larger number of data points and one or two more predictor characteristics, rather than just the two used in this example, one could achieve a more complete description of

$S_{or}$. Admittedly this is a somewhat speculative assessment and would require further investigation.

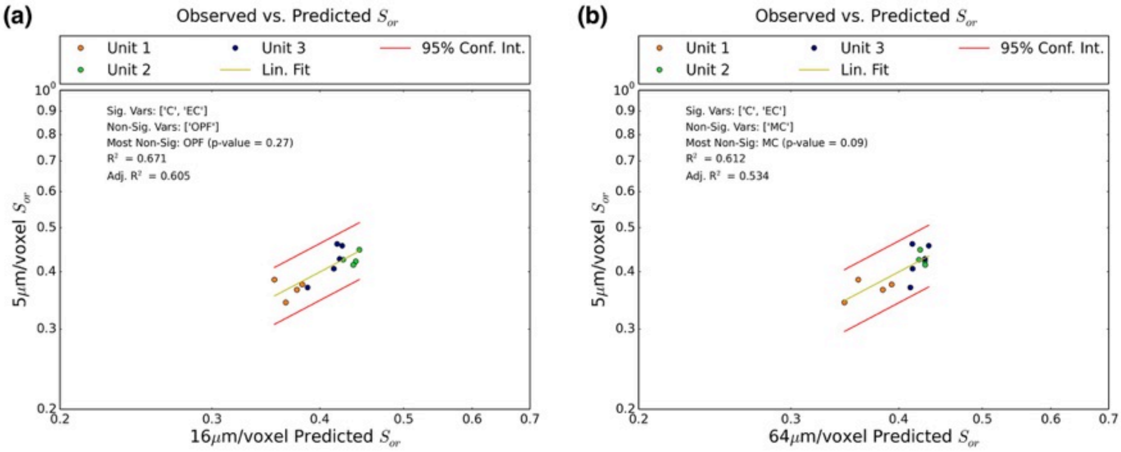

Figure 10.4: Residual non-wetting phase saturation computed from network modelling imbibition curves using the HR 5 μm/voxel image plotted against the predicted residual non-wetting phase saturation of multiple linear models using characteristics from the IR 16 μm/voxel data (a) and the LR 64 μm/voxel image (b). The 16 μm/voxel model contains open pore fraction and the Euler characteristic, while the 64 μm/voxel model contains Euler characteristic and mean curvature.

### 10.2.1 Dependence of Residual Non-Wetting Phase Saturation on Initial Wetting-Phase Saturation and Contact Angle

It is important to note that $S_{or}$ at the end of imbibition flow can be influenced by $S_{wi}$ at the beginning of imbibition flow, i.e. at the end of drainage flow, and the receding contact angle ($\theta$); therefore, changes in these parameters may produce $S_{or}$ data that show stronger correlation to the predictor variables than is shown in figure 10.4. To explore the effects of these parameters on $S_{or}$ I perform several imbibition flow simulations on the same volumes used previously by setting $S_{wi}$ to 0.1, 0.2, 0.3, and 0.4, and the receding contact angle to 20, 40, and 60. The $S_{wi}$ values equate to initial non-wetting phase saturations of 0.9, 0.8, 0.7, and 0.6. Here, a single drainage simulation is performed and purposefully terminated as close as possible to the pre-set $S_{wi}$ value; this state is then used as the starting point for imbibition flow simulation. Figure 10.5 shows the changes in $S_{or}$ as a function of $S_{wi}$ and $\theta$. Each column represents a target $S_{wi}$ value and contains the $S_{or}$ values as columns of data series for $\theta$ equal to 20, 40, and 60. The first column for

$S_{wi} = 0.1$ also contains the $S_{or}$ values for $\theta = 10$, which is the original imbibition flow simulation result used to compute the statistical models in figure 10.4. For $S_{wi} = 0.1$ figure 10.5 shows that increasing $\theta$ to 20 causes an overall decrease in $S_{or}$ for all the sub-volumes, while also increasing the range of values. A further increase in $\theta$ to 40 again decreases $S_{or}$, but limits the range of values except for one low value of ~0.125. A final increase of $\theta$ to 60 also results in lower $S_{or}$ values, but this time increases the range. This patter associated with changes in $\theta$ is repeated for $S_{wi}$ equal to 0.2, 0.3, and 0.4. Considering the effect of $S_{wi}$ the graph shows that there is a relatively small decrease in $S_{or}$ from 0.1 to 0.2 and to 0.3 for all $\theta$ values, with the largest decrease in $S_{or}$ occurring at $S_{wi}$ of 0.4. The decrease in $S_{or}$ with increasing $S_{wi}$ is largest for $\theta = 20$ and smallest for $\theta = 60$. In the context of $CO_2$ injection and storage the data from this kind of analysis is plotted as a trapping curve. In this instance because I am working with multiple units and sub-volumes in a single sample the data is complex to visualise and therefore not plotted in the conventional manner for trapping curve analysis. Trapping curves are important to understand the changes in potential capillary trapping of liquid $CO_2$ with increasing distance from the injection site, where there is less certainty of what injection pressure could be achieved. As the injection pressure drops with distance from the well-bore $S_{wi}$ increases, which, as can be seen in the simulation data of figure 10.5, causes a general decrease in $S_{or}$ (the trapped fraction of $CO_2$).

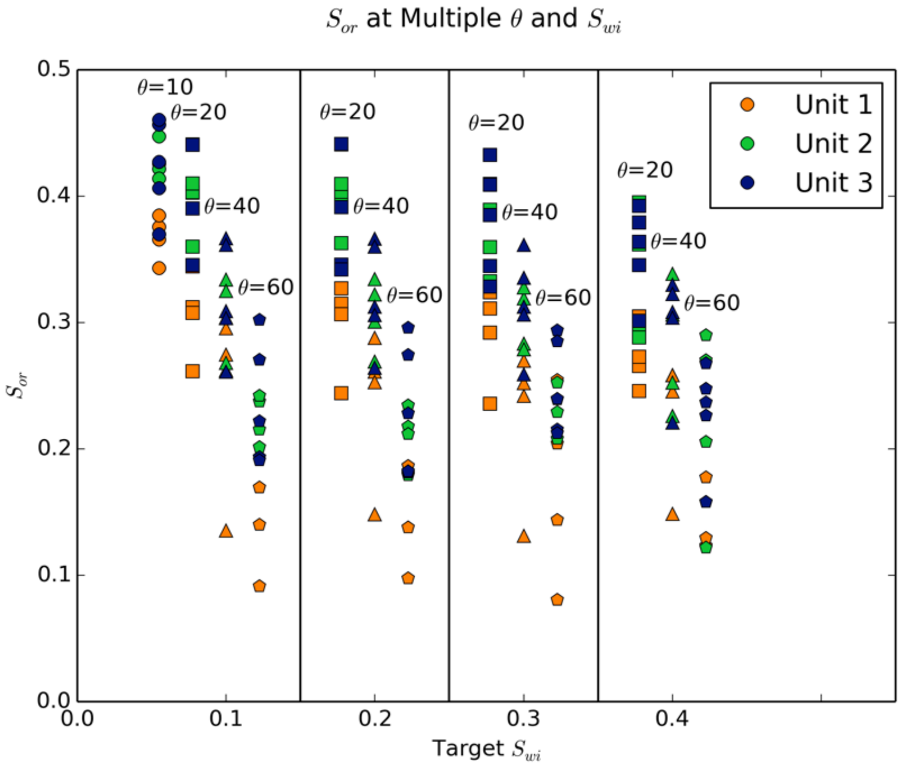

Figure 10.5: The residual non-wetting phase ($S_{or}$) plotted as a function of irreducible wetting phase saturation ($S_{wi}$) at the end of drainage flow and receding contact angle ($\theta$). The colours indicated in the legend are applicable to all marker shapes.

To check if changes in $S_{or}$ as a function of $S_{wi}$ and $\theta$ has an impact on the statistical correlations with predictor variables I run the backwards elimination statistical modelling process for each set of $S_{or}$ values. Figure 10.6 reports the coefficient of determination for each set of values. The data demonstrates that there is very little change in the amount of variance in $S_{or}$ described by the predictor characteristics as a function of changes to $S_{wi}$ and $\theta$. There is a small increase in $R^2$ compared to the correlation results using $S_{wi} = 0.1$ and $\theta = 10$ when $S_{wi}$ increases to 0.2 and $\theta$ to 20. In all other cases, except with $S_{wi} = 0.4$ and $\theta = 40$, the correlation coefficient is lower compared to the original data. In the one case where an improvement occurs it is only when for the 16 µm/voxel characteristics. With these results I suggest that $S_{wi}$ and $\theta$ are not the main drivers for relatively poor correlations between $S_{or}$ and intermediate- and low-resolution predictor characteristics.

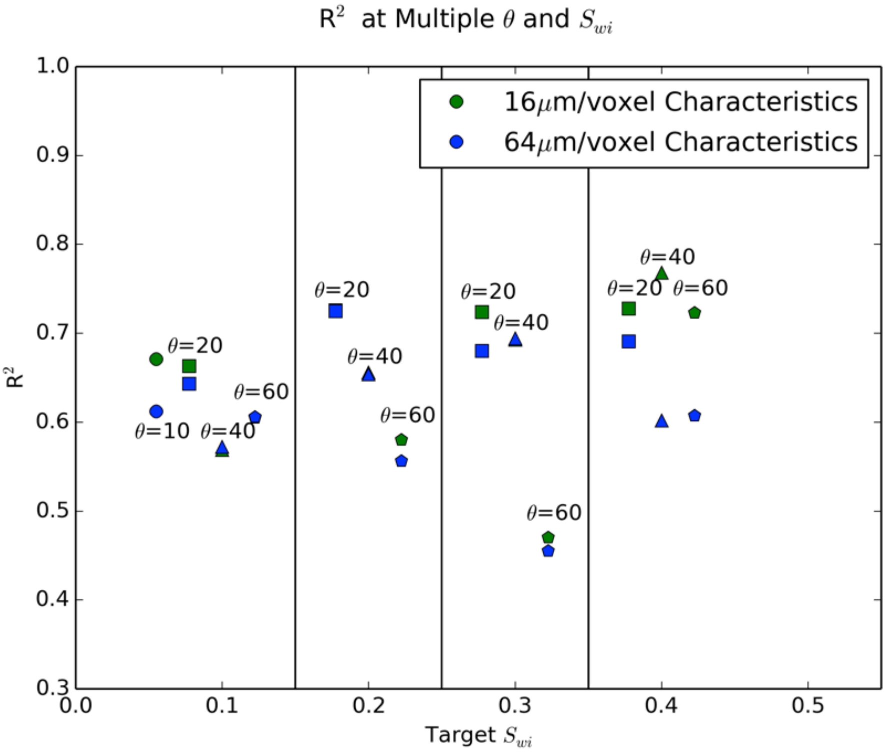

Figure 10.6: The coefficient of determination ($R^2$) of multiple linear models between $S_{or}$ values, produced as a function of changes to $S_{wi}$ and $\theta$, and the 16 and 64 µm/voxel characteristics. Owing to the relatively small dataset the $R^2$ values plotted here are for those models containing just two predictors. The colours in the legend reference all marker shapes.

The multiple linear statistical modelling results of parameters derived from network model drainage curves are mostly encouraging. Even though the dataset used here is small, especially compared to the relatively large number of predictor characteristics, the results indicate that it is possible to produce multiple linear models to describe large proportions of variance in the parameters derived from Brooks-Corey modelling of the drainage curves. As mentioned in section 10.1 even though there are differences in the threshold pressure data computed from network model and morphology-based simulations, in both cases statistical models are able to provide good descriptions of its variance. In the case of lambda network model simulations appear to produce more accurate estimates of the lambda parameter, which correlate well with predictor characteristics. Given the good statistical modelling results of threshold pressure and lambda, I suggest it could be possible, if the contact angle is known, to predict a Brooks-Corey function that describes drainage flow in IR and LR images where its direct simulation is not possible, but that imbibition may be more challenging.

# 11 Conclusions and Further Work

Computing petrophysical properties from low-resolution µCT images that cannot accurately represent the pore system is a significant and important challenge. Solving this problem would make µCT imaging of small-scale samples more applicable and useful to larger scale reservoir and aquifer modelling. Flow properties such as permeability and threshold pressure are controlled by pore system geometry and length scales. In practice large-scale images of heterogeneous systems are critical to capture formation heterogeneity at the whole core scale, however, at the time of writing this thesis µCT imaging systems cannot generate images with the desired combination of sufficient resolution and field of view. Even it were possible to collect such images, current computing infrastructure are not able to manage the large amounts of data. Instead, in large-scale images, the critical pathways that control fluid flow are typically represented as intermediate gray scale values as a result of the partial volume effect, where, at the boundaries between pores and grains, high and low gray scale values contribute in various proportions to produce some intermediate gray scale value.

In this body of work I present the fundamentals of a workflow aimed at predicting petrophysical properties where they cannot be computed directly. The two main hypotheses with which I approached this work are:

1) The classic approach to such problems applies classification methods to group repeating rock units; however, I suggest that a statistical approach may be more appropriate, and
2) Where pore throats are represented as intermediate gray scale voxels in lower resolution images, those measures that somehow make use of the image gray scale values have the potential to correlate with fluid flow properties

Results clearly showed that a statistical approach is more appropriate since the range of rock characteristics with which a classification of units or laminations could be performed exists on a continuum with no clear boundaries between repeating units. The statistical approach relies on multi-scale imaging to compute absolute permeability and parameterised capillary pressure curves on high-resolution images of small-scale samples that cover a range of grain sizes and pore length scales. Furthermore I compute fundamental rock characteristics from lower resolution images that are digitally aligned to correspond with the high-resolution data. I make use of multiple linear ordinary least squares regression analyses between the high-resolution petrophysical properties and the lower resolution rock characteristics to generate statistical models with which to predict the flow behaviour in other parts of the sample where high-resolution data are not available. Critically the low-resolution characteristics include formation factor, which, in digital rock physics can be tuned to take into account image gray scale values by performing a soft-thresholding image segmentation technique. The workflow produces a 3D property map for large-scale core images, which is ideally suited for property upscaling.

The results on two laminated sandstone samples demonstrate that multiple linear regressions can successfully model permeability and threshold pressure. The statistical model for permeability using the intermediate-resolution data includes pore size, open pore fraction, and formation factor, while the model using the low-resolution data only includes open pore fraction and formation factor. It can be inferred from the results that the open pore fraction and formation factor characteristics appear to capture critical aspects of the pore system when computed on images with relatively low resolution. The voxel sizes of 64 and 61 μm/voxel used in samples 1 and 2 are far lower than that required to capture the full pore system in black-and-white, making open pore fraction a surprising inclusion as a predictor characteristic. Open pore fraction is, however, no longer a measure of porosity in these lower-resolution images and appears to relate to the number of transport pathways critical to fluid flow. The correlation coefficient of the statistical model between permeability and open pore fraction remains relatively unchanged over a reasonable range of gray scale thresholds used for image segmentation, indicating that the predictive ability of the model is to some extent independent of the segmentation parameters used to isolate the pore space. Formation factor, because of the use of gray scale information in its computation seems to incorporate some measure of pore system length scale and connectedness. At intermediate resolution pore size is still a measure of pore length scale and is deemed to contribute significantly to a statistical model of permeability.

Statistical models of threshold pressure were developed using the backwards elimination technique and contain pore size and mean curvature using the IR 16 µm/voxel data, and open pore fraction, formation factor, and clay fraction using the LR 64 µm/voxel data for sample 1. As for permeability it would appear that the IR data contain enough geometric information for purely geometric characteristics in the form of pore size and mean curvature to adequately describe the variance in threshold pressure, while using the LR data requires gray-scale sensitive characteristics like formation factor and clay fraction to capture the length scale information required to properly model threshold pressure variance. It is critical to mention the failed result of threshold pressure regression analysis in sample 2. Sample 2 was imaged as a region of interest scan, which means it has a low signal to noise ratio. The results of modelling permeability and threshold pressure in sample 2 demonstrates the importance of image quality and the associated quality of the reference computed property values, which are critical to the reliability of the predicted petrophysical data. Even though some modifications were made to correct for this effect and to produce good models of permeability, these modifications had little effect on the models of threshold pressure. I suggest the modifications to the low signal to noise ratio image of sample 2 also changed the distribution of intermediate gray scale voxels in the pore bodies, which means the lower resolution images now contain information in locations where the high-resolution image does not. I conclude that the accuracy of predictions made using the workflow presented in this thesis is highly dependent on image quality and consistency. I further recommend that additional testing be conducted using a physically cored sample as a comparison to the results from samples 1 and 2 reported in this thesis. These new data will give greater insight into the impact and usability of high-resolution region of interest scans for statistical calibrations and predictions.

In terms of the overall body of work I emphasise that further research is required to assess the general applicability of the results and workflow presented in this thesis. In more complex rocks with more varied clay mineral composition and where the pore system connects in a different way, it is possible that the characteristics used in this study lose some of their value as property predictors. For example, intermediate gray scale values representing pore throats and those representing clay minerals could easily be confounded, potentially compromising the statistical models. In the workflow presented here, these cases would be identified by poor cross-scale correlations during the statistics calibration stage.

Additional work should also test the degree to which the choice of sub-plug location impacts on the predicted permeability and threshold pressure results and to what extent a single calibration can be transferred to other samples collected from the same or different formations. Additionally, the quality of the statistical calibrations should be assessed on a sample-by-sample basis before any predictions are made at the larger scale. It is likely that there is a relatively narrow range of image resolution for which the characteristics identified in this paper are effective predictors of permeability and threshold pressure for a given rock. If the resolution is too high then characteristics such as open pore fraction and formation factor will not contain information on channel sizes; if the resolution is too low then pore system geometric information is lost altogether. Nevertheless, the approach presented here allows for permeability, and with further testing, capillary pressure estimation for images of significantly lower resolution than was hitherto possible, and opens up the possibility of estimating these petrophysical properties for whole-core digital images, since scanners exist today which can image whole core of 100 mm diameter at the ~64 μm/voxel resolution used in this study.

The exploratory dataset of network model-based drainage and imbibition flow simulations presents encouraging results for the prediction of multi-phase flow in low-resolution images. The results indicate that, compared to data derived from pore morphology-based simulation, network model simulations produce higher values of threshold pressure and more accurate estimates of irreducible wetting phase saturation and lambda. Both network model and morphology-based simulations produce good correlations between threshold pressure and lower resolution predictor characteristics. Combined with the encouraging correlations with lambda I suggest it could be possible to predict a Brooks-Corey function that describes drainage flow in lower resolution images where its direct simulation is not possible. Statistical models of residual non-wetting phase saturation at the end of imbibition flow were less successful. Testing the influence of increasing irreducible wetting phase saturation and receding contact angle indicated that the non-wetting phase saturation generally decreases; however, the data in this thesis show that changes in residual non-wetting phase saturation do not translate to improvements in correlations with predictor characteristics. It is possible that larger datasets and the inclusion of more than just two predictor characteristics in a statistical model could describe more of the variance in residual non-wetting phase saturation.

One of the main objectives of this study was to explore the fundamentals of cross-scale correlations between predictor characteristics and petrophysical properties. Now that we have a better understanding of the relationships between flow properties and their predictor characteristics, more advanced techniques such as machine learning could be used to develop smarter predictions systems that might be able to perform more efficient image classifications and relate subtle changes in predictors to differences in flow behaviour at the larger scale.

# 12 References

Abdallah, W., Buckley, J. S., Carnegie, A., Herold, J. B. E., Fordham, E., Graue, A., et al. (2007). Fundamentals of Wettability. *Oilfield Review*, *19*(2).

Abdi, H., & Williams, L. J. (2010). Principal Component Analysis. *Wiley Interdisciplinary Reviews: Computational Statistics*, *2*(4), 433–459. https://doi.org/10.1002/wics.101

Ahmed, T. (2001). *Reservoir Engineering Handbook*. Gulf Professional Publishing.

Ahmed, T. (2005). *Working Guide to Reservoir Rock Properties and Fluid Flow* (1 edition). Amsterdam ; Burlington, MA: Gulf Professional Publishing.

Al-Anazi, A., & Gates, I. D. (2010). A Support Vector Machine Algorithm to Classify Lithofacies and Model Permeability in Heterogeneous Reservoirs. *Engineering Geology*, *114*(3–4), 267–277. https://doi.org/10.1016/j.enggeo.2010.05.005

Allen, R. J., & Houston, B. R. (1964). *Petrology of Mesozoic Sandstones of Carnarvon Highway Section, Western Bowen and Surat Basins* (No. 6). Gelogical Survey of Queensland.

Al-Menhali, A. S., & Krevor, S. (2016). Capillary Trapping of CO2 in Oil Reservoirs: Observations in a Mixed-Wet Carbonate Rock. *Environmental Science & Technology*, *50*(5), 2727–2734. https://doi.org/10.1021/acs.est.5b05925

Al-Raoush, R., & Papadopoulos, A. (2010). Representative Elementary Volume Analysis of Porous Media Using X-Ray Computed Tomography. *Powder Technology*, *200*(1–2), 69–77. https://doi.org/10.1016/j.powtec.2010.02.011

Anderson, W. G. (1986). Wettability Literature Survey Part 2: Wettability Measurement. *Journal of Petroleum Technology*, *38*(11). https://doi.org/10.2118/13933-PA

Anderson, W. G. (1987a). Wettability Literature Survey Part 4: Effects of Wettability on Capillary Pressure. *Journal of Petroleum Technology*, *39*(10), 1283–1300. https://doi.org/10.2118/15271-PA

Anderson, W. G. (1987b). Wettability Literature Survey Part 5: The Effects of Wettability on Relative Permeability. *Journal of Petroleum Technology*, *39*(11), 1453–1468. https://doi.org/10.2118/16323-PA

Andrew, M., Bijeljic, B., & Blunt, M. J. (2013). Pore-Scale Imaging of Geological Carbon Dioxide Storage Under in Situ Conditions. *Geophysical Research Letters*, *40*(15), 3915–3918. https://doi.org/10.1002/grl.50771

Apourvari, S. N., & Arns, C. H. (2014). An Assessment of the Influence of Micro-porosity for Effective Permeability Using Local Flux Analysis on Tomographic Images. International Petroleum Technology Conference. https://doi.org/10.2523/IPTC-17443-MS

Archie, G. E. (1942). The Electrical Resistivity Log as an Aid in Determining Some Reservoir Characteristics. *Transactions of the AIME*, *146*(01), 54–62. https://doi.org/10.2118/942054-G

Arns, C., Knackstedt, M., Pinczewski, W., & Garboczi, E. (2002). Computation of Linear Elastic Properties from Microtomographic Images: Methodology and Agreement Between Theory and Experiment. *GEOPHYSICS*, *67*(5), 1396–1405. https://doi.org/10.1190/1.1512785

Arns, C. H., Knackstedt, M. A., Pinczewski, M. V., & Lindquist, W. B. (2001). Accurate Estimation of Transport Properties from Microtomographic Images. *Geophysical Research Letters*, *28*(17), 3361–3364. https://doi.org/10.1029/2001GL012987

Arns, C. H., Knackstedt, M. A., Pinczewski, W. V., & Mecke, K. R. (2001). Euler-Poincaré Characteristics of Classes of Disordered Media. *Physical Review E*, *63*(3), 031112. https://doi.org/10.1103/PhysRevE.63.031112

Arns, C. H., Knackstedt, M. A., Pinczewski, W. V., & Martys, N. S. (2004). Virtual Permeametry on Microtomographic Images. *Journal of Petroleum Science and Engineering*, *45*(1–2), 41–46. https://doi.org/10.1016/j.petrol.2004.05.001

Arns, C. H., Knackstedt, M. A., & Martys, N. S. (2005). Cross-Property Correlations and Permeability Estimation in Sandstone. *Physical Review E*, *72*(4), 046304. https://doi.org/10.1103/PhysRevE.72.046304

Bai, B., ZHU, R., WU, S., YANG, W., Gelb, J., Gu, A., et al. (2013). Multi-Scale Method of Nano(micro)-Ct Study on Microscopic Pore Structure of Tight Sandstone of Yanchang Formation, Ordos Basin. *Petroleum Exploration and Development*, *40*(3), 354–358. https://doi.org/10.1016/S1876-3804(13)60042-7

Bakke, S., & Øren, P.-E. (1997). 3-D Pore-Scale Modelling of Sandstones and Flow Simulations in the Pore Networks. *SPE Journal*, *2*(02), 136–149. https://doi.org/10.2118/35479-PA

Bear, J. (1988). *Dynamics of Fluids in Porous Media*. Dover.

Beard, D. C., & Weyl, P. K. (1973). Influence of Texture on Porosity and Permeability of Unconsolidated Sand. *AAPG Bulletin*, *57*(2), 349–369.

Bell, B. A. (1996). A Review of Basic Core Analysis Techniques for Proper Evaluations of Heavy Oil Reservoirs. In *Geology of the Midway-Sunset Oil Field and Adjacent Temblor Range, San Joaquin Basin, California* (pp. 243–246). Bakersfield, CA: Pacific Section, AAPG. Retrieved from http://archives.datapages.com/data/pacific/data/093/093001/243_ps0930243.htm

Bennion, D. B., & Thomas, F. B. (1991). Recent Advances in Experimental and Analytical Tecniques for the Determination of Relative Permeability Data from Unsteady State Flow Experiments. Presented at the 10th Technical Conference and Exposition, Port of Spain, Trinidad: Society of Petroleum Engineers.

Berg, C. F. (2012). Re-Examining Archie's Law: Conductance Description by Tortuosity and Constriction. *Physical Review. E, Statistical, Nonlinear, and Soft Matter Physics*, *86*(4 Pt 2), 046314.

Berg, C. F. (2014). Permeability Description by Characteristic Length, Tortuosity, Constriction and Porosity. *Transport in Porous Media*, *103*(3), 381–400. https://doi.org/10.1007/s11242-014-0307-6

Berg, R. R. (1970). Method for Determining Permeability from Reservoir Rock Properties. *Transasctions - Gulf Coast Association of Geological Societies*, *XX*, 303–335.

Berryman, J. G., & Blair, S. C. (1986). Use of Digital Image Analysis to Estimate Fluid Permeability of Porous Materials: Application of Two-Point Correlation Functions. *Journal of Applied Physics*, *60*(6), 1930–1938. https://doi.org/10.1063/1.337245

Beucher, S., & Meyer, F. (1992). The Morphological Approach to Segmentation: The Watershed Transformation. In *Mathematical Morphology in Image Processing* (Vol. 34, pp. 433–481). New York: Marcell Dekker Inc.

Bhatnagar, P. L., Gross, E. P., & Krook, M. (1954). A Model for Collision Processes in Gases. I. Small Amplitude Processes in Charged and Neutral One-Component Systems. *Physical Review*, *94*(3), 511–525. https://doi.org/10.1103/PhysRev.94.511

Blunt, M. J. (2001). Flow in Porous Media — Pore-Network Models and Multiphase Flow. *Current Opinion in Colloid & Interface Science*, *6*(3), 197–207. https://doi.org/10.1016/S1359-0294(01)00084-X

Boggs, S. (2003). *Petrology of Sedimentary Rocks*. New York; Toronto; New York: The Blackburn Press.

Brinkman, H. C. (1949). A Calculation of the Viscous Force Exerted by a Flowing Fluid on a Dense Swarm of Particles. *Applied Scientific Research*, *1*(1), 27–34. https://doi.org/10.1007/BF02120313

Brooks, R. H., & Corey, A. T. (1964). Hydraulic Properties of Porous Media and Their Relation to Drainage Design. *Transactions of the ASAE*, *7*(1), 0026–0028. https://doi.org/10.13031/2013.40684

Bultreys, T., Hoorebeke, L. V., & Cnudde, V. (2016). Simulating Secondary Waterflooding in Heterogeneous Rocks with Variable Wettability Using an Image-Based, Multiscale Pore Network Model. *Water Resources Research*, *52*(9), 6833–6850. https://doi.org/10.1002/2016WR018950

Bultreys Tom, Stappen Jeroen Van, Kock Tim De, Boever Wesley De, Boone Marijn A., Hoorebeke Luc Van, & Cnudde Veerle. (2016). Investigating the Relative Permeability Behavior of Microporosity-Rich Carbonates and Tight Sandstones with Multiscale Pore Network Models. *Journal of Geophysical Research: Solid Earth*, *121*(11), 7929–7945. https://doi.org/10.1002/2016JB013328

Carman, P. C. (1956). *Flow of gases through porous media.* New York: Academic Press. Retrieved from http://catalog.hathitrust.org/Record/001478579

Caudle, B. H., Slobod, R. L., & Brownscombe, E. R. (1951). Further Developments in the Laboratory Determination of Relative Permeability. *Journal of Petroleum Technology*, *3*(05), 145–150. https://doi.org/10.2118/951145-G

Chapman, R. E. (Ed.). (1981). *Geology and Water*. Dordrecht: Springer Netherlands. Retrieved from http://link.springer.com/10.1007/978-94-009-8244-4

Chen, C. (2016). Multiscale Imaging, Modeling, and Principal Component Analysis of Gas Transport in Shale Reservoirs. *Fuel*, *182*, 761–770. https://doi.org/10.1016/j.fuel.2016.06.020

Chen, C.-H., & Lin, Z.-S. (2006). A Committee Machine with Empirical Formulas for Permeability Prediction. *Computers & Geosciences*, *32*(4), 485–496. https://doi.org/10.1016/j.cageo.2005.08.003

Clennell, M. B. (1997). Tortuosity: A Guide Through the Maze. *Geological Society, London, Special Publications*, *122*(1), 299–344. https://doi.org/10.1144/GSL.SP.1997.122.01.18

Cnudde, V., & Boone, M. N. (2013). High-Resolution X-Ray Computed Tomography in Geosciences: A Review of the Current Technology and Applications. *Earth-*

*Science Reviews*, *123*, 1–17. https://doi.org/10.1016/j.earscirev.2013.04.003

Craig, F. F. (1975). *The Reservoir Engineering Aspects of Waterflooding*. Richardson, Tex: Society of Petroleum.

Danielsson, P.-E. (1980). Euclidean Distance Mapping. *Computer Graphics and Image Processing*, *14*(3), 227–248. https://doi.org/10.1016/0146-664X(80)90054-4

Darcy, H. (1856). *Les fontaines publiques de la ville de Dijon*.

Darling, T. (2005). *Well Logging and Formation Evaluation*. Elsevier.

Detmer, D. M. (1995). Permeability, Porosity, and Grain-Size Distibrution of Selected Pliocene and Quaternary Sediments in the Abuquerque Basin. *New Mexico Geology*, *361*, 79–87.

Doyen, P. M. (1988). Permeability, Conductivity, and Pore Geometry of Sandstone. *Journal of Geophysical Research: Solid Earth*, *93*(B7), 7729–7740. https://doi.org/10.1029/JB093iB07p07729

Draper, N. R., & Smith, H. (2014). *Applied Regression Analysis*. John Wiley & Sons.

Durlofsky, L. J. (2005). Upscaling and Gridding of Fine Scale Geological Models for Flow Simulation. In *8th International Forum on Reservoir Simulation*. Iles Borromees, Stresa, Italy.

Farmer, C. L. (2002). Upscaling: A Review. *International Journal for Numerical Methods in Fluids*, *40*(1–2), 63–78. https://doi.org/10.1002/fld.267

Ferréol, B., & Rothman, D. H. (1995). Lattice-Boltzmann Simulations of Flow Through Fontainebleau Sandstone. In P. M. Adler (Ed.), *Multiphase Flow in Porous Media* (pp. 3–20). Springer Netherlands. Retrieved from http://link.springer.com/chapter/10.1007/978-94-017-2372-5_1

Filak, J.-M., Van Lint, J., Ali, F., Ma, E., & Al-Houti, R. (2013). Advanced Workflow for 3-D Geological Modeling of a Complex Giant Field, Greater Burgan, Kuwait. Society of Petroleum Engineers. https://doi.org/10.2118/164294-MS

Focke, J. W., & Munn, D. (1987). Cementation Exponents in Middle Eastern Carbonate Reservoirs. *SPE Formation Evaluation*, *2*(02), 155–167. https://doi.org/10.2118/13735-PA

Folk, R. L., & Ward, W. C. (1957). Brazos River Bar: A Study in the Significance of Grain Size Parameters. *Journal of Sedimentary Petrology*, *27*(1), 3–26.

Fredrich, J. T., Greaves, K. H., & Martin, J. W. (1993). Pore Geometry and Transport Properties of Fontainebleau Sandstone. *International Journal of Rock Mechanics and Mining Sciences & Geomechanics Abstracts*, *30*(7), 691–697. https://doi.org/10.1016/0148-9062(93)90007-Z

Gill, D. (1970). Application of a Statistical Zonation Method to Reservoir Evaluation and Digitized-Log Analysis. *AAPG Bulletin*, *54*(5), 719–729.

Golab, A., Knackstedt, M., Averdunk, H., Senden, T., Butcher, A., & Jaime, P. (2010). 3d Porosity and Mineralogy Characterization in Tight Gas Sandstones. *The Leading Edge*, *29*(12), 1476–1483. https://doi.org/10.1190/1.3525363

Grader, A. S., Nur, A., Baldwin, C., & Diaz, E. (2010). Multi-Scale Imaging Process for Computations of Porosity and Permeability from Carbonate Rocks. Presented at the GEO 2010 Conference, Manama, Bahrain. Retrieved from http://earthdoc.eage.org/publication/publicationdetails/?publication=52687

Harrell, F. E., Lee, K. L., Califf, R. M., Pryor, D. B., & Rosati, R. A. (1984). Regression Modelling Strategies for Improved Prognostic Prediction. *Statistics in Medicine*, *3*(2), 143–152.

Hayes, J. B. (1979). Sandstone Diagenesis—The Hole Truth. *The Society of Economic Paleontologists and Mineralogists*, *Special Publication*(26), 127–139.

Hazlett, R. D. (1995). Simulation of Capillary-Dominated Displacements in Microtomographic Images of Reservoir Rocks. *Transport in Porous Media*, *20*(1–2), 21–35. https://doi.org/10.1007/BF00616924

Hilpert, M., & Miller, C. T. (2001). Pore-morphology-based simulation of drainage in totally wetting porous media. *Advances in Water Resources*, *24*(3–4), 243–255. https://doi.org/10.1016/S0309-1708(00)00056-7

Hocking, R. R. (1976). A Biometrics Invited Paper. the Analysis and Selection of Variables in Linear Regression. *Biometrics*, *32*(1), 1–49. https://doi.org/10.2307/2529336

Jackson, J. E. (2005). *A User's Guide to Principal Components*. John Wiley & Sons.

Jennings, B. R., & Parslow, K. (1988). Particle Size Measurement: The Equivalent Spherical Diameter. *Proceedings of the Royal Society of London. A. Mathematical and Physical Sciences*, *419*(1856), 137–149. https://doi.org/10.1098/rspa.1988.0100

Jensen, H. I. (1921). The Geology of the Country North of Roma. *Queensland Government Mining Journal*, *22*, 92–93.

Jensen, H. I. (1926). *Gelogical Reconnaisance between Roma, Springsure, Tmabo, and Taroom* (No. 277). Geological Survey of Queensland.

Jolliffe, I. (2014). Principal Component Analysis. In *Wiley StatsRef: Statistics Reference Online*. John Wiley & Sons, Ltd. Retrieved from http://onlinelibrary.wiley.com/doi/10.1002/9781118445112.stat06472/abstract

Jones, A., Doyle, J., Jacobsen, T., & Kjønsvik, D. (1995). Which Sub-Seismic Heterogeneities Influence Waterflood Performance? A Case Study of a Low Net-to-Gross Fluvial Reservoir. *Geological Society, London, Special Publications*, *84*(1), 5–18. https://doi.org/10.1144/GSL.SP.1995.084.01.02

Karimpouli, S., Fathianpour, N., & Roohi, J. (2010). A New Approach to Improve Neural Networks' Algorithm in Permeability Prediction of Petroleum Reservoirs Using Supervised Committee Machine Neural Network (scmnn). *Journal of Petroleum Science and Engineering*, *73*(3–4), 227–232. https://doi.org/10.1016/j.petrol.2010.07.003

Katz, A. J., & Thompson, A. H. (1986). Quantitative Prediction of Permeability in Porous Rock. *The American Physical Society*, *34*(11), 8179–8181.

Kaufman, R. L., Dashti, H., Kabir, C. S., Pederson, J. M., Moon, M. S., Quttainah, R., & Al-Wael, H. (2002). Characterizing the Greater Burgan Field: Use of Geochemistry and Oil Fingerprinting. *SPE Reservoir Evaluation & Engineering*, *5*(03), 190–196. https://doi.org/10.2118/78129-PA

Khalili, A., Arns, J.-Y., Hussain, F., Cinar, Y., Pinczewski, W., & Arns, C. H. (2013). Permeability Upscaling for Carbonates From the Pore Scale by Use of Multiscale X-Ray-CT Images. *SPE Reservoir Evaluation & Engineering*, *16*(04), 353–368. https://doi.org/10.2118/152640-PA

King, M. J. (2007). *Upgridding and Upscaling: Current Trends and Future Directions*. Distinguished Lecturer Series presented at the SPE Distinguished Lecturer Series.

King, M. J., & Mansfield, M. (1999). Flow Simulation of Geologic Models. *SPE Reservoir Evaluation & Engineering*, *2*(04), 351–367. https://doi.org/10.2118/57469-PA

Kjonsvik, D., Doyle, J., & Jacobsen, T. (1994). The Effects Of Sedimentary Heterogeneities On Production From A Shallow Marine Reservoir - What Really Matters? Society of Petroleum Engineers. https://doi.org/10.2118/28445-MS

Kløv, T., Øren, P. E., Stensen, J. â., Lerdahl, T. R., Berge, L. I., Bakke, S., et al. (2003). Pore-to-Field Scale Modeling of WAG. In *SPE Annual Technical Conference and Exhibition*. Denver, Co, USA: Society of Petroleum Engineers. https://doi.org/10.2118/84549-MS

Knackstedt, M. A., Arns, C. H., Limaye, A., Sakellariou, A., Senden, T. J., Sheppard, A. P., et al. (2004). Digital Core Laboratory: Properties of Reservoir Core Derived from 3D Images. Society of Petroleum Engineers. https://doi.org/10.2118/87009-MS

Kozeny, J. (1927). *Über Kapillare Leitung Des Wassers Im Boden: (Aufstieg, Versickerung U. Anwendung Auf Die Bewässerg) ; Gedr. Mit Unterstützg Aus D. Jerome U. Margaret Stonborsugh-Fonds*. Hölder-Pichler-Tempsky, A.-G. [Abt.:] Akad. d. Wiss.

Krevor, S., Blunt, M. J., Benson, S. M., Pentland, C. H., Reynolds, C., Al-Menhali, A., & Niu, B. (2015). Capillary trapping for geologic carbon dioxide storage – From pore scale physics to field scale implications. *International Journal of Greenhouse Gas Control*, *40*, 221–237. https://doi.org/10.1016/j.ijggc.2015.04.006

Krumbein, W. C. (1934). Size Frequency Distributions of Sediments. *Journal of Sedimentary Research*, *4*(2), 65–77. https://doi.org/10.1306/D4268EB9-2B26-11D7-8648000102C1865D

Krumbein, W. C., & Monk, G. D. (1943). Permeability as a Function of the Size Parameters of Unconsolidated Sand. *Transactions of the AIME*, *151*(01), 153–163. https://doi.org/10.2118/943153-G

Latham, S., Varslot, T., & Sheppard, A. (2008). Automated Registration for Augmenting Micro-Ct 3d Images. In *Proceedings of the 14th Biennial Computational Techniques and Applications and Applications Conference*. Canberra, Aus: Australia and New Zealand Industrial and Applied Mathematics (ANZIAM). Retrieved from https://digitalcollections.anu.edu.au/handle/1885/51682

Latham, S., Varslot, T., Sheppard, A., & others. (2008). Image Registration: Enhancing and Calibrating X-Ray Micro-CT Imaging. *Proc. of the Soc. Core Analysts, Abu Dhabi, UAE*. Retrieved from https://www.researchgate.net/profile/Trond_Varslot/publication/254935632_IMAGE_REGISTRATION_ENHANCING_AND_CALIBRATING_X-RAY_MICRO-CT_IMAGING/links/53e4759d0cf21cc29fc8f891.pdf

Leopold, L. B., & Wolman, M. G. (1957). *River Channel Patterns: Braided, Meandering, and Straight* (USGS Numbered Series No. 282–B). U.S.

Geological Survey. Retrieved from http://pubs.er.usgs.gov/publication/pp282B

Lerdahl, T. R., Oren, P.-E., & Bakke, S. (2000). A Predictive Network Model for Three-Phase Flow in Porous Media. Presented at the SPE/DOE Improved Oil Recovery Symposium, Tulsa, Oklahoma: Society of Petroleum Engineers. https://doi.org/10.2118/59311-MS

Leverett, M. C. (1941). Capillary Behavior in Porous Solids. *Transactions of the AIME*, *142*(01), 152–169. https://doi.org/10.2118/941152-G

Li, Q., Zheng, J., Tsai, A., & Zhou, Q. (2002). Robust Endpoint Detection and Energy Normalization for Real-Time Speech and Speaker Recognition. *IEEE Transactions on Speech and Audio Processing*, *10*(3), 146–157. https://doi.org/10.1109/TSA.2002.1001979

Marquardt, D. W. (1980). A Critique of Some Ridge Regression Methods: Comment. *Journal of the American Statistical Association*, *75*(369), 87–91. https://doi.org/10.2307/2287388

Martin, K. R. (1977). *Sedimentology of the Precipice Sandstone, Surat Basin, Queensland.* University of Queensland.

Martys, N. S., & Chen, H. (1996). Simulation of Multicomponent Fluids in Complex Three-Dimensional Geometries by the Lattice Boltzmann Method. *Physical Review E*, *53*(1), 743–750. https://doi.org/10.1103/PhysRevE.53.743

Martys, N. S., Hagedorn, J. G., Goujon, D., & Devaney, J. E. (1999). Large-Scale Simulations of Single- and Multicomponent Flow in Porous Media. In *Developments in X-Ray Tomography II* (Vol. 3772, pp. 205–213). Denver, Co, USA. https://doi.org/10.1117/12.363723

Mecke,  null. (1996). Morphological Characterization of Patterns in Reaction-Diffusion Systems. *Physical Review. E, Statistical Physics, Plasmas, Fluids, and Related Interdisciplinary Topics*, *53*(5), 4794–4800.

Metz, M., Briceño, G., Diaz, E., Fang, Q., Grader, A., & Dvorkin, J. (2009). Properties of Tight Gas Sand From Digital Images. In *2009 Society of*

*Exploration Geophysicists Annual Meeting*. Houston, Texas: Society of Exploration Geophysicists. Retrieved from https://www.onepetro.org/conference-paper/SEG-2009-2135

Miall, A. D. (1977). A review of the braided-river depositional environment. *Earth-Science Reviews*, *13*(1), 1–62. https://doi.org/10.1016/0012-8252(77)90055-1

Muskat, M., & Meres, M. W. (1936). The Flow of Heterogeneous Fluids Through Porous Media. *Journal of Applied Physics*, *7*(9), 346–363. https://doi.org/10.1063/1.1745403

Nelson, P. H. (1994). Permeability-Porosity Relationships in Sedimentary Rocks. *The Log Analyst*, 38–62.

Oren, P.-E., Bakke, S., & Arntzen, O. J. (1998). Extending Predictive Capabilities to Network Models. *SPE Journal*, *3*(04), 324–336. https://doi.org/10.2118/52052-PA

Øren, P.-E., Bakke, S., & Held, R. (2007). Direct Pore-Scale Computation of Material and Transport Properties for North Sea Reservoir Rocks. *Water Resources Research*, *43*(12), W12S04. https://doi.org/10.1029/2006WR005754

Paterson, M. S. (1983). The Equivalent Channel Model for Permeability and Resistivity in Fluid-Saturated Rock—a Re-Appraisal. *Mechanics of Materials*, *2*(4), 345–352. https://doi.org/10.1016/0167-6636(83)90025-X

Patnode, H. W., & Wyllie, M. R. J. (1950). The Presence of Conductive Solids in Reservoir Rocks as a Factor in Electric Log Interpretation. *Journal of Petroleum Technology*, *2*(02), 47–52. https://doi.org/10.2118/950047-G

Peduzzi, P., Concato, J., Kemper, E., Holford, T. R., & Feinstein, A. R. (1996). A Simulation Study of the Number of Events Per Variable in Logistic Regression Analysis. *Journal of Clinical Epidemiology*, *49*(12), 1373–1379.

Peng, S., Marone, F., & Dultz, S. (2014). Resolution Effect in X-Ray Microcomputed Tomography Imaging and Small Pore's Contribution to Permeability for a

Berea Sandstone. *Journal of Hydrology*, *510*, 403–411. https://doi.org/10.1016/j.jhydrol.2013.12.028

Purcell, W. R. (1949). Capillary Pressures - Their Measurement Using Mercury and the Calculation of Permeability Therefrom. *Journal of Petroleum Technology*, *1*(02), 39–48. https://doi.org/10.2118/949039-G

Qian, Y.-H., & Zhou, Y. (1998). Complete Galilean-Invariant Lattice Bgk Models for the Navier-Stokes Equation. *EPL (Europhysics Letters)*, *42*(4), 359. https://doi.org/10.1209/epl/i1998-00255-3

Reeves, F. (1947). Geology of Roma District, Queensland, Australia. *AAPG Bulletin*, *31*(8), 1341–1371.

Ren, B., Sun, Y., & Bryant, S. (2014). Maximizing Local Capillary Trapping During CO2 Injection. *Energy Procedia*, *63*, 5562–5576. https://doi.org/10.1016/j.egypro.2014.11.590

Renard, P., & de Marsily, G. (1997). Calculating Equivalent Permeability: A Review. *Advances in Water Resources*, *20*(5–6), 253–278. https://doi.org/10.1016/S0309-1708(96)00050-4

Rink, M., & Schopper, J. R. (1978). On The Application Of Image Analysis To Formation Evaluation. *The Log Analyst*, *19*(01). Retrieved from https://www.onepetro.org/journal-paper/SPWLA-1978-vXIXn1a2

Sakellariou, A., Sawkins, T. J., Senden, T. J., & Limaye, A. (2004). X-Ray Tomography for Mesoscale Physics Applications. *Physica A: Statistical Mechanics and Its Applications*, *339*(1–2), 152–158. https://doi.org/10.1016/j.physa.2004.03.055

Schladitz, K., Ohser, J., & Nagel, W. (2006). Measuring Intrinsic Volumes in Digital 3d Images. In A. Kuba, L. G. Nyúl, & K. Palágyi (Eds.), *Discrete Geometry for Computer Imagery* (pp. 247–258). Springer Berlin Heidelberg. https://doi.org/10.1007/11907350_21

Sheppard, A., Latham, S., Middleton, J., Kingston, A., Myers, G., Varslot, T., et al. (2014). Techniques in Helical Scanning, Dynamic Imaging and Image

Segmentation for Improved Quantitative Analysis with X-Ray Micro-CT. *Nuclear Instruments and Methods in Physics Research Section B: Beam Interactions with Materials and Atoms*, *324*, 49–56. https://doi.org/10.1016/j.nimb.2013.08.072

Sheppard, A. P., Sok, R. M., & Averdunk, H. (2004). Techniques for Image Enhancement and Segmentation of Tomographic Images of Porous Materials. *Physica A: Statistical Mechanics and Its Applications*, *339*(1–2), 145–151. https://doi.org/10.1016/j.physa.2004.03.057

Sheppard, A. P., Sok, R. M., Averdunk, H., Robins, V. B., & Ghous, A. (2006). Analysis of Rock Microstructure Using High-Resolution X-Ray Tomography. In *The International Symposium of the Society of Core Analysts*. Trondheim, Norway.

Simmons, C. T. (2008). Henry Darcy (1803-1858): Immortalised by His Scientific Legacy. *Hydrogeology Journal*, *16*(6), 1023–1038. http://dx.doi.org.virtual.anu.edu.au/10.1007/s10040-008-0304-3

Sok, R. M., Varslot, T., Ghous, A., Latham, S., Sheppard, A. P., & Knackstedt, M. A. (2009). Pore Scale Characterisation of Carbonates at Multiple Scales: Integration of Micro-CT, BSEM, and FIBSEM. Presented at the Society of Core Analysist, The Netherlands.

Spanne, null, Thovert, null, Jacquin, null, Lindquist, null, Jones, null, & Adler, null. (1994). Synchrotron Computed Microtomography of Porous Media: Topology and Transports. *Physical Review Letters*, *73*(14), 2001–2004. https://doi.org/10.1103/PhysRevLett.73.2001

Swanson, B. F. (1981). A Simple Correlation Between Permeabilities and Mercury Capillary Pressures. *Journal of Petroleum Technology*, *33*(12), 2498–2504. https://doi.org/10.2118/8234-PA

Thomeer, J. H. M. (1960). Introduction of a Pore Geometrical Factor Defined by the Capillary Pressure Curve. *Journal of Petroleum Technology*, *12*(03), 73–77. https://doi.org/10.2118/1324-G

Thompson, K. E., Willson, C. S., White, C. D., Nyman, S., Bhattacharya, J., & Reed, A. H. (2005). Application of a New Grain-Based Reconstruction Algorithm to Microtomography Images for Quantitative Characterization and Flow Modeling. In *SPE Annual Technical Conference and Exhibition*. Dallas, Texas, USA: Society of Petroleum Engineers. https://doi.org/10.2118/95887-MS

Ubani, C. E., Adeboye, Y. B., & Oriji, A. B. (2012). Advances in Coring and Core Analysis for Reservoir Formation Evaluation. *Petroleum and Coal*, *54*(1), 42–51.

Udden, J. A. (1914). Mechanical Composition of Clastic Sediments. *Geological Society of America Bulletin*, *25*(1), 655–744. https://doi.org/10.1130/GSAB-25-655

Van Geet, M., Swennen, R., & Wevers, M. (2001). Towards 3-D Petrography: Application of Microfocus Computer Tomography in Geological Science. *Computers & Geosciences*, *27*(9), 1091–1099. https://doi.org/10.1016/S0098-3004(00)00154-0

Varslot, T., Kingston, A., Sheppard, A., & Sakellariou, A. (2010). Fast High-Resolution Micro-CT with Exact Reconstruction Methods. In *Developments in X-Ray Tomography VII* (Vol. 7804, pp. 780413-780413–10). San Diego, California, United States. https://doi.org/10.1117/12.860298

Vogel, H.-J. (2008). Topological Characterization of Porous Media. In K. R. Mecke & D. Stoyan (Eds.), *Morphology of Condensed Matter: Physics and Geometry of Spatially Complex Systems* (Vol. 600, pp. 75–91). Springer.

Walsh, J. B., & Brace, W. F. (1984). The Effect of Pressure on Porosity and the Transport Properties of Rock. *Journal of Geophysical Research*, *89*(B11), 9425. https://doi.org/10.1029/JB089iB11p09425

Washburn, E. W. (1921). The Dynamics of Capillary Flow. *Physical Review*, *17*(3), 273–283. https://doi.org/10.1103/PhysRev.17.273

Wentworth, C. K. (1922). A Scale of Grade and Class Terms for Clastic Sediments. *The Journal of Geology*, *30*(5), 377–392.

Whitehouse, F. W. (1953). *The Mesozoic Environments of the Great Artesian Basin* (No. 29). The Australian & New Zealand Association for the Advancement of Science.

Wildenschild, D., & Sheppard, A. P. (2013). X-Ray Imaging and Analysis Techniques for Quantifying Pore-Scale Structure and Processes in Subsurface Porous Medium Systems. *Advances in Water Resources*, *51*, 217–246. https://doi.org/10.1016/j.advwatres.2012.07.018

Winsauer, W. O., & McCardell, W. M. (1953). Ionic Double-Layer Conductivity in Reservoir Rock. *Journal of Petroleum Technology*, *5*(05), 129–134. https://doi.org/10.2118/953129-G

Yan, W., Crandall, D., Bruner, K., Ning, W., Gill, M., Xiaochun, L., & Bromhal, G. (2013). Core and Pore Scale Characterization of Liujiagou Outcrop Sandstone, Ordos basin, China for CO2 Aquifer Storage. *Energy Procedia*, *37*, 5055–5062. https://doi.org/10.1016/j.egypro.2013.06.419

Zhang, D., Zhang, R., Chen, S., & Soll, W. E. (2000). Pore Scale Study of Flow in Porous Media: Scale Dependency, Rev, and Statistical Rev. *Geophysical Research Letters*, *27*(8), 1195–1198. https://doi.org/10.1029/1999GL011101

Zhang, X., & Knackstedt, M. A. (1995). Direct Simulation of Electrical and Hydraulic Tortuosity in Porous Solids. *Geophysical Research Letters*, *22*(17), 2333–2336. https://doi.org/10.1029/95GL02230